

LARGE-SCALE DEFORMATION
AND STRESS LOCALIZATION
IN AMORPHOUS SOLIDS

A Dissertation

Presented to the Faculty of the Graduate School
of Cornell University

in Partial Fulfillment of the Requirements for the Degree of
Doctor of Philosophy

by

Lance Olav Eastgate

May 2004

© 2004 Lance Olav Eastgate

ALL RIGHTS RESERVED

LARGE-SCALE DEFORMATION
AND STRESS LOCALIZATION
IN AMORPHOUS SOLIDS

Lance Olav Eastgate, Ph.D.

Cornell University 2004

The shear-transformation-zone (STZ) theory by Falk and Langer describes the rheology of amorphous solids. It was based on the observation that plastic flow in metallic glasses consists of molecular rearrangements in localized areas (shear transformation zones). In this dissertation, a two-dimensional tensorial version of the theory is developed and explored numerically.

The numerical implementation uses finite-difference algorithms on a regular grid with a second-order explicit time-stepping scheme to integrate the equations forward in time. Deformation of the boundaries are handled by mapping the area of the material onto a unit square.

Two different geometries are used to simulate uniaxial tension experiments where materials are subjected to constant strain rates. In the first setup, a rectangular specimen is given an imperceptible indentation, allowing it to neck at the center. The dynamics are explored systematically by varying both the straining capability of the STZs (ϵ_0) and the external strain rate. Higher values of ϵ_0 increase the plastic flow and result in sharper necks. Decreased values of the external strain rate cause narrow shear bands to form, consistent with the absence of thermal relaxation mechanisms in the model.

In the second configuration, the equivalent of pre-annealed materials are explored. Here, the sample is initially square and the edges are made rough in order to encourage the formation of shear bands. With respect to ϵ_0 and the external strain rate, the results show trends similar to those in the necking simulations. The pre-annealing was modeled by using a low initial density of STZs. This had most effect when ϵ_0 was large, contributing to the localization of the strain and making the material appear more brittle.

BIOGRAPHICAL SKETCH

Lance Olav Eastgate was born in North Carolina on March 9, 1975. His father, a Kiwi, was finishing a doctorate in physics at UNC in Chapel Hill, and his mother, who is from Norway, was working in a research lab. After two years in Wisconsin, the family of three moved to Bergen, where Lance Olav completed three years of kindergarten, nine years of elementary school, ten years of piano practice, six years of computer games, one year of karate, and a year of ballroom dancing. Despite what might seem a long time, he was only 16 when they moved to Oslo. There he started high school and enrolled in the International Baccalaureate program. Although he had stopped taking piano lessons, computers and dancing dominated his extracurricular activities. Toward the end of high school he qualified for a spot on the Norwegian team competing in the International Mathematical Olympiad, which took place in Hong Kong during the summer of 1994.

Lance Olav had always enjoyed math and physics, and choosing a program in college was not hard. He enrolled at the University of Oslo in the fall of 1994, taking classes at the Faculty of Mathematics and Natural Sciences. Surrounded by fellow nerds, this was a great time for Lance Olav. After almost five years, he finished his *Candidatus Scientiarum* in physics while working in the group of Jens Feder. Notwithstanding long Latin terms, Lance Olav was accepted to Cornell University's graduate program in physics. After two and a half years in "gorges" Ithaca with Prof. Jim Sethna, and an equivalent amount of time in sunny Santa Barbara as a visiting graduate student with Prof. Jim Langer, Lance Olav's career as a graduate student seems to be drawing to a close.

To my parents, Richard and Signe, and my sister Lise.

ACKNOWLEDGEMENTS

I am exceedingly grateful to both Prof. Jim Sethna and Prof. Jim Langer, my advisors at Cornell University and UC Santa Barbara, respectively. Jim Sethna was always supportive with his unstoppable enthusiasm and amazing intuition. And Jim Langer, who graciously agreed to be my external advisor, always trusted my judgment and appreciated my contribution. I owe them both a huge Thank You.

I would like to thank Jim Langer's graduate students Anthony Foglia and Craig Maloney, and post-doc Leonid Pechenik. In addition to our many useful and interesting discussions, they were always willing to listen to my questions. A special thanks to Daniel Rabinowitz, who encouraged me to spend some of my graduate time at UCSB and who was willing to host me on several occasions.

I am also grateful for all the support and encouragement I received during my time at Cornell. I thank Markus Rauscher for always being down-to-earth and having good cheer and advice. I also greatly appreciate the time and help I got from Chris Myers and the others at the Cornell Theory Center.

I am truly grateful for having had the opportunity to meet and spend time with Robert Spatschek. His genuine personality makes him a valuable friend. I would also like to thank him for giving me some hints and suggestions on this manuscript.

You will have to look far and wide to find a kinder, more selfless person than Eirik Holm. A fellow Norwegian in Santa Barbara whose time and friendship I greatly appreciate, he immediately insisted that I borrow his computer so I could finish my thesis when my own machine came down with a fever. I am greatly indebted to him.

Without friends, the world is a very lonely place. I am thankful for all the friends that I made both in Ithaca and Santa Barbara, and for my friends back in Norway. I value every single one, and many have made extra efforts to stay in touch and express their care and support. I am especially grateful for the opportunity to become better acquainted with Jessica Morgenstern, who helped me confirm that trust, honesty, and good communication is essential for any relationship to work. Her support has helped me stay sane through these last six months. I would also like to mention my dear friend Johannes Kleppe; we have shared many adventures together, all around the world. I treasure his kindness, his intellect, and most of all, his friendship.

Last, but not least, I would like to express my love for my parents, Richard and Signe, and my sister Lise. My parents have always been caring and supportive of my decisions, and their continued love and encouragement during my time abroad have been a great comfort to me. I treasure my relationship with Lise enormously. I always look forward to our conversations, to spend time with her, and to share our passion for dancing. I am very grateful for my family, and although we have been spread across the globe in recent years, they are always there for me.

This work was supported primarily by the Research Council of Norway. It was supported in part by the National Science Foundation Materials Research Science and Engineering Centers (NSF MRSEC) program (DMR96-32716), due to Prof. Langer's gracious and surprising decision to assist me financially when my main grant ended. This work made use of the computing facility of the Cornell Center for Materials Research (CCMR) with support from the NSF MRSEC program (DMR-0079992), and computing facilities at UC Santa Barbara sponsored by a grant from the Keck Foundation for Interdisciplinary Research in Seismology and Materials

Science. Additional support came from the NSF-KDI program (DMR-9873214) and the U.S. Department of Energy (DE-FG03-99ER45762).

TABLE OF CONTENTS

Biographical Sketch	iii
Dedication	iv
Acknowledgements	v
Table of Contents	viii
List of Tables	x
List of Figures	xi
1 Introduction	1
2 Mathematical Framework	4
2.1 Tensorial Notation	5
2.2 Change of Basis	6
2.3 Material and Spatial Rates	9
2.4 Linear Elasticity in Two and Three Dimensions	14
2.5 Equations of Motion	19
2.6 Speed of Sound	21
3 The Shear-Transformation-Zone Theory	22
3.1 Introduction	22
3.2 Basic Properties	24
3.3 Constant Strain Rate	30
4 Deriving the Quasi-Linear Tensorial STZ Model	35
4.1 From Microscopics to a Mesoscopic Continuum Model	35
4.1.1 The Plastic Strain Rate	40
4.1.2 Introducing the STZ variables	42
4.1.3 The Quasi-Linear Model	43
4.2 Plastic Work and Dissipation	47
4.3 Combining the STZ theory with Linear Elasticity	52
4.4 A Scalar Version of the STZ Model	52
4.5 Energy Balance	54
4.6 Reduced Units	56
4.7 Initial Strain Rate	57
5 Numerical Setup	60
5.1 Overview	60
5.2 Mapping the Variables onto a Unit Square	62
5.3 Discretized Gradients	64
5.4 Time Stepping	65
5.5 Numerical Viscosity and Stability	66
5.6 Boundary Conditions	70
5.7 Change of Area in a Uniform Two-Dimensional Solid	74

6	Necking	77
6.1	Simulations	77
6.2	Discussion	87
7	Pre-Annealed Materials	94
7.1	Variation in ϵ_0	96
7.2	Comparing Pre-Annealed and Worked Materials	100
7.3	Strain-Rate Dependent Localization	102
8	Conclusion	105
A	Linear Stability Analysis of Numerical Algorithms	109
A.1	The Stability Criteria	109
A.2	Examples	110
A.2.1	Advection Equation with Explicit Euler	110
A.2.2	Diffusion Equation with Explicit Euler	111
A.2.3	Diffusion Equation with Second-Order Runge-Kutta in One Dimension	112
A.2.4	Diffusion Equation with Second-Order Runge-Kutta in Two Dimensions	113
A.2.5	Wave Equation with Lax	114
A.3	Derivation of the Stability Criteria Formulas	115
B	Mapping the Variables onto a Unit Square	117
B.1	Prelude	117
B.2	One Deforming Edge	118
B.3	Two Deforming Edges	122
	Bibliography	126

LIST OF TABLES

- 5.1 The symmetry conditions imposed on the fields in the necking calculations across the boundaries between the symmetric images . . . 70

LIST OF FIGURES

2.1	A vector represented in two coordinate systems rotated with respect to each other	7
3.1	The flow diagram for Δ when $\Lambda = 1$ and the deviatoric stress s is held constant	28
3.2	The steady-state stress s_∞ plotted against the scaled strain rate $D^{\text{tot}}/\epsilon_0$ in a uniform material	32
3.3	Stress-strain curves showing strain softening in a uniform material	34
4.1	A schematic illustration of an STZ as a two-state system	36
4.2	An illustration of the relation $\theta = \Phi + \Theta$, where Φ is the angle of the principal stress axis	46
5.1	The geometrical setup of the two-dimensional simulations	61
5.2	The two-dimensional area of the simulations mapped onto a unit square	63
5.3	Implementation of the step-doubling technique to control numerical accuracy	67
5.4	Definition of θ , the angle of the boundary $X(y, t)$	72
5.5	The shear modulus μ plotted against the relative change of area $\Delta A/A_0$ due to elastic deformation for a few selected values of the deviatoric stress	75
6.1	Outlines of the initial and strained configurations of two samples, one strained an order of magnitude faster than the other	79
6.2	The plastic dissipation Q and the velocity field in a strained sample	80
6.3	Six snapshots of a material as it was being strained, and the corresponding stress-strain curve	81
6.4	The true stress σ_{yy} at the grip plotted against the true total strain $\epsilon_{yy}^{\text{tot}}$ for selected values of ϵ_0	83
6.5	The true stress σ_{yy} at the grip plotted against the true total strain $\epsilon_{yy}^{\text{tot}}$ for selected values of D^{tot}	84
6.6	The true stress σ_{yy} at the grip plotted against the true total strain $\epsilon_{yy}^{\text{tot}}$, varying both ϵ_0 and D^{tot}	85
6.7	The true strain $\epsilon_{xx}^{\text{tot}}$ across the sample both at the end (grip) and at the middle (neck) as a function of the total strain $\epsilon_{yy}^{\text{tot}}$ along the sample for various values of ϵ_0	86
6.8	The true strain $\epsilon_{xx}^{\text{tot}}$ across the sample both at the end (grip) and at the middle (neck) as a function of the total strain $\epsilon_{yy}^{\text{tot}}$ for various strain rates, otherwise similar to Fig. 6.7	87
6.9	A “phase diagram” for the dynamics of constant strain rate necking simulations in the $(D^{\text{tot}}, \epsilon_0)$ parameter space	89
6.10	The same “phase diagram” as in Fig. 6.9, with simulations marked	91

7.1	Graphs of P_{external} , Q_{sum} , and Λ_{avg} for various values of ϵ_0 in a pre-annealed material	98
7.2	A comparison of a pre-annealed ($\Lambda_0 = 0.01$) and a worked ($\Lambda_0 = 1$) material	101
7.3	Density plots of Λ at 7% strain, showing that materials strained at higher rates did not make up for lost time when given time to relax	104

CHAPTER 1

INTRODUCTION

A glass is defined as a material that has solidified without crystallizing. It can be thought of as a liquid where the constituent particles have stopped in their tracks, at least when considered on time scales of days or shorter; it is a supercooled liquid. It is an amorphous solid.

There are several types of glasses, including the familiar silicate glasses as well as glassy polymers [1, 2, 3] and metallic glasses [4, 5, 6, 7]. Sometimes systems with larger particles where the thermal energy is insignificant are also included, such as rafts of soap bubbles [8, 9, 10, 11] and granular materials [12, 13, 14, 15, 16]. While glassy polymers often have long and entangled particles, the simple atomic structure of amorphous metals makes it easier to model. Although the results presented in this thesis are not limited to metallic glasses, this type of materials was the main focus while developing the model and comparing results to experiments.

Metallic glasses have been studied since Duwez *et al.* showed in 1960 that a metal could be quenched from a molten state without crystallizing [17]. For decades, the only way to achieve this was to cool the metal extremely rapidly in a process called melt-spinning, where a jet of molten metal hits a rotating metal disk, cooling the melt faster than 10^3 K/s (in fact, usually faster than 10^5 K/s) and forming a thin ribbon no thicker than $50\ \mu\text{m}$ [4]. Recently, new multi-component alloys with critical cooling rates as low as 0.1 K/s have been found, allowing the production of bulk metallic glasses [6, 18, 19]. This has simplified studies of the mechanical properties, and renewed interest in the material has also spurred many new applications; see [6] for some examples.

Amorphous metals have two modes of deformation: Homogeneous and inhomogeneous flow [20, 21, 22]. Homogeneous flow is typical for low stresses and high temperatures, and under uniaxial tension a material sample will deform uniformly throughout the specimen. In inhomogeneous flow, the deformation is usually localized in narrow shear bands that run at a 45° angle with respect to the tensile axis [23, 24] (some studies show that the angle of the shear bands deviate under large isotropic pressures [25, 26]). The cross-section of the material decreases as slip, and eventually fracture, occurs along these shear bands [21, 23, 27]. At low temperatures, the shear-localization instability sets in right after yield, making the material behave in a seemingly brittle manner; there is no hardening due to strain in metallic glasses, although physical aging decreases the plastic response [28].

This dissertation presents a two-dimensional model that describes elastic and plastic dynamics in an amorphous solid. The main contribution of this dissertation is the exploration of the shear-transformation-zone (STZ) theory, which is responsible for supplying the model with a plastic-flow description. Chapter 2 starts by presenting some basic mathematical equations including the linear elastic framework of the model. This chapter is relatively elementary, but is included for convenience and serves as an introduction to the notation used in this manuscript. Chapter 3 describes the basic behavior of a zero-dimensional, or scalar, version of the STZ model, initially developed by Falk and Langer [29, 30]. This scalar model represents the special case of a uniform material in a spatially extended system, which applies as long as the deformation is homogeneous throughout the sample. Chapter 4 derives a tensorial version of the STZ theory starting from microscopic observations. This model does not incorporate a mechanism for thermal relaxation, which means that its dynamics are pertinent to the low-temperature limit.

The tensorial version was based on both the scalar model developed earlier by Falk and Langer, as well as some of Falk's initial ideas of how to write the theory in a two-dimensional setting [29].

The remaining part, which forms the core of the dissertation, reviews two sets of numerical uniaxial-tension constant-strain-rate simulations of the two-dimensional, tensorial STZ model. First, Chapter 5 explains the details of the implementation. Then the first set is presented in Chapter 6, exploring how the plastic flow affected the dynamics during necking. The second set is described in Chapter 7, relating the pre-annealing of amorphous materials to increased strain localization and brittle behavior. The dissertation is concluded in Chapter 8.

CHAPTER 2

MATHEMATICAL FRAMEWORK

The shear-transformation-zone (STZ) model adds plasticity to linear elastic theory by providing microscopically derived state variables that keep track of the density and orientation of localized groups of particles that have the freedom to undergo large deformations. Before introducing the STZ model (Chapters 3 and 4), the basic mathematical framework of linear elastic theory will be established [31, 32]. This chapter presents the constitutive relations, leaving room for the plastic deformation which will be introduced later through the STZ theory. As in the Navier-Stokes model [33], these equations are formulated in terms of deformation *rates*. The model presented in this dissertation describes plastic flow, and the deformation itself (as opposed to its rates) cannot be used to describe the internal state since strain is dependent on the initial configuration.

Before presenting the equations for the linear elastic framework of the model, it is necessary to introduce and discuss mathematical notation that will be used throughout this dissertation. Section 2.1 shows how a tensor can be split into its isotropic and deviatoric parts. Section 2.2 explains how the representation of a tensor changes when the coordinate system rotates, and Section 2.3 shows how advection, including rotation, is taken into account in the temporal derivatives. Section 2.4 discusses the relation between two- and three-dimensional models. Finally, the last section presents the equations of motion for the stresses and velocities using Hooke's law (the linear elastic constitutive relations) and Newton's second law (conservation of momentum). The equations, which leave the plastic deformation unspecified, lay the foundation for the model. The remaining chapters are devoted to the details of the plastic flow, where the STZ theory is explained,

derived, and explored both analytically and numerically.

2.1 Tensorial Notation

In a two- or three-dimensional elastic and plastic material, it is convenient to write some of the variables describing the current state, such as the stress σ_{ij} , in tensorial form. Further, it is sometimes useful to decompose these tensors into their isotropic and deviatoric parts. The former corresponds to the trace of the tensor and represents the average value, while the latter is a traceless tensor which captures how the property in question is aligned.

As an example, the stress can be decomposed as

$$\boldsymbol{\sigma} = \begin{pmatrix} \sigma_{xx} & \sigma_{xy} \\ \sigma_{xy} & \sigma_{yy} \end{pmatrix} = \begin{pmatrix} -p - s & \tau \\ \tau & -p + s \end{pmatrix} \quad (2.1)$$

where the pressure p is the isotropic component, and the deviatoric part of the tensor (which is indicated by a tilde) is given by

$$\mathbf{s} \equiv \tilde{\boldsymbol{\sigma}} = \begin{pmatrix} s_{xx} & s_{xy} \\ s_{xy} & s_{yy} \end{pmatrix} = \begin{pmatrix} -s & \tau \\ \tau & s \end{pmatrix} \quad (2.2)$$

(be careful not to confuse the tensor \mathbf{s} with the component s). In general, a two-dimensional symmetric tensor T_{ij} can be written as

$$\mathbf{T} = \begin{pmatrix} T_{xx} & T_{xy} \\ T_{xy} & T_{yy} \end{pmatrix} = \begin{pmatrix} -T_p - T_s & T_\tau \\ T_\tau & -T_p + T_s \end{pmatrix} \quad (2.3a)$$

or

$$T_{ij} = -T_p \delta_{ij} + \tilde{T}_{ij}, \quad (2.3b)$$

where δ_{ij} is the Kronecker delta, \tilde{T}_{ij} is the deviatoric part of T_{ij} , and

$$T_p = -\frac{T_{xx} + T_{yy}}{2}, \quad T_s = -\frac{T_{xx} - T_{yy}}{2}, \quad T_\tau = T_{xy}. \quad (2.3c)$$

2.2 Change of Basis

This section describes how to transform the coordinates of a vector or a tensor between two bases that are rotated with respect to each other. Assume that $\hat{\mathbf{e}}_i$ and $\hat{\mathbf{e}}'_i$ are two orthogonal bases. Define the cosines between these unit vectors as

$$\hat{\mathbf{e}}'_i \cdot \hat{\mathbf{e}}_j = \beta_{ij}. \quad (2.4)$$

This means that

$$\hat{\mathbf{e}}'_i = \beta_{ij} \hat{\mathbf{e}}_j \quad \text{and} \quad \hat{\mathbf{e}}_i = \beta_{ji} \hat{\mathbf{e}}'_j. \quad (2.5)$$

A vector \mathbf{v} and a tensor $\boldsymbol{\sigma}$ can be written in the $\hat{\mathbf{e}}_i$ basis as

$$\mathbf{v} = v_i \hat{\mathbf{e}}_i \quad \boldsymbol{\sigma} = \sigma_{ij} (\hat{\mathbf{e}}_i \otimes \hat{\mathbf{e}}_j). \quad (2.6)$$

The *same* vector and tensor can be written using a different representation, or basis, $\hat{\mathbf{e}}'_i$:

$$\mathbf{v} = v'_i \hat{\mathbf{e}}'_i \quad \boldsymbol{\sigma} = \sigma'_{ij} (\hat{\mathbf{e}}'_i \otimes \hat{\mathbf{e}}'_j). \quad (2.7)$$

Writing the system in a rotated basis can be thought of as keeping the material and its properties standing still, and just changing the coordinate system. Of course, if the coordinate system changes (from $\hat{\mathbf{e}}_i$ to $\hat{\mathbf{e}}'_i$), then the coordinates have to change, too (from v_i and σ_{ij} to v'_i and σ'_{ij}). Fig. 2.1 illustrates how one vector can be represented in two different coordinate systems simultaneously.

If $\hat{\mathbf{e}}_i$ is the standard two-dimensional Cartesian coordinate system where the index i runs through the values x and y , and $\hat{\mathbf{e}}'_i$ is $\hat{\mathbf{e}}_i$ rotated an angle θ in the counter-clockwise direction, then

$$\hat{\mathbf{e}}_x = \begin{pmatrix} 1 \\ 0 \end{pmatrix}, \quad \hat{\mathbf{e}}_y = \begin{pmatrix} 0 \\ 1 \end{pmatrix}, \quad \hat{\mathbf{e}}'_x = \begin{pmatrix} \cos \theta \\ \sin \theta \end{pmatrix}, \quad \hat{\mathbf{e}}'_y = \begin{pmatrix} -\sin \theta \\ \cos \theta \end{pmatrix}, \quad (2.8)$$

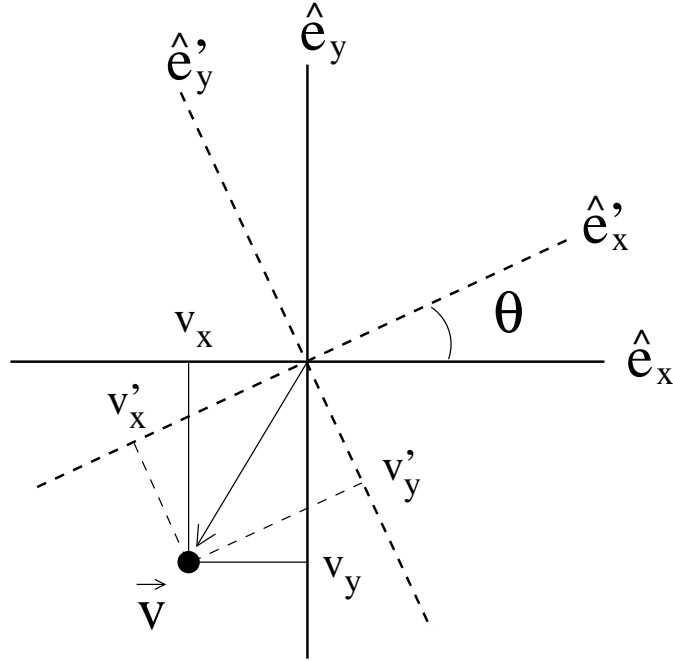


Figure 2.1: The vector \mathbf{v} represented in the two coordinate systems $\hat{\mathbf{e}}_i$ and $\hat{\mathbf{e}}'_i$, the latter rotated an angle θ in the counter-clockwise direction with respect to the former.

and

$$\boldsymbol{\beta} = \begin{pmatrix} \cos \theta & \sin \theta \\ -\sin \theta & \cos \theta \end{pmatrix}. \quad (2.9)$$

Further,

$$\begin{aligned} \mathbf{v} = v_i \hat{\mathbf{e}}_i &= \begin{pmatrix} v_x \\ v_y \end{pmatrix} & \mathbf{v} = v'_i \hat{\mathbf{e}}'_i &= \begin{pmatrix} v'_x \\ v'_y \end{pmatrix}' \\ \boldsymbol{\sigma} = \sigma_{ij} (\hat{\mathbf{e}}_i \otimes \hat{\mathbf{e}}_j) &= \begin{pmatrix} \sigma_{xx} & \sigma_{xy} \\ \sigma_{xy} & \sigma_{yy} \end{pmatrix} & \boldsymbol{\sigma} = \sigma'_{ij} (\hat{\mathbf{e}}'_i \otimes \hat{\mathbf{e}}'_j) &= \begin{pmatrix} \sigma'_{xx} & \sigma'_{xy} \\ \sigma'_{xy} & \sigma'_{yy} \end{pmatrix}'. \end{aligned} \quad (2.10)$$

The prime ($'$) on the matrices signifies that in these matrices the coordinates are given in the $\hat{\mathbf{e}}'_i$ basis.

Using the first part of Eq. (2.5), the vector \mathbf{v} and tensor $\boldsymbol{\sigma}$ can be written as

$$\mathbf{v} = v_i \hat{\mathbf{e}}_i = v_i \beta_{ji} \hat{\mathbf{e}}'_j = \begin{pmatrix} v_x \cos \theta + v_y \sin \theta \\ -v_x \sin \theta + v_y \cos \theta \end{pmatrix}' \quad (2.11a)$$

and

$$\begin{aligned} \boldsymbol{\sigma} &= \sigma_{ij} (\hat{\mathbf{e}}_i \otimes \hat{\mathbf{e}}_j) = \beta_{ki} \sigma_{ij} \beta_{lj} (\hat{\mathbf{e}}'_k \otimes \hat{\mathbf{e}}'_l) \\ &= \begin{pmatrix} -p - s \cos 2\theta + \tau \sin 2\theta & \tau \cos 2\theta + s \sin 2\theta \\ \tau \cos 2\theta + s \sin 2\theta & -p + s \cos 2\theta - \tau \sin 2\theta \end{pmatrix}', \end{aligned} \quad (2.11b)$$

respectively. In order to simplify Eq. (2.11b), the stresses have been written in their isotropic and deviatoric components, as given by Eq. (2.1). For clarity, the last equation can be written in terms of the isotropic and deviatoric components alone,

$$p' = p \quad (2.12a)$$

$$s' = s \cos 2\theta - \tau \sin 2\theta \quad (2.12b)$$

$$\tau' = \tau \cos 2\theta + s \sin 2\theta. \quad (2.12c)$$

Again, remember that σ'_{xx} represents the stress along x' , while σ_{xx} represents the stress along x .

The original coordinates can also be written in terms of the rotated coordinates by using the second part of Eq. (2.5):

$$\mathbf{v} = v'_i \hat{\mathbf{e}}'_i = v'_i \beta_{ij} \hat{\mathbf{e}}_j = \begin{pmatrix} v'_x \cos \theta - v'_y \sin \theta \\ v'_x \sin \theta + v'_y \cos \theta \end{pmatrix} \quad (2.13a)$$

and

$$\begin{aligned}\boldsymbol{\sigma} &= \sigma'_{ij}(\hat{\mathbf{e}}'_i \otimes \hat{\mathbf{e}}'_j) = \beta_{ik}\sigma'_{ij}\beta_{jl}(\hat{\mathbf{e}}_k \otimes \hat{\mathbf{e}}_l) \\ &= \begin{pmatrix} -p' - s' \cos 2\theta - \tau' \sin 2\theta & \tau' \cos 2\theta - s' \sin 2\theta \\ \tau' \cos 2\theta - s' \sin 2\theta & -p' + s' \cos 2\theta + \tau' \sin 2\theta \end{pmatrix}. \end{aligned} \quad (2.13b)$$

Writing out the mapping between the stresses explicitly gives

$$p = p' \quad (2.14a)$$

$$s = s' \cos 2\theta + \tau' \sin 2\theta \quad (2.14b)$$

$$\tau = \tau' \cos 2\theta - s' \sin 2\theta. \quad (2.14c)$$

For convenience, the special case for a traceless tensor, say the deviatoric stress \mathbf{s} , is written out below:

$$\begin{aligned}\mathbf{s} &= \begin{pmatrix} -s' & \tau' \\ \tau' & s' \end{pmatrix}' = \begin{pmatrix} -s \cos 2\theta + \tau \sin 2\theta & \tau \cos 2\theta + s \sin 2\theta \\ \tau \cos 2\theta + s \sin 2\theta & s \cos 2\theta - \tau \sin 2\theta \end{pmatrix}' \\ &= \begin{pmatrix} -s & \tau \\ \tau & s \end{pmatrix} = \begin{pmatrix} -s' \cos 2\theta - \tau' \sin 2\theta & \tau' \cos 2\theta - s' \sin 2\theta \\ \tau' \cos 2\theta - s' \sin 2\theta & s' \cos 2\theta + \tau' \sin 2\theta \end{pmatrix}. \end{aligned} \quad (2.15)$$

2.3 Material and Spatial Rates

Continuum mechanics has two types of description of the motion in common use: The material description and the spatial description [32, 34]. Consider a particle P located inside a material. Then

- the **material** or **referential** description has the position \mathbf{x}_0 of the particle P in some arbitrary reference configuration and the time t as its independent variables. If the system actually assumed the reference configuration at time $t = 0$, it is called the *Lagrangian* description. Malvern [34] states that there

is a subtle difference between the material and referential description; that the material description has the actual particle P , rather than the position of P in some reference configuration, as the independent variable. Disregarding the distinction between these two descriptions rarely causes any harm, and the terms “material” and “referential” are used interchangeably in this manuscript.

- the **spatial** description has the *current* position \boldsymbol{x} of the particle P and the time t as its independent variables. Also called the *Eulerian* description, it focuses on a fixed position in space, \boldsymbol{x} , rather than following the particle P around. The spatial description is useful when describing fluid flow, as in the Navier-Stokes equations [33], and was used for the equations of motion in the numerical simulations described in Chapters 5, 6, and 7.

Constitutive equations such as the stress-strain relations (Hooke’s law) usually have the simplest representation when presented in a frame of reference that is at rest relative to the material. Since the model in this dissertation is based on flow (or strain rates), it seems that the only viable approach is for the state variables to be given in Eulerian coordinates, as is done in the Navier-Stokes equations for fluid flow. The former description, using material derivatives, follows the material particles, while the latter representation uses local derivatives that are always fixed relative to the inertial lab frame.

The rest of this section gives an overview of the relation between the time derivatives given by the material and spatial descriptions. Although some derivations are included, this should not be considered rigorous mathematical proof; rather, its aim is to give some intuition into the use of material derivatives. The details can be found in for instance [32, 34].

As mentioned above, it is useful to write the material time derivative in terms of the spatial. Any variable, say the temperature T , can be written both in terms of the referential coordinates, $T = g_0(\mathbf{x}_0, t)$, and in terms of the spatial coordinates, $T = g(\mathbf{x}, t)$. In the material time derivative, the referential variables are kept constant. In the numerical simulations, which use the spatial description, the Eulerian variables are kept constant. In order to link this gap, it is assumed that there exists a sufficiently differentiable and single-valued function \mathbf{r} such that $\mathbf{x} = \mathbf{r}(\mathbf{x}_0, t)$, which describes the motion of the material in terms of the referential coordinates and the time; the function \mathbf{r} need not be known. Thus

$$T = g_0(\mathbf{x}_0, t) \equiv g[\mathbf{r}(\mathbf{x}_0, t), t]. \quad (2.16)$$

For a two-dimensional material this means that

$$\left(\frac{\partial T}{\partial t}\right)_{\mathbf{x}_0} = \left(\frac{\partial T}{\partial t}\right)_{\mathbf{x}} + \frac{\partial T}{\partial x} \left(\frac{\partial x}{\partial t}\right)_{\mathbf{x}_0} + \frac{\partial T}{\partial y} \left(\frac{\partial y}{\partial t}\right)_{\mathbf{x}_0}. \quad (2.17)$$

Since $\mathbf{x} = (x, y) = \mathbf{r}(\mathbf{x}_0, t)$, it follows that

$$\left(\frac{\partial \mathbf{x}}{\partial t}\right)_{\mathbf{x}_0} = \mathbf{v}. \quad (2.18)$$

As a notational convenience, the material and spatial time derivatives are written as

$$\left(\frac{\partial}{\partial t}\right)_{\mathbf{x}_0} \equiv \frac{D}{Dt} \quad \text{and} \quad \left(\frac{\partial}{\partial t}\right)_{\mathbf{x}} \equiv \frac{\partial}{\partial t}, \quad (2.19)$$

respectively. Thus

$$\frac{DT}{Dt} = \frac{\partial T}{\partial t} + v_x \frac{\partial T}{\partial x} + v_y \frac{\partial T}{\partial y}. \quad (2.20)$$

The left-hand side gives the change of temperature in a small part of the material, following specific particles even as it is moving and deforming, while the local

derivative $\partial T/\partial t$ gives the change in temperature of a specific location in space, regardless of what part of the material is occupying it.

For the special case of rigid translation, $DT/Dt = 0$. In spatial coordinates, on the other hand, the value of T changes if it has a gradient. For example, if $\partial T/\partial x > 0$, and $v_x > 0$, then as the body moves to the right (positive x -direction), the local value of T has to become smaller. Mathematically,

$$\frac{DT}{Dt} = \frac{\partial T}{\partial t} + v_x \frac{\partial T}{\partial x} = 0, \quad (2.21)$$

which means that

$$\frac{\partial T}{\partial t} = -v_x \frac{\partial T}{\partial x} < 0. \quad (2.22)$$

From the point of view of the particle, the coordinate system moves in the negative x -direction at a speed of $-v_x$.

When dealing with non-scalar quantities, both rotation and translation needs to be taken into account. The material derivatives with rotation for a vector \mathbf{v} and a tensor $\boldsymbol{\sigma}$ are given by

$$\frac{\mathcal{D}\mathbf{v}}{\mathcal{D}t} = \lim_{\Delta t \rightarrow 0} \left(\frac{\mathbf{v}^\Delta - \mathbf{v}}{\Delta t} \right)_{\mathbf{x}_0} \quad \text{and} \quad \frac{\mathcal{D}\boldsymbol{\sigma}}{\mathcal{D}t} = \lim_{\Delta t \rightarrow 0} \left(\frac{\boldsymbol{\sigma}^\Delta - \boldsymbol{\sigma}}{\Delta t} \right)_{\mathbf{x}_0}, \quad (2.23)$$

respectively. Here, \mathbf{v} and $\boldsymbol{\sigma}$ are given at time t , and \mathbf{v}^Δ and $\boldsymbol{\sigma}^\Delta$ are the values of \mathbf{v} and $\boldsymbol{\sigma}$ at a later time $t + \Delta t$ in the frame of the particle (that is, in referential coordinates):

$$\mathbf{v}^\Delta = \mathbf{R} \mathbf{v}[\mathbf{r}(\mathbf{x}_0, t + \Delta t), t + \Delta t] \quad (2.24a)$$

$$\boldsymbol{\sigma}^\Delta = \mathbf{R} \boldsymbol{\sigma}[\mathbf{r}(\mathbf{x}_0, t + \Delta t), t + \Delta t] \mathbf{R}^T, \quad (2.24b)$$

where

$$\mathbf{R} = \boldsymbol{\beta}(\theta = \Delta\alpha) \approx \begin{pmatrix} 1 & \Delta\alpha \\ -\Delta\alpha & 1 \end{pmatrix} \quad (2.25)$$

for small angles $\Delta\alpha$, giving the angular velocity

$$\omega = \lim_{\Delta t \rightarrow 0} \frac{\Delta\alpha}{\Delta t} = \frac{(\nabla \times \mathbf{v})_z}{2} = \frac{1}{2} \left(\frac{\partial v_y}{\partial x} - \frac{\partial v_x}{\partial y} \right); \quad (2.26)$$

if $\omega > 0$ then the material is rotating in the counter-clockwise direction. The operator \mathbf{R} changes the basis from $\hat{\mathbf{e}}_i$ to a coordinate system $\hat{\mathbf{e}}'_i$ which is rotated an angle θ in the counter-clockwise direction. Imagine that the material is undergoing a pure rigid rotation in the counter-clockwise direction. In this case, one would expect $\mathcal{D}/\mathcal{D}t = 0$; since the operator \mathbf{R} turns the coordinate system the exact same amount as the material is moving, it seems as if the material is standing still. Similarly, if the material is undergoing a pure rigid translation, then $\boldsymbol{\sigma}[\mathbf{r}(\mathbf{x}_0, t + \Delta t), t + \Delta t] = \boldsymbol{\sigma}[\mathbf{r}(\mathbf{x}_0, t), t]$, giving $D/Dt = 0$. Thus if there are only rigid translations and rotations, $\boldsymbol{\sigma}^\Delta = \boldsymbol{\sigma}$. These arguments hold true for \mathbf{v} , too.

Continuing with the derivation, one has that

$$\mathbf{R}\mathbf{v} = \mathbf{v} + \Delta\alpha\mathbf{v}_R \quad (2.27)$$

$$\mathbf{R}\boldsymbol{\sigma}\mathbf{R}^T = \boldsymbol{\sigma} + 2\Delta\alpha\boldsymbol{\sigma}_R \quad (2.28)$$

to first order in $\Delta\alpha$, where

$$\mathbf{v}_R = \begin{pmatrix} v_y \\ -v_x \end{pmatrix} \quad \text{and} \quad \boldsymbol{\sigma}_R = \begin{pmatrix} \tau & s \\ s & -\tau \end{pmatrix}. \quad (2.29)$$

This means that

$$\frac{\mathcal{D}\mathbf{v}}{\mathcal{D}t} = \frac{D\mathbf{v}}{Dt} + \omega\mathbf{v}_R \quad \text{and} \quad \frac{\mathcal{D}\boldsymbol{\sigma}}{\mathcal{D}t} = \frac{D\boldsymbol{\sigma}}{Dt} + 2\omega\boldsymbol{\sigma}_R. \quad (2.30)$$

The material time derivatives with rotation for each of the components v_x , v_y , p , s , and τ can be written as

$$\frac{\mathcal{D}}{\mathcal{D}t} \begin{pmatrix} v_x \\ v_y \end{pmatrix} = \frac{D}{Dt} \begin{pmatrix} v_x \\ v_y \end{pmatrix} + \omega \begin{pmatrix} v_y \\ -v_x \end{pmatrix}, \quad (2.31)$$

$$\frac{\mathcal{D}}{\mathcal{D}t} \begin{pmatrix} p \\ s \\ \tau \end{pmatrix} = \frac{D}{Dt} \begin{pmatrix} p \\ s \\ \tau \end{pmatrix} + 2\omega \begin{pmatrix} 0 \\ -\tau \\ s \end{pmatrix}. \quad (2.32)$$

As a check that this is correct, consider a pure rigid rotation in the counter-clockwise direction ($\omega > 0$) around the origin. This means that $\mathcal{D}\boldsymbol{\sigma}/\mathcal{D}t = 0$, giving that $Ds/Dt = 2\omega\tau$ and $D\tau/Dt = -2\omega s$. Consider a particle has $\tau > 0$; this means that the material is being sheared or stretched in the positive x - and y -direction, becoming longer along $y = x$ and shorter along $y = -x$. If there is rigid rotation, the particle does not notice any change in its surroundings, but locally the positive shear turns into a deviatoric stress that is positive in the y -direction. Thus a positive τ gives a positive s . Likewise, starting with a deviatoric stress in the y -direction, this turns into a negative shear.

Although the rotational derivatives apply to most vectors, they are not used in the equation of motion for the velocity, which comes from the conservation of momentum (Newton's second law). In this case the appropriate derivative is $D\mathbf{v}/Dt$, as used in Section 4.3. Detailed derivations can be found in [32, 34].

2.4 Linear Elasticity in Two and Three Dimensions

The theory and simulations presented in this dissertation are all strictly two-dimensional. Experiments and most of the literature describing them often use a three-dimensional description. The two-dimensional approach, where the third

degree of freedom simply does not exist, can model results from, say, a two-dimensional molecular dynamics simulation. But care should be taken when extrapolating the results to three dimensions. In certain cases a three-dimensional description can mimic a two-dimensional model. One such case is linear elasticity where the third dimension is made irrelevant by assuming plane stress or plane strain. This section presents linear elasticity in both two and three dimensions, and explains how these descriptions are connected in the cases of plane stress and plane strain.

In order to avoid confusion, all variables and parameters in this section have a subscript referring to what dimensional model they belong to. For instance, p_2 is the pressure in two dimensions, and σ_{3xx} is σ_{xx} in the three-dimensional model. If the form of an equation is valid in both two and three dimensions, a subscript d is used on the relevant variables and parameters, as in ν_d . Note that there are no dimensional indices on the strains ε_{ij} ; they are assumed to be unaffected by the dimensionality (with the only exception that ε_{xz} , ε_{yz} , and ε_{zz} do not exist in 2D).

Stress and pressure have different units in two and three dimensions, as does the shear modulus. Notationally, this is simplified by scaling all variables and parameters that have the unit of stress by $2\mu_d$, and writing the new variables with an accent: $\hat{\sigma}_d = \sigma_d/2\mu_d$, $\hat{p}_d = p_d/2\mu_d$, $\hat{s}_d = s_d/2\mu_d$, $\hat{E}_d = E_d/2\mu_d$, and $\hat{K}_d = K_d/2\mu_d$.

The following equations for the elastic strain $\boldsymbol{\varepsilon}$, the stress $\boldsymbol{\sigma}$, the deviatoric stress \boldsymbol{s} , the pressure p , the bulk compressibility K , Young's modulus E , and the

Poisson ratio ν , are true in both two and three dimensions:

$$\varepsilon_{ij} = \hat{\sigma}_{dij} - \frac{\nu_d}{1 + \nu_d} \hat{\sigma}_{dkk} \delta_{ij} = \hat{s}_{dij} - \frac{\hat{p}_d \delta_{ij}}{\hat{K}_d d}, \quad (2.33a)$$

$$\hat{\sigma}_{dij} = \frac{\hat{E}_d}{1 + \nu_d} \left(\varepsilon_{ij} + \frac{\nu_d}{1 - (d-1)\nu_d} \varepsilon_{kk} \delta_{ij} \right) \quad (2.33b)$$

$$\hat{p}_d = -\frac{1}{d} \hat{\sigma}_{dkk}, \quad (2.33c)$$

$$\hat{s}_{dij} = \hat{\sigma}_{dij} + \hat{p}_d \delta_{ij}, \quad (2.33d)$$

$$\hat{E}_d = 1 + \nu_2 \quad (2.33e)$$

$$\hat{K}_d \equiv -\frac{\hat{p}_d}{\varepsilon_{kk}}, \quad \hat{K}_d d = \frac{1 + \nu_d}{1 - (d-1)\nu_d}. \quad (2.33f)$$

The plan now is to write out these equations explicitly in both two and three dimensions, and then see if it is possible to restrict the latter to resemble the former (for example by using plane strain).

Consider a linear elastic block of material with an applied load $\hat{\sigma}_{dyy} = \hat{\sigma}_0$, where $\hat{\sigma}_{dxx} = 0$. In this setting, the Poisson ratio is defined as

$$\nu_d = \lim_{\sigma_0 \rightarrow 0} \left(-\frac{\varepsilon_{xx}}{\varepsilon_{yy}} \right). \quad (2.34)$$

In the case of a three-dimensional system, a constraint is needed for the z -direction as well. Both plane strain ($\varepsilon_{zz} = 0$) and plane stress ($\hat{\sigma}_{3zz} = 0$) will be considered below.

Writing out the diagonal terms of Eq. (2.33a) in two dimensions gives

$$\varepsilon_{xx} = -\nu_2 \hat{\sigma}_0 \quad \text{and} \quad \varepsilon_{yy} = (1 - \nu_2) \hat{\sigma}_0. \quad (2.35)$$

In three dimensions with plane stress ($\hat{\sigma}_{3zz} = 0$) the equations read

$$\varepsilon_{xx} = -\nu_3 \hat{\sigma}_0, \quad \varepsilon_{yy} = (1 - \nu_3) \hat{\sigma}_0, \quad \varepsilon_{zz} = -\nu_3 \hat{\sigma}_0, \quad (2.36)$$

while plane strain ($\varepsilon_{zz} = 0$) gives

$$\varepsilon_{xx} = -\frac{\nu_3}{1 - \nu_3} \hat{\sigma}_0, \quad \varepsilon_{yy} = \frac{1 - 2\nu_3}{1 - \nu_3} \hat{\sigma}_0, \quad \hat{\sigma}_{3zz} = \frac{\nu_3}{1 - \nu_3} \hat{\sigma}_0. \quad (2.37)$$

Comparing Eqs. (2.35) with (2.36), one can see that for plane stress the same equations are valid for ε_{xx} and ε_{yy} in both two and three dimensions. For plane strain, on the other hand, the equations for ε_{xx} and ε_{yy} are only the same if

$$\nu_2 = \frac{\nu_3}{1 - \nu_3} \quad (2.38)$$

from which it follows that

$$\begin{aligned} \nu_3 &= \frac{\nu_2}{1 + \nu_2}, & \frac{1 - \nu_2}{1 + \nu_2} &= 1 - 2\nu_3, \\ 2\hat{K}_2 &= \frac{1}{1 - 2\nu_3} = \frac{1 + \nu_2}{1 - \nu_2}, & 3\hat{K}_3 &= \frac{1 + \nu_3}{1 - 2\nu_3}. \end{aligned} \quad (2.39)$$

It is worth noting that the two- and three-dimensional Poisson ratio can have different values. Throughout this thesis, the value of the Poisson ratio was chosen to be $\nu_2 = 1/2$. This would correspond to $\nu_3 = 1/3$ in a three-dimensional model subjected to plane strain, which could occur in the bulk of a thick material, that is, where the length of the material in the third direction, L_z , is much greater than the two others, L_x and L_y . This is only of importance when making quantitative comparisons between two-dimensional models and three-dimensional experiments. The main focus of this dissertation is on describing behavior in two-dimensional models. Consequently, only the two-dimensional Poisson ratio ν_2 will be used. Before leaving the topic of three-dimensional systems, the two-dimensional linear elastic model will be compared to the three-dimensional version subjected to *plane strain* as an example of how the former can be viewed as a special case of the latter.

The full plane strain condition is that

$$\varepsilon_{xz} = \varepsilon_{yz} = \varepsilon_{zz} = 0, \quad v_z = 0, \quad \text{and} \quad \frac{\partial}{\partial z} = 0. \quad (2.40)$$

Note that since $\varepsilon_{zz} = 0$ in 3D, ε_{kk} is the same in both two and three dimensions.

Eq. (2.33a) gives that

$$\hat{s}_{3xz} = \hat{s}_{3yz} = \hat{\sigma}_{3xz} = \hat{\sigma}_{3yz} = 0, \quad (2.41a)$$

$$\hat{s}_{3xy} = \hat{s}_{2xy} = \hat{\sigma}_{3xy} = \hat{\sigma}_{2xy}. \quad (2.41b)$$

Using Eqs. (2.33f), one finds that

$$\hat{p}_3 = \frac{\hat{K}_3}{\hat{K}_2} \hat{p}_2 = \frac{2}{3}(1 + \nu_3) \hat{p}_2. \quad (2.42)$$

Eq. (2.33a) and $\varepsilon_{zz} = 0$ gives

$$\hat{s}_{3zz} = \frac{\hat{p}_3}{3\hat{K}_3} = \frac{2}{3}(1 - 2\nu_3) \hat{p}_2 \quad (2.43)$$

which together with (2.33d) gives

$$\hat{\sigma}_{3zz} = -2\nu_3 \hat{p}_2. \quad (2.44)$$

Combining (2.42) and (2.44) with (2.33c) for $d = 3$, one finds that

$$\hat{p}_2 = -\frac{\hat{\sigma}_{3xx} + \hat{\sigma}_{3yy}}{2}; \quad (2.45)$$

further, using Eq. (2.45) with (2.33c) for $d = 2$, one gets

$$\hat{\sigma}_{3xx} + \hat{\sigma}_{3yy} = \hat{\sigma}_{2xx} + \hat{\sigma}_{2yy}. \quad (2.46)$$

When taking the difference $\varepsilon_{xx} - \varepsilon_{yy}$ using (2.33a) (in either two or three dimensions), the pressure disappears, and it follows that

$$\hat{s}_{3xx} - \hat{s}_{3yy} = \hat{s}_{2xx} - \hat{s}_{2yy}, \quad (2.47)$$

$$\hat{\sigma}_{3xx} - \hat{\sigma}_{3yy} = \hat{\sigma}_{2xx} - \hat{\sigma}_{2yy}. \quad (2.48)$$

Finally, combining (2.46) and (2.48) gives the linear-elastic relations between the stresses in a two-dimensional model and a three-dimensional model subjected to

plane strain:

$$\begin{pmatrix} \hat{\sigma}_{3xx} & \hat{\sigma}_{3xy} & \hat{\sigma}_{3xz} \\ \hat{\sigma}_{3xy} & \hat{\sigma}_{3yy} & \hat{\sigma}_{3yz} \\ \hat{\sigma}_{3xz} & \hat{\sigma}_{3yz} & \hat{\sigma}_{3zz} \end{pmatrix} = \begin{pmatrix} \hat{\sigma}_{2xx} & \hat{\sigma}_{2xy} & 0 \\ \hat{\sigma}_{2xy} & \hat{\sigma}_{2yy} & 0 \\ 0 & 0 & -2\nu_3\hat{p}_2 \end{pmatrix}, \quad (2.49a)$$

$$\hat{p}_3 = \frac{2}{3}(1 + \nu_3)\hat{p}_2. \quad (2.49b)$$

Making a similar comparison between two and three dimensions when plastic flow is included is harder; so far, the three-dimensional STZ theory has only been successfully related to the two-dimensional version when imposing plane strain on the elastic and plastic parts separately. The results presented in this dissertation are still valid as long as they are considered in the context of this “strictly two-dimensional” environment; a more detailed analysis will be needed if quantitative comparisons are to be made with three-dimensional experimental results.

2.5 Equations of Motion

It is now time to write down the equations of motion that constitute the framework of the flow model, having presented the necessary mathematical tools. These equations include the rates for the stress $\boldsymbol{\sigma}$ and the velocity \boldsymbol{v} , which will use Hooke’s law (the linear elastic constitutive relations) and Newton’s second law (conservation of momentum), respectively.

The equation of motion for the velocity basically states that momentum is conserved, and is written as

$$\rho \frac{Dv_i}{Dt} = \frac{\partial \sigma_{ji}}{\partial x_j}. \quad (2.50)$$

To form the stress rates, it is assumed that the total rate of deformation can be

written as the superposition of the elastic and plastic parts,

$$D_{ij}^{\text{tot}} = D_{ij}^{\text{el}} + D_{ij}^{\text{pl}}. \quad (2.51)$$

The left-hand side is approximated as

$$D_{ij}^{\text{tot}} \approx \frac{1}{2} \left(\frac{\partial v_i}{\partial x_j} + \frac{\partial v_j}{\partial x_i} \right), \quad (2.52)$$

where the geometric nonlinear terms are left out [31]. The elastic rate of deformation is given by

$$D_{ij}^{\text{el}} = \frac{\mathcal{D}\varepsilon_{ij}}{\mathcal{D}t}, \quad (2.53)$$

where ε_{ij} is the elastic strain. The form of the plastic rate of deformation D_{ij}^{pl} is the topic of Chapters 3 and 4. The two-dimensional version of the constitutive equations (2.33a) relating the stress and the strain becomes

$$\varepsilon_{ij} = \frac{\sigma_{ij}}{2\mu} - \frac{\nu_2}{1 + \nu_2} \frac{\sigma_{kk}}{2\mu} \delta_{ij} = \frac{s_{ij}}{2\mu} - \frac{1 - \nu_2}{1 + \nu_2} \frac{p}{2\mu} \delta_{ij}, \quad (2.54a)$$

and stated here for convenience, Eq. (2.54a) can also be written in terms of the stresses:

$$\frac{\sigma_{ij}}{2\mu} = \varepsilon_{ij} + \frac{\nu_2}{1 - \nu_2} \varepsilon_{kk} \delta_{ij}. \quad (2.54b)$$

The equations of motion for the stresses can now be found by combining Eqs. (2.51), (2.53), and (2.54a). It is easier to write the equations after splitting the stresses into isotropic and deviatoric parts, as shown in Section 2.1; the equations of motion for the stress and velocity are thus written as

$$\left(\frac{1 - \nu_2}{1 + \nu_2} \right) \frac{1}{2\mu} \frac{Dp}{Dt} = -\frac{1}{2} \nabla \cdot \mathbf{v}, \quad (2.55a)$$

$$\frac{1}{2\mu} \frac{\mathcal{D}s_{ij}}{\mathcal{D}t} = \tilde{D}_{ij}^{\text{tot}} - D_{ij}^{\text{pl}}, \quad (2.55b)$$

$$\rho \frac{Dv_i}{Dt} = \frac{\partial s_{ji}}{\partial x_j} - \frac{\partial p}{\partial x_i}, \quad (2.55c)$$

where the deviatoric part of the total rate of deformation is given by

$$\tilde{D}_{ij}^{\text{tot}} = \frac{1}{2} \left(\frac{\partial v_i}{\partial x_j} + \frac{\partial v_j}{\partial x_i} \right) - \frac{1}{2} \nabla \cdot \mathbf{v}. \quad (2.56)$$

The plastic deformations are assumed to conserve volume (or area, since there are only two dimensions), thus D_{ij}^{pl} is traceless and $D_{ij}^{\text{pl}} \equiv \tilde{D}_{ij}^{\text{pl}}$. The five independent equations (2.55) specify the dynamics of the stresses and the velocities, with the only piece left unspecified being the plastic rate of deformation D_{ij}^{pl} . The STZ theory described in the following chapters suggests how to formulate the dynamics of the plastic flow based on microscopic considerations.

2.6 Speed of Sound

The speed of sound in an elastic material determines how quickly information, and deformations, can propagate. When considering plastic flow, it is often assumed that the elastic deformations occur instantaneously, or that the speed of sound is large compared to the velocity of the material. To make sure that this quasi-static assumption holds, it is necessary to know how the sound speed relates to the other parameters.

In a system where the elastic wavelengths are much smaller than the size of the material (that is, in an infinite system), the transverse wave speed is given by

$$c_t = \sqrt{\frac{\mu}{\rho}} \quad (2.57)$$

in both two and three dimensions. The longitudinal (or dilatational) wave speed c_l is faster by at least a factor of $\sqrt{2}$, but the exact factor depends on the dimensionality of the system and the Poisson ratio. For finite systems, small changes due to the geometry must also be taken into account. See [31] for further details.

CHAPTER 3

THE SHEAR-TRANSFORMATION-ZONE THEORY

3.1 Introduction

The goal of the continuum shear-transformation-zone (STZ) theory is to describe plastic deformation in amorphous solids on a mesoscopic scale, averaging out some of the microscopic, discrete details. These details are often atomistic, as in metallic glasses [4, 5, 6, 7], but they can also be larger, as in granular materials [12, 13, 14, 15, 16] or even foams [8, 9, 10, 11]. The plastic deformation is described in terms of flow rates, similar in approach to that of the Navier-Stokes model [33] although the scalar pressure has been replaced with a stress tensor.

There have been many attempts to describe plastic flow in crystalline and polycrystalline materials [35, 36, 37, 38, 39, 40, 41, 42, 43, 44]. The conventional approach has been to separate the static and time-dependent descriptions, although a few of them are so-called “unified theories” that try to combine the two in a single model. The STZ model is an example of such a unified theory, incorporating both static and time-dependent plastic flow in one succinct description, but it is based on the microscopic dynamics of amorphous solids¹.

The STZ theory was constructed by Falk and Langer [29, 30, 47, 48, 49, 50, 51, 52], and originated with the assumption that plastic deformation is limited to, and defined as, the non-affine transformation of particles in localized areas or zones. This was based on similar ideas made by Argon, Spaepen, and others who described creep in metallic glasses in terms of local, molecular transitions or rearrangements [8, 20, 53, 54, 55, 56]. This, in turn, grew out of theories by Turnbull, Cohen,

¹Recently, a couple of models for glassy materials using the free volume as an order parameter have been published [15, 45, 46].

and others, who suggested that the observed behavior in the amorphous metals could be described by linking the transition rates to local free-volume fluctuations [53, 57, 58, 59].

To identify these localized zones of non-affine transformations, Falk invented a metric. The question he asked was: Given two snapshots taken at different times during a molecular dynamics simulation, how could one identify where there had been plastic deformations? To answer this question, he developed a numerical tool where he would take an atom or particle and all of its neighbors within a certain cutoff radius (in his case the radius of the cutoff was 2.5 times that of the atom), and compare the configuration of all these atoms in the initial snapshot with the configuration of the same atoms in the final snapshot. Specifically, he would try to describe the transformation using a local strain tensor. Only if the deformation could be described as uniform strain would this be accurate; otherwise a best fit would be made by minimizing the deviation from a uniform strain deformation. This deviation, which he referred to as D_{\min}^2 , would measure the amount of non-affine deformation in the neighborhood of the given atom. He would then calculate D_{\min}^2 for each atom in the simulation and use it as a diagnostic to measure the amount of local rearrangements in different areas; a high D_{\min}^2 would thus correspond to an area with many active STZs. For a more detailed account of D_{\min}^2 , see [29, 30, 47].

Looking more closely at the areas that had a high D_{\min}^2 , Falk noticed that they behaved like two-state systems. When stressed in one direction, the atoms would locally rearrange in a non-affine manner, or flip, in order to relieve stress, but any further applied stress would not have any significant effect (see Fig. 4.1 in the next chapter for an illustration of such a flip). On the other hand, a stress

in the opposite direction would readily change the configuration back, although, again, any further stress would only have a negligible effect. In short, these areas, or STZs, could flip back and forth but would “jam” any further deformation if stressed in one direction only.

In order to describe these STZs in a continuum setting, Falk introduced the state variables Λ and Δ_{ij} . The former is a scalar that measures a scaled density of STZs, while the latter is a traceless tensor that indicates the alignment of flipped STZs, that is, the direction in which the majority of the STZs are pointing.

A tensorial version of this model will be developed and explored in Chapter 4. In the following section, the more intuitive special case of an infinite, uniform material (sometimes referred to as the zero-dimensional, scalar, or non-tensorial description) will be discussed.

3.2 Basic Properties

Assume a uniform material subjected to simple shear, where the principal stress axes and the STZs align only along the horizontal (x) and vertical (y) directions. As compared to the two-dimensional version, this zero-dimensional or scalar STZ theory avoids the use of tensors, eliminating some equations and making the remaining ones simpler. In addition, the scalar model will be presented in reduced units where some of the physical parameters have been eliminated through rescaling (see Section 4.6).

In this zero-dimensional model, assume that $s \equiv s_{yy} = -s_{xx}$ and $s_{xy} = 0$ (the value of the hydrostatic pressure p depends on the boundary conditions, but it is not needed at this point). Thus $s > 0$ means that the material is being pulled in the y -direction, while $s < 0$ means that it is being pulled in the x -direction.

Similarly, define $\Delta \equiv \Delta_{yy} = -\Delta_{xx}$ and $\Delta_{xy} = 0$. When $\Delta > 0$, there are more STZs aligned along the y -axis, while $\Delta < 0$ means that a majority of STZs are lying parallel to the x -axis. If $\Delta = 0$ then there are equally many STZs pointing in the vertical and horizontal directions.

The equation of motion for the relative density of STZs in the scalar model is²

$$\dot{\Lambda} = \Gamma(1 - \Lambda), \quad (3.1)$$

where Γ , which is always positive, is proportional to both the rate of energy dissipation per STZ and the rate of creation and annihilation of STZs. The steady-state value for the density of STZs is $\Lambda = 1$, although if initially lower, it might take a long time for Λ to grow if the plastic dissipation is low. Notice in Eq. (3.1) how the first and second term represents the creation and annihilation of STZs, respectively. The first term creates STZs at a rate proportional to Γ , while the last term destroys them at a rate of $\Gamma\Lambda$. This means that as Λ increases, the rate of STZ annihilation will also increase until it balances the rate of creation; this happens when Λ reaches unity.

Currently, it will be assumed that the system has reached a state where $\Lambda = 1$. In that case,

$$\dot{\Delta} = w + \Gamma(0 - \Delta), \quad (3.2)$$

where

$$w \equiv \frac{D^{\text{pl}}}{\epsilon_0} = s - \Delta, \quad (3.3)$$

D^{pl} is the plastic rate of deformation, and ϵ_0 is a physical parameter proportional to the amount of strain induced by the flipping of STZs. The first term of Eq. (3.2), w , is responsible for changing Δ when the STZs are flipping, while the second and

²The full set of equations of motion for the scalar STZ model is derived in Section 4.4.

third terms adjust the variable as STZs are created and annihilated. The zero in the second term was included in order to compare it to the right-hand side of Eq. (3.1), but this will be explained later.

Considering only the first term, Δ grows more positive when $w > 0$. Physically, this means that more and more STZs align along the y -axis as long as the material is deforming plastically in the vertical direction. Similarly, as long as w stays negative, Δ will grow more negative as the number of STZs aligned with the x -axis increases. Still only considering the first term, assume that the stress s is held at a fixed positive stress, and that initially the STZs are randomly aligned along the horizontal and vertical axes giving $\Delta = 0$. The fixed stress causes a positive rate of deformation in the y -direction, and Δ will grow until it reaches s . The system becomes jammed. Increasing the stress a little will not do much, since most of the STZ are already aligned along the vertical axis. If, on the other hand, the stress is reversed ($s \rightarrow -s$), the rate of plastic deformation will become large and negative, and the STZs will quickly align along the x -axis as the Δ tries to catch up with the new value of s .

This would be the end of the story if STZs were never created nor destroyed. Notice how the last two terms of Eq. (3.2) resemble the right-hand side of Eq. (3.1). In both equations, the part that is proportional to Γ represents the creation of STZs, while the part that is proportional to $\Gamma\Lambda$ or $\Gamma\Delta$ speaks for the annihilation. The main difference from Eq. (3.1) is that the first part is zero; Δ does not change when new STZs are created. The reason for this is that the newly created STZs are randomly aligned in the horizontal and vertical directions. This is an important property of the model, because the newly created STZs can now flip and further deform the material. Thus, if the stress is high enough, and enough STZs are

annihilated and recreated, the system will no longer be jammed; there will be plastic flow.

It is worth looking at this mechanism in more detail. If $\Lambda = 1$, then

$$\Gamma = \frac{w^2}{(1 - \Delta^2)}. \quad (3.4)$$

Γ is proportional to both the creation and annihilation of STZs as well as the rate of dissipated energy per STZ. Inserting Eq. (3.4) into (3.2) gives

$$\dot{\Delta} = \frac{(s - \Delta)(1 - s\Delta)}{1 - \Delta^2}. \quad (3.5)$$

Again, assume that the material is subjected to a constant stress. Setting $\dot{\Delta} = 0$, one can see that there are two steady-state solutions:

$$\Delta = s \quad \text{and} \quad \Delta = \frac{1}{s}. \quad (3.6)$$

The first solution, as explained earlier, corresponds to a jammed material with $w = 0$. The second solution is new, and it was made possible by the annihilation term in Eq. (3.2). In this case, the plastic deformation is non-zero, and the material is flowing. The two steady-state solutions (3.6) have been plotted in Fig. 3.1. The transition between the jammed and flowing solutions occurs when the two solutions match at $s = \pm 1$:

$$\left. \begin{array}{l} |s| < 1 \quad \text{is jammed} \\ |s| > 1 \quad \text{is flowing} \end{array} \right\} \begin{array}{l} \text{for a steady-state solution} \\ (\dot{\Lambda} = \dot{\Delta} = 0, \Lambda = 1). \end{array} \quad (3.7)$$

The critical stress $|s| = 1$ behaves as if it were the yield stress, but notice that no explicit yield stress was specified in the model; it is a result of the interplay between the rate of flipping and the rate of creation and annihilation of STZs. It is worth noting that the denominator of Eq. (3.5) ensures that $\Delta^2 < 1$ (in general, $\Delta^2 < \Lambda^2$).

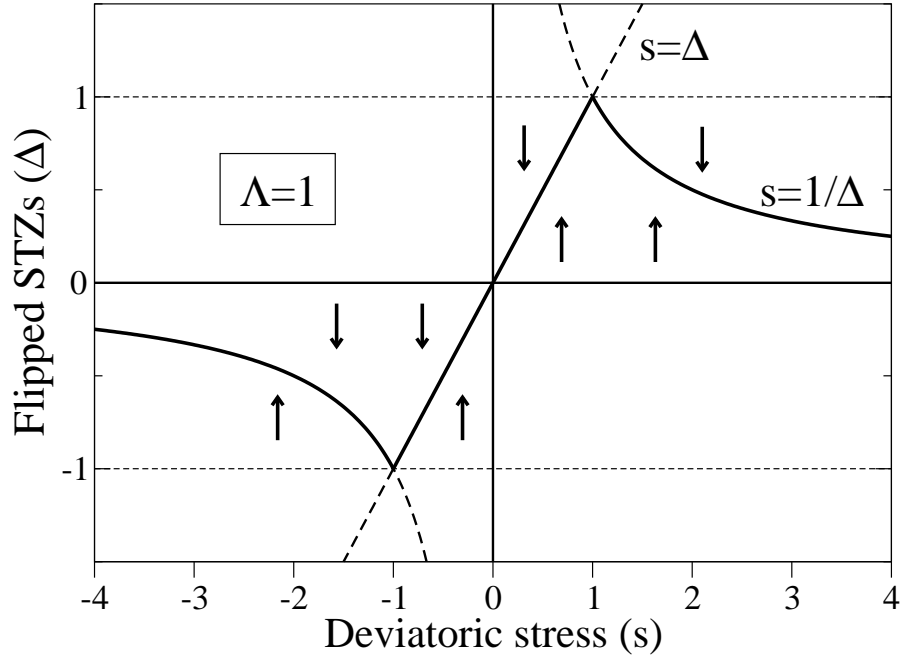


Figure 3.1: The flow diagram for Δ when $\Lambda = 1$ and the deviatoric stress s is held constant. The arrows show that Δ will flow towards the steady-state solution, and the horizontal lines emphasize that Δ^2 is always less than unity. The line $s = \Delta$ represents the jammed solution, while $s = 1/\Delta$ is the plastically flowing steady-state solution.

Until now, most of this discussion has focused on behavior at $\Lambda = 1$. Experiments have shown that metallic glasses that have been annealed below the glass transition temperature seem more brittle, show more pronounced strain softening, and have decreased plastic flow [21, 60, 61, 62, 63, 64, 65]. Microscopically, observations showed structural relaxation in the form of more closely packed molecules, corresponding to a macroscopic increase in density. Upon plastic deformation the materials were seen to return to their pre-annealed (as-quenched) states, including a decrease in the density and a lower packing fraction. Annealing for a longer time or with a higher temperature gave more pronounced changes in the mechanical properties. It is also worth noting that aging the materials over longer periods of

time at lower temperatures also made the metallic glasses more brittle [28].

The STZ theory captures the change in behavior due to annealing through the variable Λ . When a material is initially quenched from a molten state, the atoms have little time to organize into a closely packed configuration, leaving more potential STZs in a “fluffy” structure. Annealing the material packs the atoms into a tighter configuration and gives a lower initial Λ . This picture also fits in with the idea that plastic work increases the density of STZs; it “fluffs up” the tightly packed atoms, leaving more room for local rearrangements.

The version of the STZ theory that is explored numerically in this dissertation has no mechanism for thermal creep or relaxation, which is reflected in the fact that $\dot{\Lambda} \geq 0$. Thus the model can only simulate *pre*-annealed materials, by setting the initial value of Λ low. In order to incorporate the effects of annealing and aging seen in real materials, there would need to be a mechanism in Eq. (3.1) that could reduce the value of Λ . There are currently efforts to incorporate thermal effects into the STZ theory [66].

With Λ no longer assumed to be one, the equations of motion for $\dot{\Lambda}$ and $\dot{\Delta}$ read

$$\dot{\Lambda} = \Gamma(1 - \Lambda), \quad (3.8a)$$

$$\dot{\Delta} = w - \Gamma\Delta, \quad (3.8b)$$

with

$$\Gamma = \left(\frac{2\Lambda}{1 + \Lambda} \right) \frac{w^2}{\Lambda^2 - \Delta^2} \quad \text{and} \quad w = s\Lambda - \Delta. \quad (3.9)$$

Interesting enough, the stress at $|s| = 1$ can still be considered a yield stress. Unless the stress is increased too rapidly, $\Delta \approx \Lambda s$ as long as $|s| < 1$. This means that

$$\Gamma \propto \frac{w^2}{1 - s^2}. \quad (3.10)$$

Thus when the stress s^2 approaches one, the plastic dissipation increases dramatically which in turn forces the density of STZs to grow rapidly to its equilibrium value $\Lambda = 1$.

Instead of concentrating on the stress s , consider Δ^2 as it approaches Λ^2 ; this means that all the available STZs have flipped, inducing Γ to grow rapidly (due to its denominator), creating more STZs. The system will converge to steady state as $\Lambda \rightarrow 1$, and the results outlined earlier will apply.

3.3 Constant Strain Rate

So far, the discussion has focused on a uniform material subjected to a fixed load (that is, a constant stress s). Alternatively, one could strain the material at a constant rate and let the stress vary; it is this approach that is used in the numerical simulations described in Chapters 6 and 7. The equation of motion for the stress is³

$$\begin{aligned}\dot{s} &= \mu(1 + \nu_2) (D^{\text{tot}} - D^{\text{pl}}) \\ &= \mu(1 + \nu_2) (D^{\text{tot}} - \epsilon_0 w) ,\end{aligned}\tag{3.11}$$

where D^{tot} is given and constant. The total strain ϵ^{tot} and the total strain rate D^{tot} are linked through

$$\epsilon^{\text{tot}} = D^{\text{tot}} t\tag{3.12}$$

(ϵ^{tot} is the true, or logarithmic, strain, as opposed to the engineering strain). Note that as long as $\mu\epsilon_0$ and $D^{\text{tot}}/\epsilon_0$ are kept constant, ϵ_0 , μ , and D^{tot} can be changed without affecting the equations for \dot{s} , $\dot{\Lambda}$, or $\dot{\Delta}$ at all. In fact, Eq. (3.11) could be rescaled to eliminate one of the three parameters. Later on, though, when dealing

³See Section 4.4 for details on the derivation.

with a two-dimensional system, such a rescaling will no longer be possible: μ is part of determining the sound speed in the material, and the total strain will affect the geometry and thus the behavior of the material.

If the material is strained at a constant rate, steady state is reached when $\dot{\Lambda} = \dot{\Delta} = \dot{s} = 0$, which implies that $w = D^{\text{tot}}/\epsilon_0$, $\Lambda = 1$, and $\Delta = 1/s$. From this, the steady-state stress is found to be

$$s_{\infty} = \frac{D^{\text{tot}}}{2\epsilon_0} + \sqrt{1 + \left(\frac{D^{\text{tot}}}{2\epsilon_0}\right)^2} \approx \begin{cases} 1 & \text{when } D^{\text{tot}}/\epsilon_0 \ll 1 \\ D^{\text{tot}}/\epsilon_0 & \text{when } D^{\text{tot}}/\epsilon_0 \gg 1 \end{cases} \quad (3.13)$$

(this solution has $s_{\infty} \geq 1$; there is a second solution for the steady-state stress that gives $-1 \leq s_{\infty} < 0$, but this is an invalid solution since it gives $\Delta^2 > 1$). Eq. (3.13) is plotted in Fig. 3.2.

When looking beyond the scalar version of the STZ model, preparing for the spatially extended two-dimensional numerical simulations, it turns out that the results of a constant strain rate test depends on how the strain rate is initially ramped up. This is especially true for tests with high strain rates, although the sensitivity depends on the values of the other parameters as well. If the strain rate is ramped up too quickly to its final value, it becomes unclear how the speed of the spreading elastic and plastic deformations affect the results. If the strain rate is ramped up too slowly, the system might reach yield stress before the strain rate has attained its final value.

In order to eliminate some of these arbitrary side-effects caused by ramping up the strain rate at different speeds, one can start the numerical experiments with the strain rate already at its final value. Given this strain rate, one can calculate

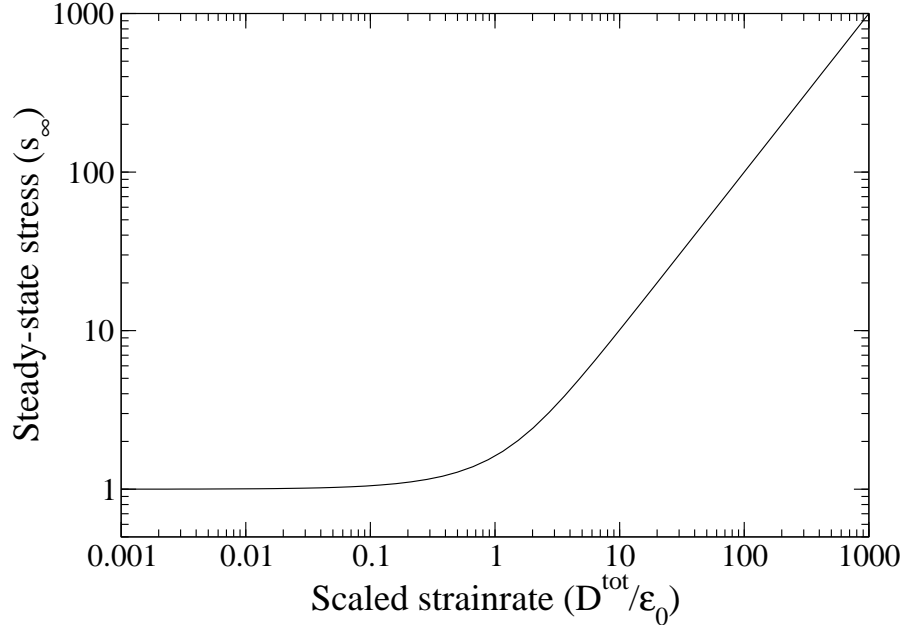


Figure 3.2: The steady-state stress s_∞ plotted against the scaled strain rate $D^{\text{tot}}/\epsilon_0$ in a uniform material. When $D^{\text{tot}}/\epsilon_0 \ll 1$, the steady-state stress remains around 1. When $D^{\text{tot}}/\epsilon_0 \gg 1$, the steady-state stress becomes proportional to the strain rate.

what the initial values of the other fields should be in order for the system to start off in a state close to steady state; this will minimize oscillating stresses and other transient effects. Given the strain rate D^{tot} and the initial values $\Lambda_0 \equiv \Lambda(0)$ and $\Delta(0) = 0$, the initial stress should be⁴

$$s(0) = \frac{D^{\text{tot}}}{\frac{1}{\mu(1+\nu_2)} + \epsilon_0 \Lambda_0}, \quad (3.14)$$

with the corresponding initial stress rate

$$\dot{s}(0) = s(0) \quad (3.15)$$

It is useful to know at what total strain $\epsilon_{\text{yield}}^{\text{tot}}$ and time Δt the stress s reaches unity (the “yield stress”). Although it is hard to calculate the exact value analyti-

⁴See Section 4.7 for details on the derivation.

cally, the assumption that \dot{s} stays constant until $s = 1$ gives a good approximation.

Combining $\dot{s}(0)\Delta t = 1 - s(0)$ and $\varepsilon_{\text{yield}}^{\text{tot}} = \Delta t D^{\text{tot}}$, solving for $\varepsilon_{\text{yield}}^{\text{tot}}$, gives

$$\varepsilon_{\text{yield}}^{\text{tot}} = \epsilon_0 \Lambda_0 - D^{\text{tot}} + \frac{1}{\mu(1 + \nu_2)} \quad [\text{assuming } s(0) < 1]. \quad (3.16)$$

The time then follows from $\Delta t = \varepsilon_{\text{yield}}^{\text{tot}}/D^{\text{tot}}$.

The STZ model can also account for an effect known as strain softening, where the stress peaks at a value higher than the yield stress before decaying down to a steady-state value. Fig. 3.3 shows how the scalar model behaves during two tension tests, the only difference between the two being the initial value of Λ . One can clearly see that there is strain softening in the case with the lower value of Λ_0 . This is because the initial lack of STZs limits the amount of plastic deformation, thus the system has no way of relieving itself of the elastic tension when the stress approaches the “yield stress”. The stress finally sinks back to its steady-state value when the number of STZs increases to $\Lambda = 1$. Notice that $\Delta^2 < \Lambda^2$, and that as long as $s < 1$, Δ tries to catch up with $s\Lambda$.

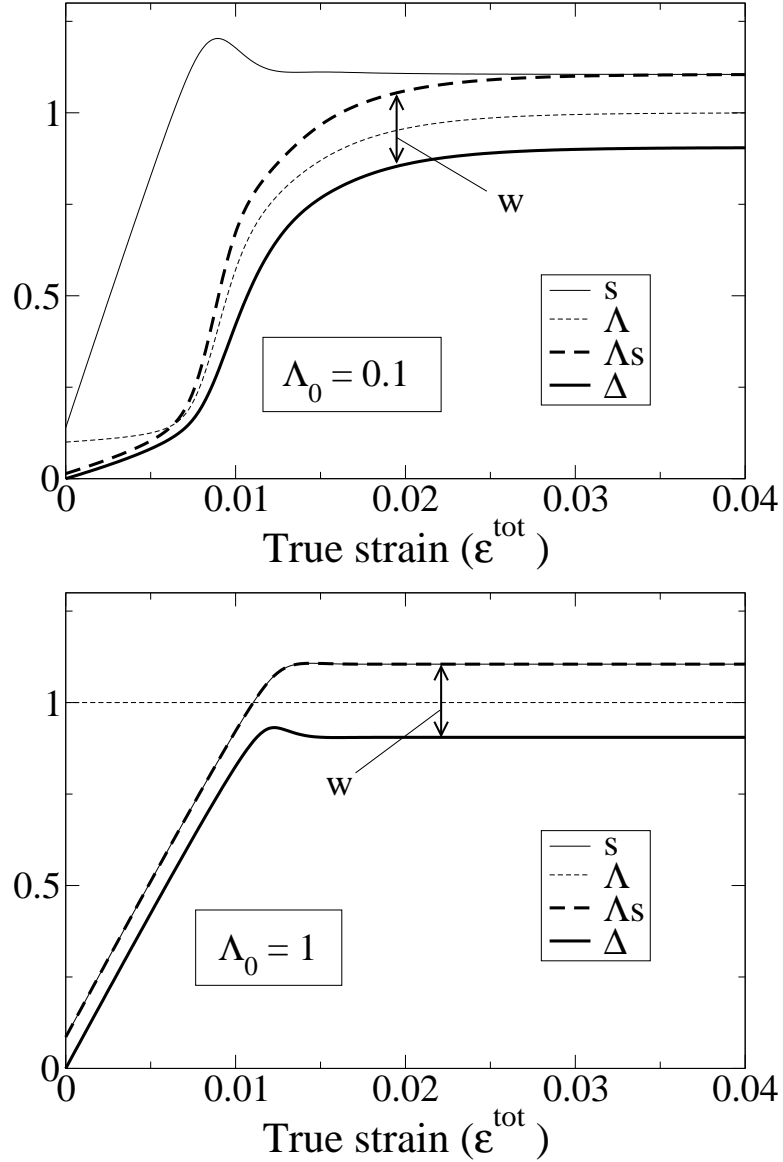


Figure 3.3: During a constant strain rate tension test, the variables in the zero-dimensional version of the STZ theory react differently for $\Lambda_0 = 0.1$ and $\Lambda_0 = 1$. In both cases $\mu = 100$, $\epsilon_0 = 0.005$, and $D^{\text{tot}} = 0.001$. In the test where $\Lambda_0 = 0.1$, there are initially fewer STZs, which means less plastic deformation (which is proportional to w). When the stress reaches the “yield stress”, the system has to wait for Λ to increase before there is a sufficient amount of STZs to supply enough plastic deformation to relieve the stress imposed by the constant rate of deformation. This leads to a spike in the stress before it reaches its steady-state value. This phenomenon is known as strain softening.

CHAPTER 4

DERIVING THE QUASI-LINEAR TENSORIAL STZ MODEL

A basic framework for describing deformation of matter was introduced in Section 2.5. The only part that was left unspecified in Eqs. (2.55) was the plastic rate of deformation D_{ij}^{pl} . Chapter 3 was an attempt to give an intuitive overview of both the microscopic mechanisms of plastic strain and the dynamics of the continuum equations of the non-tensorial STZ theory while avoiding detailed mathematical derivations linking the two. Section 4.1 fills that gap by quantitatively connecting microscopic non-affine rearrangements to a tensorial continuum formulation describing plastic deformation. Then Section 4.2 looks at plastic work, presents the assumption that the rate of creation and annihilation of STZs is proportional to the plastic dissipation, and discusses different forms of flow observed in experiments with amorphous metals. Section 4.3 incorporates the STZ description into the linear elastic framework before Section 4.4 presents the special zero-dimensional case when the material can be considered uniform. Section 4.5 talks about how the work done on the system is stored as elastic, plastic, or kinetic energy, or dissipated during plastic flow. Finally, subtle issues of initiating a constant strain-rate experiment are discussed in Section 4.7.

4.1 From Microscopics to a Mesoscopic Continuum Model

Section 3.1 gave an overview of the STZ model, where plastic flow is described on the microscopic scale as local, non-affine rearrangements of particles or atoms in “shear transformation zone”s (STZs). Each STZ can stretch in either of two directions, and the idea is that when a zone transforms, or flips, from one state to the other, it contributes to the local plastic strain.

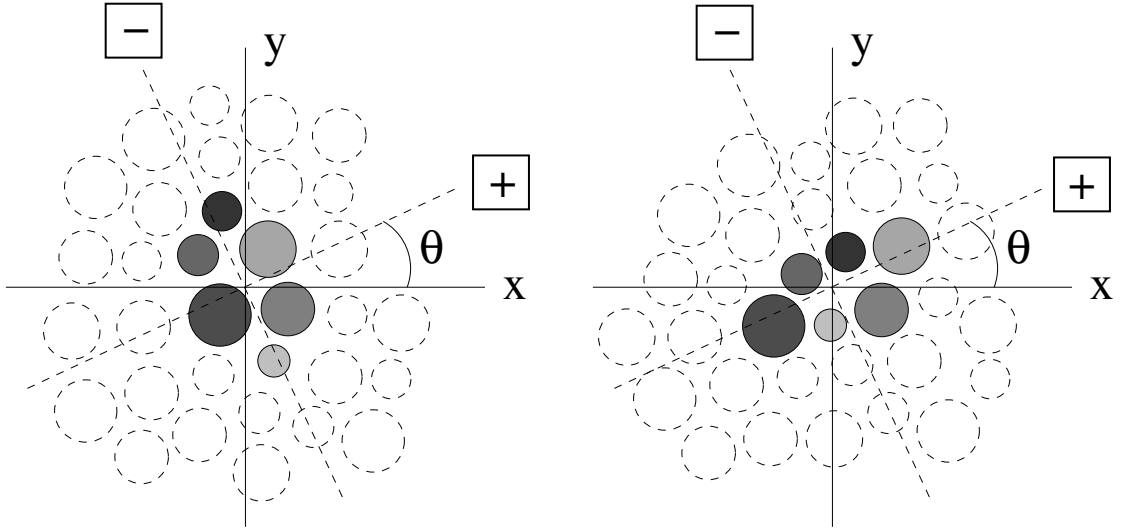


Figure 4.1: A schematic illustration of an STZ as a two-state system. An STZ can flip between its “+”- and “-”-state, elongating the material in either of the two perpendicular directions.

Fig. 4.1 is a schematic illustration of an STZ in its two different states. Physically, these two states represent the elongation of the STZ along either a “+”-axis or a “-”-axis, where the “+” and “-” axes are perpendicular to each other and rotated an angle θ in the counter-clockwise direction relative to the x and y axes, respectively. Note that the choice of the labels “+” and “-” is arbitrary; there is no physical difference between the two states, since rotating the coordinate system by $\pi/2$ would reverse the labels.

The STZs are assumed to transform between states at a rate that depends on the local deviatoric stress. To be more precise, consider the rotated coordinate system shown in Fig. 2.1, where the x' and y' axes have been rotated an angle θ in the counter-clockwise direction relative to the x and y axes, respectively. That means that the x' -axis is aligned with the “+”-axis, as are the y' and “-” axes.

Using the primed notation of Section 2.2,

$$s'_\theta = s \cos 2\theta - \tau \sin 2\theta \quad (4.1)$$

is the deviatoric stress along the y' (or “−”) axis (the subscript θ is just a reminder that the value of s' depends on the angle θ of the rotated coordinate system).

Given this, define the average rate at which STZs will flip from the “+”-state to the “−”-state as $R[s'_\theta]$. Falk and Langer [30] suggested that the rate should be proportional to an expression resembling a Boltzmann factor used in thermally activated processes,

$$R[s'_\theta] = R_0 \exp \left[-\frac{\Delta V^*(s'_\theta)}{v_f} \right] \quad \text{with} \quad \Delta V^*(s'_\theta) = V_0^* \exp \left(-\frac{s'_\theta}{\bar{\mu}} \right), \quad (4.2)$$

where R_0 is an attempt frequency, v_f is the free volume per particle (and the quantity analogous to the temperature),¹ and $\Delta V^*(s'_\theta)$ is the excess free volume needed to activate a transition from a “+” to a “−” state given a stress s'_θ . The function $\Delta V^*(s'_\theta)$ decreases with respect to the stress, which means that as the stress grows larger, less and less free volume is needed to activate a transition. This function was chosen to be exponential rather than linear since in the limit of large stresses, the needed excess volume should approach zero rather than become negative. The constant $\bar{\mu}$ sets the stress scale and basically determines the yield stress. A linearized version of Eq. (4.2) was used for the simulations in this dissertation; this approximation, used in the “quasi-linear” version of the model, will be applied and explained later.

¹Apparently, the use of the free volume as an internal state variable is considered controversial by some; see for example [67] and references therein. The sense in which the free volume takes part in the STZ theory is perhaps different from the conventional usage by Spaepen and others (see Chapter 3); in the STZ description, it seems to be closer in spirit to an effective temperature, where the STZs arise due to fluctuations in the material.

As mentioned above, STZs will flip from their “+”-state to the “-”-state at a rate of $R[s'_\theta]$. Since the stress along the x' (or “+”) axis is given by $s'_{\theta-\pi/2} = -s'_\theta$, the average rate at which STZs will flip from the “-” to the “+” state must be given by $R[-s'_\theta]$. As a shorthand, write

$$R_\theta^+ \equiv R[s'_\theta] \quad \text{and} \quad R_\theta^- \equiv R[s'_{\theta-\pi/2}] = R[-s'_\theta]. \quad (4.3)$$

It follows that

$$R_{\theta\pm\pi/2}^- = R_\theta^+. \quad (4.4)$$

In the continuum formulation of the STZ theory, individual STZs are averaged out. Let $n(\theta)$ be the local angular distribution of STZs. More precisely, let $n(\theta)d\theta$ be proportional to the number of STZs per area (in two dimensions) with their “+”-axis lying in the interval $[\theta, \theta + d\theta]$. The corresponding distribution for the STZs in the “-” state is given by $n(\theta - \pi/2)$ or $n(\theta + \pi/2)$; since the STZs are directors, $n(\theta)$ has a period of π , or $n(\theta) \equiv n(\theta + m\pi)$ for all integers m . Introducing another shorthand, let

$$n_\theta^+ \equiv n(\theta) \quad \text{and} \quad n_\theta^- \equiv n(\theta - \pi/2). \quad (4.5)$$

With the rate R and the density $n(\theta)$ properly defined, the rate equations for the latter can be written as

$$\dot{n}_\theta^+ = R_\theta^- n_\theta^- - R_\theta^+ n_\theta^+ + \left(\frac{n_\infty}{2} - n_\theta^+\right) \Gamma, \quad (4.6a)$$

$$\dot{n}_\theta^- = R_\theta^+ n_\theta^+ - R_\theta^- n_\theta^- + \left(\frac{n_\infty}{2} - n_\theta^-\right) \Gamma. \quad (4.6b)$$

In both of the above equations, the two first terms take into account only the transformation, or flipping, of STZs. In the last term, $(n_\infty/2)\Gamma$ is responsible for the creation of new STZs, while $n_\theta^\pm\Gamma$ represents the annihilation of old ones.

The rate at which STZs are created and annihilated is controlled by Γ , which is later assumed to be proportional to Q , the energy dissipated through plastic work. While the rate of annihilation is proportional to the number of STZs present, the rate of creation is just set proportional to a constant, n_∞ . It was chosen so that it would be the steady-state value for the total number of STZs, $n_\theta^- + n_\theta^+$, at the angle θ , as will become clear in the following discussion.

It has proven convenient to rewrite Eqs. (4.6) using the following definitions:

$$n_\theta^{\text{tot}} \equiv n_\theta^- + n_\theta^+, \quad n_\theta^\Delta \equiv n_\theta^- - n_\theta^+, \quad (4.7a)$$

$$\mathcal{C}_\theta \equiv \frac{R_\theta^+ + R_\theta^-}{2R_0}, \quad \mathcal{S}_\theta \equiv \frac{R_\theta^+ - R_\theta^-}{2R_0}, \quad \text{and} \quad \mathcal{T}_\theta \equiv \frac{\mathcal{S}_\theta}{\mathcal{C}_\theta}. \quad (4.7b)$$

It is important to understand that n_θ^{tot} represents *all* the STZs at the angle θ . To repeat, n_θ^{tot} includes *all* the STZs with either their “+”-axis or their “-”-axis in the interval $\theta \in [\theta, \theta + d\theta)$. Subsequently, when referring to “the STZs at an angle θ ”, n_θ^{tot} is what is meant.

Using Eqs. (4.7), one can write

$$\begin{aligned} W_\theta &\equiv R_\theta^+ n_\theta^+ - R_\theta^- n_\theta^- \\ &= R_0(\mathcal{S}_\theta n_\theta^{\text{tot}} - \mathcal{C}_\theta n_\theta^\Delta) \\ &= R_0 \mathcal{C}_\theta (\mathcal{T}_\theta n_\theta^{\text{tot}} - n_\theta^\Delta), \end{aligned} \quad (4.8)$$

where the symbol W_θ has been defined for later convenience. Eqs. (4.6) can now be written as

$$\dot{n}_\theta^{\text{tot}} = (n_\infty - n_\theta^{\text{tot}})\Gamma, \quad (4.9a)$$

$$\dot{n}_\theta^\Delta = 2W_\theta - n_\theta^\Delta \Gamma. \quad (4.9b)$$

As promised earlier, Eq. (4.9a) shows that the steady-state value of n_θ^{tot} , the total number of STZs at the angle θ , equals n_∞ . Notice that if n_θ^{tot} is initially uniform

with respect to θ (a reasonable assumption), Eq. (4.9a) will keep it uniform at all later times (this does *not* mean that the average direction in which the STZs are aligned is uniform; n_θ^Δ keeps track of that). With this assumption define

$$n^{\text{tot}} \equiv \frac{2}{\pi} \int_{-\pi/4}^{\pi/4} n_\theta^{\text{tot}} d\theta = n_\theta^{\text{tot}}, \quad (4.10)$$

where the fraction in front of the integral is a normalization factor.

4.1.1 The Plastic Strain Rate

The goal now is to find the plastic strain rate tensor D_{ij}^{pl} . Define $\Delta\varepsilon$ to be the strain increment occurring in any space containing a single transforming STZ. Thus if an STZ flips from the “+” to the “-” state, the strain along the “-”-axis increases by $\Delta\varepsilon$ in that region, while the strain along the “+”-axis decreases by the same amount. The latter statement implies that STZ transformations, and thus plastic deformations, are area conserving. The creation and annihilation of STZs do not contribute to the plastic strain.

On the mesoscopic scale (that is, in the continuum formulation), the plastic strain rate along the y' -axis caused by n_θ^{tot} , the STZs at θ , is given by

$$\Delta\varepsilon b^2 W_\theta d\theta \left(\begin{array}{c} \text{plastic strain rate} \\ \text{along } y'\text{-axis} \\ \text{due to STZs at } \theta \end{array} \right), \quad (4.11)$$

where b^2 is the typical size of an STZ [52] (b^2 is sometimes referred to as V_z [30, 47]). Since n_θ^\pm are number densities, W_θ is the net rate of STZs per area at θ that flip from the “+”-state to the “-”-state. Multiplying this net rate by b^2 gives the fraction of area that, during one unit of time, has experienced a transforming STZ. Including the factor $\Delta\varepsilon$ then gives the average increment of strain per unit time; this is the plastic strain rate.

Eq. (4.11) only accounts for the STZs that lie in the interval $[\theta, \theta + d\theta)$, and it gives the plastic strain along y' rather than y . Consider a strain tensor $\boldsymbol{\varepsilon}$ describing pure shear (that is, the strain tensor is traceless) along the y' -axis:

$$\boldsymbol{\varepsilon} = \begin{pmatrix} -a & 0 \\ 0 & a \end{pmatrix}'. \quad (4.12)$$

As explained in Section 2.2, the prime on the matrix means that the components are written relative to the (x', y') basis, which is rotated an angle θ in the counter-clockwise direction relative to the (x, y) basis. The tensor $\boldsymbol{\varepsilon}$ describes a strain $\varepsilon'_{yy} = a$ along the y' -axis, and a strain $\varepsilon'_{xx} = -a$ along the x' -axis, while $\varepsilon'_{xy} = 0$. Transforming the coordinates of $\boldsymbol{\varepsilon}$ to the (x, y) basis, like in Eq. (2.15), the tensor in Eq. (4.12) can be written as

$$\boldsymbol{\varepsilon} = \begin{pmatrix} -a \cos 2\theta & -a \sin 2\theta \\ -a \sin 2\theta & a \cos 2\theta \end{pmatrix} = -a \mathbf{D}^\theta, \quad (4.13)$$

where

$$\mathbf{D}^\theta = \begin{pmatrix} \cos 2\theta & \sin 2\theta \\ \sin 2\theta & -\cos 2\theta \end{pmatrix} \quad (4.14)$$

is the two-dimensional director matrix [68]. This means that the tensor $\boldsymbol{\varepsilon}$ describes a system with a strain of $\varepsilon_{yy} = a \cos 2\theta$ along the y -axis, $\varepsilon_{xx} = -a \cos 2\theta$ along the x -axis, and with $\varepsilon_{xy} = -a \sin 2\theta$.

Applying the same technique to Eq. (4.11), the tensor

$$\mathbf{D}_\theta^{\text{pl}} = \begin{pmatrix} -\Delta\varepsilon b^2 W_\theta & 0 \\ 0 & \Delta\varepsilon b^2 W_\theta \end{pmatrix}' \quad (4.15)$$

describes the plastic strain rate due to the STZs at θ in the basis (x', y') . Writing it in the basis (x, y) , this becomes

$$D_{\theta,ij}^{\text{pl}} = -\Delta\varepsilon b^2 W_\theta \mathcal{D}_{ij}^\theta \quad (\text{or } \mathbf{D}_\theta^{\text{pl}} = -\Delta\varepsilon b^2 W_\theta \mathbf{D}^\theta). \quad (4.16)$$

In order to find the plastic strain resulting from all the STZs at all angles, all that is left to do is to integrate $\mathbf{D}_\theta^{\text{pl}}$ over θ :

$$D_{ij}^{\text{pl}} = \int_{-\pi/4}^{\pi/4} D_{\theta,ij}^{\text{pl}} d\theta = \int_{-\pi/4}^{\pi/4} -\Delta\varepsilon b^2 W_\theta \mathcal{D}_{ij}^\theta d\theta. \quad (4.17)$$

4.1.2 Introducing the STZ variables

The distribution function n_θ^Δ represents the skewness in the alignment of the STZs. Having written the plastic strain rate (4.11) as a traceless tensor D_{ij}^{pl} , it seems reasonable to do the same with n_θ^Δ , considering that the expressions for n_θ^Δ and W_θ both appear in Eq. (4.9b). Just as in Eq. (4.17), define

$$n_{ij} \equiv \int_{-\pi/4}^{\pi/4} -n_\theta^\Delta \mathcal{D}_{ij}^\theta d\theta. \quad (4.18)$$

On a side note, the Fourier series for $n(\theta)$ can be written as

$$n(\theta) = \sum_{m=-\infty}^{\infty} c_m e^{i2m\theta} = \sum_{m=-\infty}^{\infty} a_m \cos 2m\theta + b_m \sin 2m\theta, \quad (4.19a)$$

$$c_m = \frac{1}{\pi} \int_{-\pi/2}^{\pi/2} n(\theta) e^{-i2m\theta} d\theta, \quad a_m = \frac{c_m + c_{-m}}{2}, \quad b_m = \frac{i(c_m - c_{-m})}{2}, \quad (4.19b)$$

where $a_m, b_m \in \mathbb{R}$ and $c_{-m} = c_m^*$ since $n(\theta)$ is a real function. The prefactor and limits of integration take into account that $n(\theta)$ has a period of π . In terms of $n(\theta)$,

$$n_{\text{tot}} = \frac{2}{\pi} \int_{-\pi/2}^{\pi/2} n(\theta) d\theta, \quad n_{ij} = \int_{-\pi/2}^{\pi/2} n(\theta) \mathcal{D}_{ij}^\theta d\theta, \quad (4.20)$$

from which it follows that $n_{\text{tot}} = 2a_0$, $n_{xx} = \pi a_1$, and $n_{xy} = \pi b_1$; in other words, n_{tot} and n_{ij} captures the first two moments of the Fourier series of $n(\theta)$.

Eqs. (4.17) and (4.18) can now be used to write Eq. (4.9b) in tensor form; if the latter equation is multiplied by $-\mathcal{D}_{ij}^\theta$ and integrated over the quadrant $\theta \in [-\pi/4, \pi/4)$, one gets

$$\dot{n}_{ij} = \frac{2}{\Delta\varepsilon b^2} D_{ij}^{\text{pl}} - n_{ij} \Gamma. \quad (4.21)$$

Define the STZ variables Λ and Δ_{ij} as n^{tot} and n_{ij} normalized by the steady-state value n_∞ ,

$$\Lambda \equiv \frac{n^{\text{tot}}}{n_\infty} \quad \text{and} \quad \Delta_{ij} \equiv \frac{n_{ij}}{n_\infty}. \quad (4.22)$$

Applying Eqs. (4.22) to (4.9a) and (4.21), it follows that

$$\dot{\Lambda} = \Gamma(1 - \Lambda), \quad (4.23a)$$

$$\dot{\Delta}_{ij} = \frac{1}{\epsilon_0} D_{ij}^{\text{pl}} - \Gamma \Delta_{ij}, \quad (4.23b)$$

where

$$\epsilon_0 \equiv \frac{1}{2} \Delta \varepsilon b^2 n_\infty \quad (4.24)$$

is a parameter that depends on the size and the steady-state density of the STZs, as well as the amount of strain they induce during transformation.

4.1.3 The Quasi-Linear Model

Before Eqs. (4.23) can be considered complete, the plastic strain rate D_{ij}^{pl} needs to be written in terms of Λ and Δ_{ij} . At this point, the plastic strain rate takes the form

$$\frac{1}{\epsilon_0} D_{ij}^{\text{pl}} = \int_{-\pi/4}^{\pi/4} -\mathcal{D}_{ij}^\theta \frac{1}{\tau_0^\theta} \left(\mathcal{T}_\theta \frac{n^{\text{tot}}}{n_\infty} - \frac{n_\theta^\Delta}{n_\infty} \right) d\theta, \quad (4.25)$$

where

$$\frac{1}{\tau_0^\theta} \equiv 2R_0 \mathcal{C}_\theta \quad (4.26)$$

is a time factor that adjusts the rate of plastic strain as a function of the magnitude and direction of the deviatoric stress. It has been shown that if $1/\tau_0^\theta$ becomes small as the stress drops to zero, the material is able to preserve some of the strain history in its internal variables [30]. The presence of this ‘‘internal memory’’ leads to hysteresis when a material is repeatedly loaded and unloaded. To simplify the

model, it is assumed that constant:

$$\tau_0^\theta \approx \tau_0 = \text{constant} . \quad (4.27)$$

The justification for using this approximation is that the simulations presented in this dissertation did not perform load cycling. Nevertheless, the results from the numerical simulations presented in Chapters 6 and 7 showed that there was inhomogeneous plastic flow. This means that some areas in the interior of the material was able to unload while the ends were strained at a constant rate. The approximation (4.27) is believed not to have had a qualitative impact on the results of Chapters 6 and 7, but it might prove essential when considering more complex processes.

The plastic strain rate can now be written as

$$\frac{1}{\epsilon_0} D_{ij}^{\text{pl}} = \frac{1}{\tau_0} (\mathcal{T}_{ij} \Lambda - \Delta_{ij}) , \quad (4.28)$$

where

$$\mathcal{T}_{ij} = \int_{-\pi/4}^{\pi/4} -\mathcal{D}_{ij}^\theta \mathcal{T}_\theta d\theta . \quad (4.29)$$

One more approximation will be made to the model, namely that \mathcal{T}_θ is linear in s'_θ . This combined with Eq. (4.27) will be referred to as the “quasi-linear” approximation.

So far, the form of the rate $R[s'_\theta]$ has not been specified. Choosing the rate (4.2) suggested by Falk and Langer [30], and inserting it into Eqs. (4.7b), one can write

$$\mathcal{C}_\theta = \exp \left[-\frac{V_0^*}{v_f} \cosh \left(\frac{s'_\theta}{\bar{\mu}} \right) \right] \cosh \left[\frac{V_0^*}{v_f} \sinh \left(\frac{s'_\theta}{\bar{\mu}} \right) \right] , \quad (4.30a)$$

$$\mathcal{S}_\theta = \exp \left[-\frac{V_0^*}{v_f} \cosh \left(\frac{s'_\theta}{\bar{\mu}} \right) \right] \sinh \left[\frac{V_0^*}{v_f} \sinh \left(\frac{s'_\theta}{\bar{\mu}} \right) \right] , \quad (4.30b)$$

$$\mathcal{T}_\theta = \tanh \left[\frac{V_0^*}{v_f} \sinh \left(\frac{s'_\theta}{\bar{\mu}} \right) \right] . \quad (4.30c)$$

By Taylor-expanding Eq. (4.30c) around $s'_\theta = 0$, one gets

$$\mathcal{T}_\theta = \left(\frac{V_0^*}{v_f \bar{\mu}} \right) s'_\theta + \mathcal{O}[(s'_\theta)^3]. \quad (4.31)$$

The approximation $\mathcal{T}_\theta \approx (V_0^*/v_f \bar{\mu}) s'_\theta$ becomes more accurate as V_0^*/v_f tends to zero (the value of $\bar{\mu}$ is irrelevant because the stress typically takes on values in the range $s'_\theta \in [-\bar{\mu}, \bar{\mu}]$). Before inserting this approximation into Eq. (4.29), one can rewrite the stress s'_θ to further simplify the expression.

The maximum shear stress (or the positive principal stress of a traceless or deviatoric stress tensor) is an invariant of the stress tensor given by

$$\bar{s} \equiv \sqrt{\frac{1}{2} s_{kl} s_{kl}} = \sqrt{s^2 + \tau^2} \quad (4.32)$$

(some texts write \bar{s} as τ_{\max}). Define Φ to be the principal angle of stress so that when the components of the deviatoric stress tensor is written in a basis that is rotated an angle Φ in the counter-clockwise direction, $s'_\Phi \equiv \bar{s}$ and $\tau'_\Phi = 0$ ($\Phi = 0$ means that $s \equiv s_{yy} = -s_{xx} = \bar{s}$ and $\tau \equiv s_{xy} = 0$, that is, the principal stress axes are parallel to the x and y axes). Define

$$\Theta \equiv \theta - \Phi. \quad (4.33)$$

Since $\theta = \Theta + \Phi$, Θ is the angle that separates θ and the angle of the principal stress axes, Φ (see Fig. 4.2). Since

$$s'_\Phi = s \cos 2\Phi - \tau \sin 2\Phi = \bar{s} \quad (4.34a)$$

$$\tau'_\Phi = \tau \cos 2\Phi + s \sin 2\Phi = 0, \quad (4.34b)$$

it follows, using Eq. (4.1), that

$$s'_\theta = s'_{\Theta+\Phi} = \bar{s} \cos 2\Theta. \quad (4.35)$$

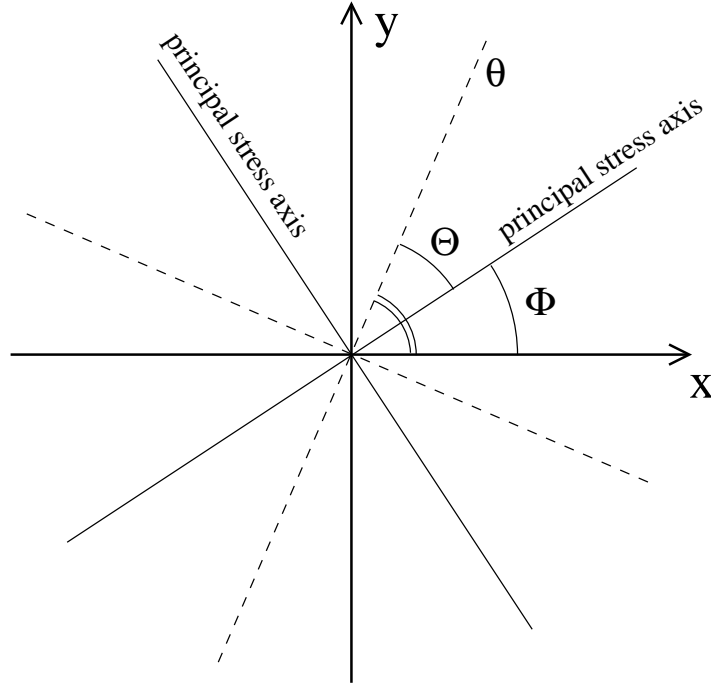


Figure 4.2: The angle Θ is defined as the difference between Φ , the principal stress axis, and θ , the current angle, $\theta = \Phi + \Theta$.

Eq. (4.29) now reads

$$\begin{aligned}
 \mathcal{T}_{ij} &\approx \left(\frac{V_0^*}{v_f \bar{\mu}} \right) \bar{s} \int_{-\pi/4-\Phi}^{\pi/4-\Phi} -\mathcal{D}_{ij}^{\Theta+\Phi} \cos 2\Theta d\Theta \\
 &= -\frac{\pi}{4} \left(\frac{V_0^*}{v_f \bar{\mu}} \right) \bar{s} \mathcal{D}_{ij}^{\Phi} \\
 &= \lambda s_{ij}, \tag{4.36}
 \end{aligned}$$

where

$$\lambda \equiv \frac{\pi V_0^*}{4 v_f \bar{\mu}}. \tag{4.37}$$

The last equality of Eq. (4.36) used that

$$s_{ij} = -\bar{s} \mathcal{D}_{ij}^{\Phi}, \tag{4.38}$$

which can be deduced from the last expression in Eq. (2.15). The plastic strain

rate now reads

$$\frac{1}{\epsilon_0} D_{ij}^{\text{pl}} = \frac{1}{\tau_0} (\lambda s_{ij} \Lambda - \Delta_{ij}) . \quad (4.39)$$

Eqs. (4.23) together with (4.39) give the equations of motion for the STZ variables Λ and Δ_{ij} in the quasi-linear model.

4.2 Plastic Work and Dissipation

This section discusses the nature of the plastic work and derives an expression for Γ , the rate of creation and annihilation of STZs. This derivation is based on Pechenik's idea that Γ should be proportional to Q , the dissipative part of the plastic work [69, 70]. He pursued this conjecture after the current author discovered that the original expression for Γ , proportional to the rate of all the plastic work (not just Q), would sometimes turn negative in parts of the material during unloading, leading to non-physical effects [71].

The energy-balance equation for the plastic work is

$$D_{ij}^{\text{pl}} s_{ij} = \frac{D}{Dt} \psi^{\text{pl}}(\Lambda, \Delta_{ij}) + Q(s_{ij}, \Lambda, \Delta_{ij}) , \quad (4.40)$$

where the left-hand side is the rate of plastic work done on the system. On the right-hand side, ψ^{pl} is the recoverable plastic energy and Q is the rate of dissipation due to the plastic work.

Pechenik's idea was that Γ , which is proportional to the rate of creation and annihilation of STZs, and Q , which is the (positive) rate of energy dissipation due to plastic deformation, should be similar functions. He thus made the conjecture that

$$Q(s_{ij}, \Lambda, \Delta_{ij}) = \frac{a(\Lambda)}{\lambda} \Gamma(s_{ij}, \Lambda, \Delta_{ij}) . \quad (4.41)$$

Inserting this into Eq. (4.40) gives ²

$$D_{ij}^{\text{pl}} s_{ij} = \frac{\partial \psi^{\text{pl}}}{\partial \Delta_{ij}} \frac{\mathcal{D} \Delta_{ij}}{\mathcal{D} t} + \frac{\partial \psi^{\text{pl}}}{\partial \Lambda} \frac{D \Lambda}{D t} + \frac{a(\Lambda)}{\lambda} \Gamma. \quad (4.42)$$

Inserting Eqs. (4.23) gives

$$D_{ij}^{\text{pl}} s_{ij} = \frac{\partial \psi^{\text{pl}}}{\partial \Delta_{ij}} \left(\frac{1}{\epsilon_0} D_{ij}^{\text{pl}} - \Gamma \Delta_{ij} \right) + \frac{\partial \psi^{\text{pl}}}{\partial \Lambda} \Gamma (1 - \Lambda) + \frac{a(\Lambda)}{\lambda} \Gamma. \quad (4.43)$$

Solving for Γ yields

$$\Gamma = \frac{\lambda D_{ij}^{\text{pl}} \left(s_{ij} - \frac{1}{\epsilon_0} \frac{\partial \psi^{\text{pl}}}{\partial \Delta_{ij}} \right)}{a(\Lambda) + \lambda \frac{\partial \psi^{\text{pl}}}{\partial \Lambda} (1 - \Lambda) - \lambda \frac{\partial \psi^{\text{pl}}}{\partial \Delta_{ij}} \Delta_{ij}}. \quad (4.44)$$

Since Γ is proportional to the rate of dissipation, it has to be positive. The rate of plastic deformation is given by Eq. (4.39); thus the numerator of Eq. (4.44) can only be guaranteed to be positive if

$$\frac{\partial \psi^{\text{pl}}}{\partial \Delta_{ij}} = \epsilon_0 \frac{\Delta_{ij}}{\lambda \Lambda}. \quad (4.45)$$

Integrating ψ^{pl} for each set of indices and combining the results give

$$\psi^{\text{pl}} = \frac{\epsilon_0 \bar{\Delta}^2}{\lambda \Lambda} + \psi_0^{\text{pl}}(\Lambda) \quad (4.46)$$

where $\bar{T}^2 \equiv (1/2) T_{ij} T_{ij}$ for any tensor T_{ij} , and also $\bar{T}^2 = T_s^2 + T_\tau^2$ if T_{ij} is symmetric and traceless (which is the case for both Δ_{ij} and D_{ij}^{pl}). If $a(\Lambda)$ is chosen as

$$a(\Lambda) = \epsilon_0 (1 + \Lambda) - \lambda \frac{d\psi_0^{\text{pl}}(\Lambda)}{d\Lambda} (1 - \Lambda), \quad (4.47)$$

then

$$\Gamma = \frac{2\Lambda\tau_0 \left(\frac{1}{\epsilon_0} \bar{D}^{\text{pl}} \right)^2}{(1 + \Lambda)(\Lambda^2 - \bar{\Delta}^2)}, \quad (4.48)$$

²If Δ_{ij} is traceless and symmetric then, technically, the first term on the right-hand side of Eq. (4.42) should have a factor of 1/2. This factor would propagate into Eqs. (4.43) and (4.44), and Eq. (4.45) would have a factor of 2 on the right-hand side. Fortunately, the remaining equations would be unaffected, which means that the expressions for Γ , a , ψ^{pl} , and ψ_0^{pl} do not depend on whether or not the tensor Δ_{ij} is symmetric and traceless.

which is always positive.

It is not obvious what the form of $\psi_0^{\text{pl}}(\Lambda)$ should be. Choosing

$$\psi_0^{\text{pl}}(\Lambda) = \frac{\epsilon_0}{\lambda} \Lambda \quad (4.49)$$

gives

$$a(\Lambda) = 2\epsilon_0 \Lambda \quad (4.50)$$

and

$$\psi^{\text{pl}} = \frac{\epsilon_0}{\lambda} \left(\frac{\Lambda^2 + \bar{\Delta}^2}{\Lambda} \right). \quad (4.51)$$

This choice is enticing, since it makes Γ proportional to the rate of dissipation per STZ.

So far, dividing the plastic work into plastic dissipation and stored plastic energy has not been much more than a mathematical exercise. What exactly is “stored plastic energy”? According to the STZ model, plastic deformation occurs when the STZs flip. This deformation, causing the internal stress distribution to change, will then flip even more STZs *as well as* creating new ones and annihilating existing ones. It takes energy to flip an STZ. The work done on it could even be considered reversible, if one could make the STZ flip back again. Then again, the STZ could make it back to its original position without releasing any energy by being annihilated and recreated. Since, theoretically, one could regain the energy in the flipped STZ if one could make all the STZ flip back again without any of them being annihilated, the energy stored in the flipped STZs seem like a reasonable interpretation of the stored plastic energy. In practice, though, some of the stored plastic energy would probably be lost if the STZs were to flip back, since this flipping would cause further deformations and thus more creation and annihilation of STZs. The plastic dissipation Q can be interpreted as the energy lost when an

STZ is annihilated and recreated.

Various terms exist to describe strain response in amorphous solids, although they are not always used consistently; the following is an effort to summarize the explanations given in [21, 28, 55, 72]:

Homogeneous flow :

- **Elastic** response is reversible upon removal of stress, time independent (instantaneous), and linear with respect to the stress.
- **Anelastic** response is reversible upon removal of stress (although some annealing at an elevated temperature might be necessary to fully recover the anelastic strain), and time dependent (anelasticity is sometimes called “delayed elasticity”). There can be both linear and non-linear anelastic strain, but only the former will be considered below.
- **Visco-elastic** or **visco-plastic** response is permanent and time dependent. This is often just referred to as homogeneous (permanent) plastic flow. The relationship between the stress and the strain rate can be both linear and non-linear, the latter usually occurring at higher stresses.

Inhomogeneous flow is caused by plastic flow confined to thin shear bands. The stress is usually strain rate insensitive.

In addition, the term “inelastic” usually refers to everything except the linear elastic response. Note, though, that “plastic” and “inelastic” are often used interchangeably, as is the case in this manuscript.

Consider a material specimen undergoing homogeneous flow while subjected to a constant stress. The sample will immediately respond elastically with a strain proportional to the stress (the speed of the elastic response is only limited by the

speed of sound in the material). The specimen will then continue to strain, but more slowly. If the stress is low (and especially if the temperature is low, too), the material will come to a halt after a while, otherwise it will settle into a steady-state homogeneous plastic flow.

Imagine now that the stress is removed. The elastic strain is immediately recovered. The sample will then continue to contract for a while, recovering the anelastic strain. When the strain recovery has converged, only the permanent plastic strain remains.

The classification of the strain response given above seems to match well with the deformation mechanisms seen in the STZ theory. The linear elastic response is in the model by construction; the next section shows how it is mathematically combined with the STZ description. The anelastic strain seems to match up well with the stored plastic energy ψ^{pl} , or equivalently, the flipped STZs. When the stress is released, the work that was needed to flip the STZs can be recovered as the zones transform back to their original position. The permanent deformation occurs when STZs are annihilated, preventing them from flipping back. The dissipated energy Q is thus the stored plastic energy that was lost when the STZs were annihilated.

Again, notice the ambiguous use of the word “plastic”. In Eq. (4.40), both the reversible (anelastic) and dissipative (permanent plastic) terms contribute to the plastic (inelastic) work. In this dissertation, the term “plastic deformation” refers to both the anelastic and permanent plastic response.

4.3 Combining the STZ theory with Linear Elasticity

So far, this chapter has focused on formulating a continuum description of plastic deformation starting from a microscopic point of view. This description, represented by Eqs. (4.23), (4.39), and (4.48), can now be combined with the linear elastic framework (2.55) and (2.56) presented earlier:

$$\left(\frac{1-\nu_2}{1+\nu_2}\right) \frac{1}{2\mu} \frac{Dp}{Dt} = -\frac{1}{2} \nabla \cdot \mathbf{v}, \quad (4.52a)$$

$$\frac{1}{2\mu} \frac{\mathcal{D}s_{ij}}{\mathcal{D}t} = \tilde{D}_{ij}^{\text{tot}} - D_{ij}^{\text{pl}}, \quad (4.52b)$$

$$\rho \frac{Dv_i}{Dt} = \frac{\partial s_{ji}}{\partial x_j} - \frac{\partial p}{\partial x_i}, \quad (4.52c)$$

$$\frac{D\Lambda}{Dt} = \Gamma(1-\Lambda), \quad (4.52d)$$

$$\frac{\mathcal{D}\Delta_{ij}}{\mathcal{D}t} = \frac{1}{\epsilon_0} D_{ij}^{\text{pl}} - \Gamma \Delta_{ij}, \quad (4.52e)$$

with

$$\tilde{D}_{ij}^{\text{tot}} = \frac{1}{2} \left(\frac{\partial v_i}{\partial x_j} + \frac{\partial v_j}{\partial x_i} \right) - \frac{1}{2} \nabla \cdot \mathbf{v}, \quad \frac{1}{\epsilon_0} D_{ij}^{\text{pl}} = \frac{1}{\tau_0} (\lambda \Lambda s_{ij} - \Delta_{ij}), \quad (4.52f)$$

and

$$\Gamma = \frac{2\Lambda\tau_0 \left(\frac{1}{\epsilon_0} \bar{D}^{\text{pl}}\right)^2}{(1+\Lambda)(\Lambda^2 - \bar{\Delta}^2)}. \quad (4.52g)$$

Eqs. (4.52) are referred to as the quasi-linear tensorial STZ model in two dimensions. When combined with boundary conditions, it can be used to describe both the elastic and plastic dynamics of an amorphous solid.

4.4 A Scalar Version of the STZ Model

Chapter 3 explored a zero-dimensional version of the STZ model, which is valid when the system can be considered uniform throughout. Without the spatial

variation to worry about, the tensor notation of (4.52) can be eliminated, and the equations can be simplified a great deal. More importantly, one can apply a constant strain rate, as well as boundary conditions, without introducing any geometrical effects. Note that since the equations of motion only contain the gradients of the velocities, and not the velocities themselves, these gradients can easily be included in the zero-dimensional description as long as they are uniform throughout the system. Since the stresses, as well as Λ and Δ_{ij} , are used explicitly in the equations, their gradients all have to be set to zero.

Aligning the y -axis along the direction of principal stress, one can define

$$s \equiv s_{yy} = -s_{xx}, \quad \Delta \equiv \Delta_{yy} = -\Delta_{xx}, \quad D^{\text{pl}} \equiv D_{yy}^{\text{pl}} = -D_{xx}^{\text{pl}}, \quad (4.53a)$$

$$s_{xy} = \Delta_{xy} = D_{xy}^{\text{pl}} = 0, \quad (4.53b)$$

$$\frac{\partial s_{ij}}{\partial x_k} = \frac{\partial \Delta_{ij}}{\partial x_k} = \frac{\partial \Lambda}{\partial x_k} = 0 \quad \forall i, j, k \in \{x, y, z\}, \quad (4.53c)$$

and

$$D^{\text{tot}} \equiv D_{yy}^{\text{tot}} = \frac{\partial v_y}{\partial y}, \quad D^{\text{el}} \equiv D_{yy}^{\text{el}}. \quad (4.53d)$$

Further,

$$\bar{s} = |s| \quad \text{and} \quad \bar{\Delta} = |\Delta|. \quad (4.53e)$$

Using Eqs. (4.53), Eqs. (4.52) now read

$$\dot{\Lambda} = \Gamma(1 - \Lambda) \quad (4.54a)$$

$$\dot{\Delta} = w - \Gamma\Delta \quad (4.54b)$$

$$w \equiv \frac{1}{\epsilon_0} D^{\text{pl}} = \frac{1}{\tau_0} (\lambda s \Lambda - \Delta) \quad (4.54c)$$

$$\Gamma = \tau_0 \left(\frac{2\Lambda}{1 + \Lambda} \right) \frac{w^2}{\Lambda^2 - \Delta^2}. \quad (4.54d)$$

Since there are no gradients in s , Δ , or Λ , there are no advective terms. Further, since $\partial_x v_y = \partial_y v_x = 0$, there are no rotational derivatives either.

If the system is subjected to a constant strain rate rather than to a constant stress, an additional requirement is needed to determine the hydrostatic pressure p . The numerical simulations in this dissertation used that $\sigma_{xx} = 0$, which means that $p = -s$ and $\sigma_{yy} = 2s$. In this case, Eq. (2.54a) becomes

$$\varepsilon_{xx} = -\frac{s}{2\mu} \frac{2\nu_2}{1 + \nu_2}, \quad (4.55a)$$

$$\varepsilon_{yy} = \frac{s}{2\mu} \frac{2}{1 + \nu_2}. \quad (4.55b)$$

According to Eq. (2.51), the total rate of deformation is assumed to be a linear combination of the elastic and plastic parts, $D^{\text{tot}} \approx D^{\text{el}} + D^{\text{pl}}$. If the total strain rate D^{tot} is held constant, then Eq. (2.53) with the time derivative of Eq. (4.55b) yields

$$\begin{aligned} \dot{s} &= \mu(1 + \nu_2)(D^{\text{tot}} - D^{\text{pl}}) \\ &= \mu(1 + \nu_2)(D^{\text{tot}} - \epsilon_0 w). \end{aligned} \quad (4.56)$$

Eqs. (4.54) and (4.56) are referred to as the zero-dimensional, quasi-linear STZ model.

4.5 Energy Balance

When a force applied to a material causes it to accelerate or deform, the force is doing work on the material. Define the rate of this work as P_{external} (the P stands for “power”). For example, in the numerical simulations discussed in Chapter 7, a two-dimensional square specimen was subjected to uniaxial tension by applying a force F to the top edge. The force and the edge were parallel and perpendicular

to the y -axis, respectively. In this case, the rate of work done on the system was

$$P_{\text{external}} = F v_y, \quad (4.57)$$

where v_y was the velocity of the top edge. This section will discuss how the energy from applied work can be absorbed by a two-dimensional material as stored elastic and plastic energy, kinetic energy, and dissipation due to plastic deformations.

Using Eq. (2.54a) for the elastic strain, the stored elastic energy density is found to be

$$\psi^{\text{el}} = \frac{\sigma_{ij}\varepsilon_{ij}}{2} = \frac{1}{2\mu} \left[\left(\frac{1-\nu_2}{1+\nu_2} \right) p^2 + s^2 + \tau^2 \right]. \quad (4.58)$$

As seen in Section 4.2, the plastic work done on the system can be divided into two parts: the stored plastic energy density,

$$\psi^{\text{pl}} = \frac{\epsilon_0}{\lambda} \left(\frac{\Lambda^2 + \Delta_s^2 + \Delta_\tau^2}{\Lambda} \right), \quad (4.59)$$

and the dissipation due to plastic deformations,

$$Q = \frac{2\epsilon_0\Lambda}{\lambda}\Gamma, \quad \text{with } \Gamma = \frac{1}{\tau_0} \frac{2\Lambda}{1+\Lambda} \left[\frac{(\lambda\Lambda s - \Delta_s)^2 + (\lambda\Lambda\tau - \Delta_\tau)^2}{\Lambda^2 - \Delta_s^2 - \Delta_\tau^2} \right]. \quad (4.60)$$

The kinetic energy density is given by

$$\psi^{\text{kin}} = \frac{1}{2}\rho\mathbf{v}^2 = \frac{1}{2}\rho v_x^2 + \frac{1}{2}\rho v_y^2. \quad (4.61)$$

As discussed in Section 4.2, the rate of plastic work is given by Eq. (4.40). The rate of work due to the total deformation, $D_{ij}^{\text{tot}}\sigma_{ij}$, is found by adding the elastic work, since it is assumed that $D^{\text{tot}} = D^{\text{el}} + D^{\text{pl}}$:

$$D_{ij}^{\text{tot}}\sigma_{ij} = D_{ij}^{\text{el}}\sigma_{ij} + D_{ij}^{\text{pl}}\sigma_{ij} = \frac{D}{Dt}\psi^{\text{el}} + \frac{D}{Dt}\psi^{\text{pl}} + Q. \quad (4.62)$$

Both Eqs. (4.40) and (4.62) are true regardless of any assumptions about ψ_0^{pl} , like the one given in Eq. (4.49).

Eqs. (4.58), (4.59), and (4.61) give the elastic, plastic, and kinetic energy densities, while Eq. (4.60) gives the rate of plastically dissipated energy per area. These quantities are all densities, so to find the total rate at which energy is absorbed into the system, they must be integrated over the area of the material:

$$P_{\text{absorbed}} = \int_A \left[\frac{D}{Dt} (\psi^{\text{el}} + \psi^{\text{pl}} + \psi^{\text{kin}}) + Q \right] dA. \quad (4.63)$$

With all the energy accounted for, having energy balance means that the total rate of energy P_{external} supplied to the system, for example by the force mentioned earlier in this section, must equal the energy that is absorbed:

$$P_{\text{external}} = P_{\text{absorbed}}. \quad (4.64)$$

4.6 Reduced Units

By introducing reduced units, it is possible to eliminate some of the parameters from the equations and simultaneously rescale the variables making their range of values lie closer to unity, the latter being favorable in numerical procedures. In this dissertation, the variables were rescaled by the basic units \mathbb{S} (stress or pressure), \mathbb{L} (length), and \mathbb{T} (time):

$$\sigma_{ij} \rightarrow \frac{\sigma_{ij}}{\mathbb{S}} \quad \text{and} \quad v_i \rightarrow \frac{v_i}{\mathbb{S}} \quad (4.65)$$

(Λ and Δ_{ij} were already unit-less). By choosing these units to match parameters in the model,

$$\mathbb{S} = 1/\lambda, \quad \mathbb{T} = \tau_0, \quad \text{and} \quad \mathbb{L} = L, \quad (4.66)$$

where L is a length representative of the size of the system, those parameters were rescaled to unity:

$$\lambda \rightarrow \lambda \mathbb{S} = 1, \quad \tau_0 \rightarrow \tau_0 / \mathbb{T} = 1, \quad \text{and} \quad L \rightarrow L / \mathbb{L} = 1. \quad (4.67)$$

The introduction of reduced units would rescale the other parameters as well, for example

$$\rho \rightarrow \rho \frac{\mathbb{L}^2}{\mathbb{S}\mathbb{T}^2} \quad \text{and} \quad \mu \rightarrow \frac{\mu}{\mathbb{S}}. \quad (4.68)$$

In the remainder of the dissertation, all the equations will be written using reduced units.

4.7 Initial Strain Rate

The procedure of initiating a constant strain rate tension test is not as straightforward as it might seem at first glance. One option is to carefully ramp up the strain rate starting from a material at rest. Unfortunately, the way the strain rate is ramped up will affect the results, especially for high strain rates. On one hand, if the strain rate is ramped up too fast, the material will experience enormous stresses at the grip and the outcome will then depend on geometrical details of how the strain rate was applied to the material. On the other hand, if the strain rate is ramped up too slowly, the material will reach the yield stress long before the strain rate has reached its final value, thus affecting the stress-strain curve. It therefore seems worthwhile to see if one can start the numerical experiment already pre-set at the given strain rate, and calculate what values the other fields should take given the boundary conditions and uniform stresses.

For the numerical simulations discussed later in this dissertation, the initial configuration is approximately a uniform rectangular block of material, which means that the assumptions given in Section 4.4 are appropriate. In addition, some more assumptions are needed if the initial values of the fields in Eqs. (4.54) are to be uniquely specified. For instance, either s or Δ needs to be assigned a value. Here, $\Delta = 0$ seems reasonable, since it is vital that $\Delta^2 < \Lambda^2$ at all times; it also greatly

simplifies the equations:

$$\left. \begin{aligned} \dot{\Lambda} &= \left(\frac{1 - \Lambda}{1 + \Lambda} \right) \frac{2w^2}{\Lambda} \\ \dot{\Delta} &= w \\ \dot{s} &= \mu(1 + \nu_2)(D^{\text{tot}} - \epsilon_0 w) \end{aligned} \right\} \text{when } \Delta = 0. \quad (4.69)$$

As explained in Section 4.6, the equations are written in reduced units, which is equivalent to setting $\lambda = \tau_0 = 1$. Conveniently, $\dot{\Lambda}$ is small when Λ is close to zero or one (the largest value for $\dot{\Lambda}$ happens when $\Lambda = 1/2$). It will be assumed for the sake of calculating the initial field values that Λ is constant.

The next assumption will be that

$$\frac{1}{\epsilon_0} \dot{D}^{\text{pl}} = \dot{w} = \Lambda \dot{s} - \dot{\Delta} = 0. \quad (4.70)$$

Although the reason might not be immediately obvious, one bad side-effect of not having the correct field values during a two-dimensional numerical simulation is that the stresses will oscillate. Keeping w constant means that both s and Δ will grow at a steady rate (at least in the beginning while $\Delta = 0$), and this will ensure a non-oscillatory start. Using Eqs. (4.69) to solve (4.70) gives (at $t = 0$)

$$\left. \begin{aligned} s(0) &= \frac{D^{\text{tot}}}{\frac{1}{\mu(1+\nu_2)} + \epsilon_0 \Lambda_0} \\ \dot{s}(0) &= s(0) \\ \dot{\Delta}(0) &= \Lambda_0 s(0) \end{aligned} \right\} \text{assuming } \Delta(0) = 0 \text{ and } \dot{\Lambda}(0) \approx 0, \quad (4.71)$$

where D^{tot} and Λ_0 are given. In addition to setting the initial values for the stresses and STZ variables, it is important that the velocity gradients are set correctly. The gradients are given by

$$\frac{\partial v_x}{\partial x} = D_{xx}^{\text{tot}} \quad \text{and} \quad \frac{\partial v_y}{\partial y} = D_{yy}^{\text{tot}} \equiv D^{\text{tot}}. \quad (4.72)$$

To find $\partial_x v_x$ in terms of D^{tot} , remember that

$$D_{xx}^{\text{el}} = -\nu_2 D_{yy}^{\text{el}} \quad \text{and} \quad D_{xx}^{\text{pl}} = -D_{yy}^{\text{pl}}. \quad (4.73)$$

Combining this with the approximation $D^{\text{tot}} \approx D^{\text{el}} + D^{\text{pl}}$, or

$$D_{xx}^{\text{tot}} \approx D_{xx}^{\text{el}} + D_{xx}^{\text{pl}} \quad \text{and} \quad D_{yy}^{\text{tot}} \approx D_{yy}^{\text{el}} + D_{yy}^{\text{pl}}, \quad (4.74)$$

one can write

$$D_{xx}^{\text{tot}} + \nu_2 D^{\text{tot}} + (1 - \nu_2) D^{\text{pl}} = 0. \quad (4.75)$$

Solving for D_{xx}^{tot} at time $t = 0$, and using that $D^{\text{pl}}(0) = \epsilon_0 w(0) = \epsilon_0 \Lambda_0 s(0)$, one arrives at

$$\frac{\partial v_x(0)}{\partial x} = -\frac{\nu_2 + \Lambda_0 \epsilon_0 \mu (1 + \nu_2)}{1 + \Lambda_0 \epsilon_0 \mu (1 + \nu_2)} D^{\text{tot}}. \quad (4.76)$$

It is important to emphasize that the initial values calculated in this section are only valid when $s(0) < 1$, $\Delta(0) = 0$, and $\dot{\Lambda}(0) \approx 0$. If this is not the case, the fields (and particularly the velocities) will tend to oscillate, and could drastically change the results. When parameters are chosen so that $s(0)$ is close to unity, one should proceed with caution; a system with such parameters will be highly sensitive to how the strain rate is initiated in a real experiment.

CHAPTER 5

NUMERICAL SETUP

In order to further explore the STZ theory presented in previous chapters, a couple of two-dimensional geometrical configurations were implemented and simulated numerically. For this purpose, a C++-program using finite-difference algorithms on a regular grid with a second-order explicit time-stepping scheme to integrate the equations was written from scratch. This chapter will discuss some technical details with regards to the numerical implementation of the model, including mapping of the variables onto a unit square, finite-difference and time-stepping approximations, and boundary conditions.

5.1 Overview

The two-dimensional STZ theory was implemented numerically in order to simulate uniaxial tension experiments where material specimens were strained at constant rates. The velocity was controlled along the top and bottom edges (the “grips”), while the left and right boundaries were assumed to have no normal stresses and were allowed to deform; see Fig. 5.1.

Two sets of simulations were performed; in the first set the material was made to neck (Chapter 6), while in the second set the samples were given rough boundaries to encourage the formation of shear bands (Chapter 7). In the necking simulations, a small indentation was applied at the center of the material to break the symmetry and to encourage the neck to form in the middle. In addition, the material was assumed to be symmetric across both the x - and y -axis, so only a quarter of the system was modeled numerically.

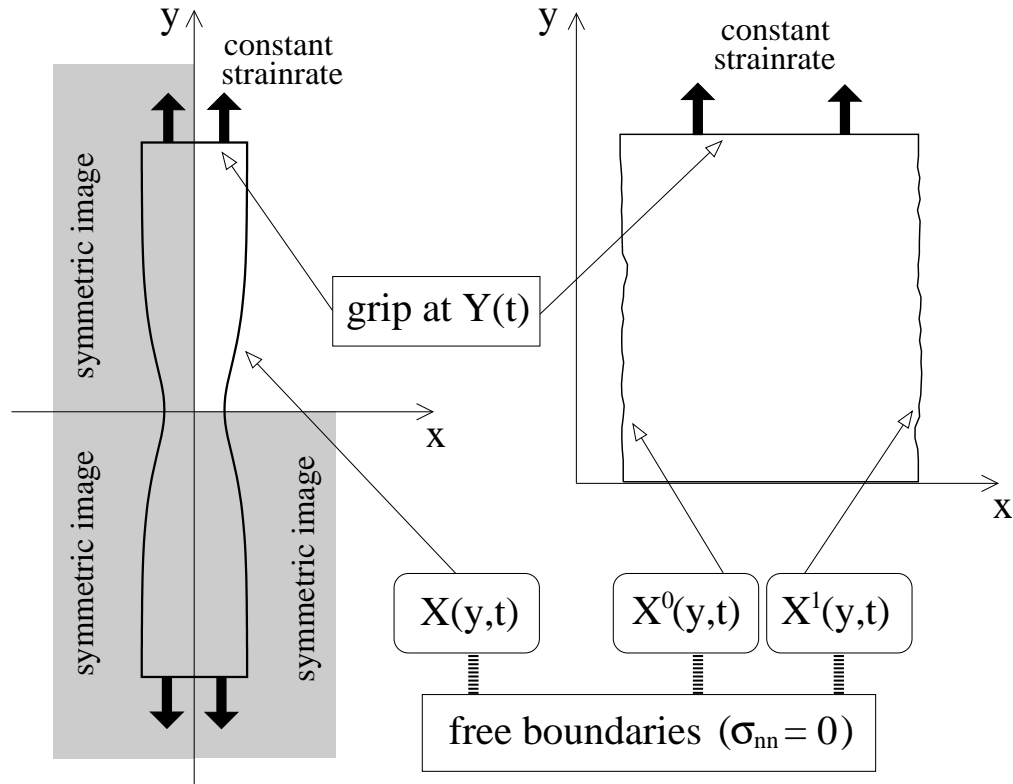


Figure 5.1: The geometrical setup of the two-dimensional simulations. A constant strain rate was applied to the rigid ends at $Y(t)$ by adjusting the velocity. The free boundaries at $X(y, t)$, $X^0(y, t)$, and $X^1(y, t)$ had no normal stresses, that is, $\sigma_{nn} = 0$. In the necking simulations on the left, the material was assumed to be symmetric across the x and y axes; thus only the upper right-hand corner of the material was actually simulated. In the simulations on the right, the lower edge was held fixed.

In the simulations with rough boundaries, the left and right edges were made stress-free and independent of each other, and no symmetry assumptions were used. The bottom of the material was held fixed while the top was subjected to a constant strain rate.

The rest of this chapter will discuss some of the details of the implementation. That includes the mapping of the coordinates onto a unit square, the discrete derivatives, the time integration, and the addition of numerical viscosity to add

stability. Finally, the implementation of the boundary conditions are discussed in detail.

5.2 Mapping the Variables onto a Unit Square

One aim when introducing the two-dimensional model was to find out how it differed from the zero-dimensional description, in particular with respect to geometrical inhomogeneities. After deciding to investigate constant strain rate simulations, it seemed sufficient to only allow the sides to deform, while keeping the grips straight. It was assumed that the free boundaries could be described by functions that were single valued: $X(y, t)$ for the necking simulations, or $X^0(y, t)$ and $X^1(y, t)$ in the case of the model without symmetry assumptions. The position of the grips was described by a function only dependent on time, $Y(t)$. With these assumptions, the material was easily mapped onto a unit square with coordinates $\zeta_x \in [0, 1]$ and $\zeta_y \in [0, 1]$. For the necking simulations with the axis symmetries, the mapping was

$$\zeta_x = \frac{x}{X(y, t)}, \quad \zeta_y = \frac{y}{Y(t)}, \quad (5.1)$$

while the simulations with the free boundaries needed the slightly more general transformation

$$\zeta_x \equiv \frac{x - X^0(y, t)}{X^1(y, t) - X^0(y, t)}, \quad \zeta_y \equiv \frac{y}{Y(t)}. \quad (5.2)$$

See Fig. 5.2 for an illustration. The first-order derivatives would then take the

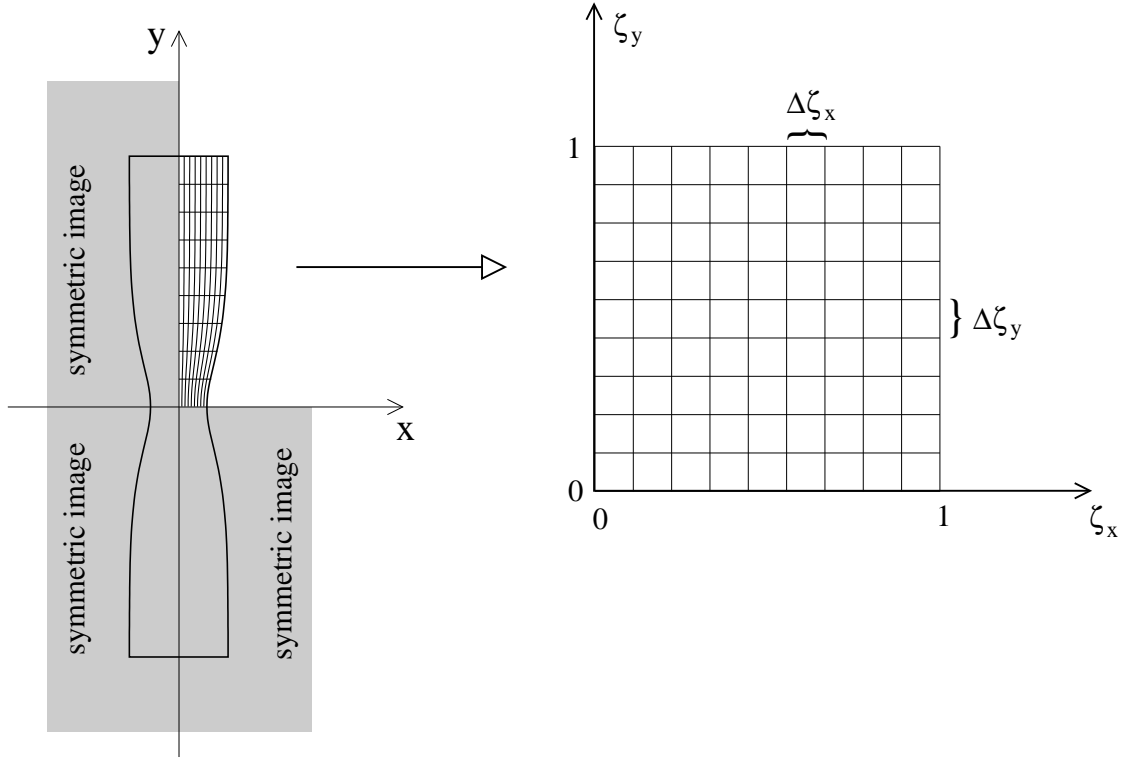


Figure 5.2: For the necking simulations, the deformed area $x \in [0, X(y, t)]$, $y \in [0, Y(t)]$ was mapped onto the unit square $\zeta_x \in [0, 1]$, $\zeta_y \in [0, 1]$. Similarly, the non-symmetric simulations (not shown here) mapped the area $x \in [X^0(y, t), X^1(y, t)]$, $y \in [0, Y(t)]$ onto the same unit square.

form¹

$$\frac{\partial}{\partial x} = \frac{1}{(\mathcal{X}^1 - \mathcal{X}^0)} \frac{\partial}{\partial \zeta_x}, \quad (5.3a)$$

$$\frac{\partial}{\partial y} = \frac{1}{Y} \left(\frac{\partial}{\partial \zeta_y} - \omega_{xy} \frac{\partial}{\partial \zeta_x} \right), \quad (5.3b)$$

where

$$\omega_{xy} = \frac{1}{(\mathcal{X}^1 - \mathcal{X}^0)} \left[\zeta_x \frac{\partial \mathcal{X}^1}{\partial \zeta_y} + (1 - \zeta_x) \frac{\partial \mathcal{X}^0}{\partial \zeta_y} \right]. \quad (5.3c)$$

¹The derivation of the temporal and spatial derivatives in the new coordinates, as well as the transformed equations of motion, can be found in Appendix B.

In the equations for the derivatives, the deforming boundaries needed to be written as functions of ζ_y rather than y , so $\mathcal{X}^0 \equiv \mathcal{X}^0(\zeta_y, t)$ and $\mathcal{X}^1 \equiv \mathcal{X}^1(\zeta_y, t)$ were used instead of $X^0(y, t)$ and $X^1(y, t)$, respectively. For the necking simulations, the expressions can be simplified by setting $\mathcal{X}^1 \rightarrow \mathcal{X}$ and $\mathcal{X}^0 \rightarrow 0$.

The advantage of mapping the coordinates using Eqs. (5.1) and (5.2) was that the calculations could be done on a regular grid where the values of the fields were discretized into equally spaced nodes. The disadvantage was that the operators, like the first-order derivatives shown above, became more complicated.

Rather than tracking the boundaries by mapping the coordinate system onto a unit square, the phase-field [73] and level-set [74, 75] methods were briefly considered, although this approach would have been much more expensive computationally. At least in the initial stages of the simulations, the geometry was simple enough that the most compelling choice was to track the boundary by mapping the material onto the unit square so that the boundary $X(y, t)$ of the sample became single valued and coincided with the boundary of the grid. In the later stages in some of the cases presented in Chapters 6 and 7, the simulations showed signs of shear banding that induced sharp inhomogeneous flows; these results should be interpreted with the restricted geometry in mind, and it might be interesting in future numerical investigations to loosen those restrictions (perhaps by using the aforementioned methods) when exploring the dynamics both in the limit of extreme deformations and in more complicated geometries.

5.3 Discretized Gradients

The simulations were carried out on a uniform rectangular grid using finite-difference approximations for the spatial derivatives and an explicit time stepping

scheme. The continuous fields were discretized onto a grid with N_x nodes in the x -direction and N_y nodes in the y -direction. In terms of the transformed coordinates (5.1) and (5.2), the distance between the nodes were $\Delta\zeta_x = 1/(N_x - 1)$ and $\Delta\zeta_y = 1/(N_y - 1)$; see Fig. 5.2.

Since the fields were discretized, approximations involving the grid points were needed to calculate the necessary gradients required by the equations of motion. The values of the expressions $\partial/\partial\zeta_x$ and $\partial/\partial\zeta_y$ in Eqs. (5.3) (the grid derivatives) at any grid point in the bulk were approximated by calculating the slope between the nodes on either side of that grid point:

$$\left. \frac{\partial u}{\partial \zeta} \right|_{\zeta=i\Delta\zeta} \rightarrow \frac{u_{i+1} - u_{i-1}}{2\Delta\zeta} \quad (\text{bulk}), \quad (5.4a)$$

where ζ was either ζ_x or ζ_y . This is the central difference approximation, and it is accurate to second order.

Special care was needed at the boundaries. There were two types, the ones that were at the edge of the material and the ones that bordered to a symmetric image (the latter only applied to the necking calculations). For the former type, the grid-derivatives were estimated through extrapolation as

$$\left. \frac{\partial u}{\partial \zeta} \right|_{\zeta=i\Delta\zeta} \rightarrow \frac{3u_i - 4u_{i-1} + u_{i-2}}{2\Delta\zeta} \quad (\text{edge}). \quad (5.4b)$$

The fields were assumed to be symmetric or anti-symmetric across the symmetry-axes, and the discretized equations for the bulk could still be applied to the latter type. The boundary conditions will be discussed further in Section 5.6.

5.4 Time Stepping

The fields were integrated forward in time using the mid-point method, also known as the second-order Runge-Kutta scheme [76]. It is an explicit integration algo-

rithm which is second-order accurate in time. The details of the implementation are given below.

Start by writing the (analytic) equations of motion for the fields as

$$\frac{\partial \mathbf{u}}{\partial t} = f[\mathbf{u}], \quad (5.5)$$

where $\mathbf{u} = \{u_1, u_2, \dots, u_m\}$ contains all the m fields of the model (in Chapters 6 and 7 the fields were: the pressure p , the stresses s and τ , the components of the velocity v_x and v_y , and the STZ variables Δ_s , Δ_τ , and Λ). Given the fields \mathbf{u}^n at time $t = n\Delta t$, the values \mathbf{u}^{n+1} at time $t = t + \Delta t = (n + 1)\Delta t$ were calculated as follows:

$$\tilde{\mathbf{u}}^{n+1} = \mathbf{u}^n + f[\mathbf{u}^n]\Delta t, \quad (5.6a)$$

$$\mathbf{u}^{n+1} = \mathbf{u}^n + \frac{1}{2}(f[\mathbf{u}^n] + f[\tilde{\mathbf{u}}^{n+1}])\Delta t. \quad (5.6b)$$

The simulations used an adaptive time-step technique called *step-doubling*. The details are described in Section 16.2 of Numerical Recipes [76]. The general idea, illustrated in Fig. 5.3, is that first, the system $\mathbf{u}_{\text{original}}^n$ is integrated forward twice using a time-step of Δt , giving $\mathbf{u}_{\text{twice}}^{n+2}$. From the original values $\mathbf{u}_{\text{original}}^n$, the system is again integrated forward in time, only now the time-step is $2\Delta t$, yielding $\mathbf{u}_{\text{once}}^{n+2}$. The difference $|\mathbf{u}_{\text{once}}^{n+2} - \mathbf{u}_{\text{twice}}^{n+2}|$ is then used to monitor the accuracy; if the error is low enough, the results $\mathbf{u}_{\text{twice}}^{n+2}$ are accepted, otherwise they have to be recalculated from $\mathbf{u}_{\text{original}}^n$ using a smaller time-step.

5.5 Numerical Viscosity and Stability

As explained in Section 5.3, all the spatial first-order derivatives were approximated by a central-difference formula. Since the equations of motion (4.52) had no higher-order spatial derivatives, the grid points had a tendency to become “decoupled”

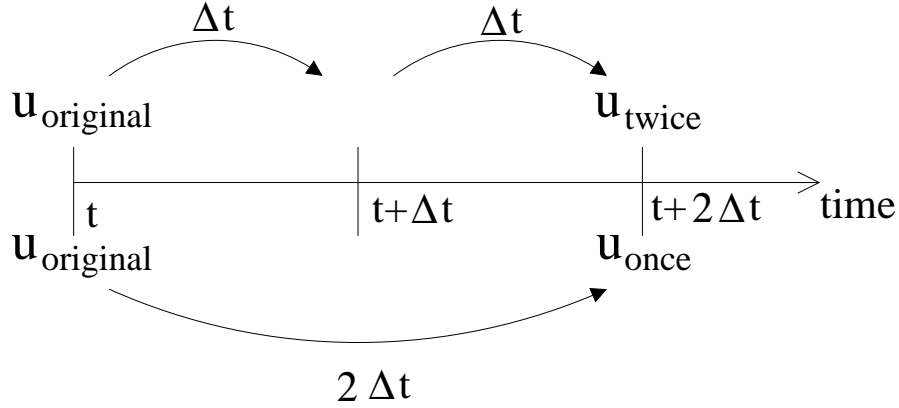


Figure 5.3: The step-doubling technique was used to control the accuracy of the simulations. The fields were integrated twice, first in two steps using a time-step of Δt (u_{twice}), then in one step using a time-step of $2\Delta t$ (u_{once}). The time-step was then adjusted according to the difference in the results.

into two sets of nodes like the black and white squares on a chess board. The easiest way to remedy this was to add a small amount of numerical viscosity. If the original equations of motion were given by Eq. (5.5), then viscosity could be included by adding a diffusion term

$$\frac{\partial \mathbf{u}}{\partial t} = f[\mathbf{u}] + \eta \nabla^2 \mathbf{u}, \quad (5.7)$$

where η is the strength of the numerical viscosity. Some care was needed to make sure that the new term behaved properly. The three issues that will be discussed below are implementation, stability, and how it affected the physical results.

Two questions that arose during implementation were, firstly, whether to include the diffusion for all the fields or just some, and secondly, whether or not it should be written in transformed coordinates (that is, mapped onto the unit square). After extensive investigation, it was found that the most effective approach was to add the viscosity to the velocities only; they were usually the first fields to go unstable, and as long as they were under control, the simulations did

fine. It is also worth noting that it was usually the velocities, through the adaptive time-step algorithm described in Section 5.4, that limited the size of the time-steps.

With regards to the transformed coordinates, the purpose of the damping term was to “re-couple” those black and white squares on the chess board mentioned above. This was best done by implementing the diffusion term as

$$\left. \frac{\partial^2 u}{\partial t^2} \right|_{\zeta=i\Delta\zeta} \rightarrow \eta \left(\frac{u_{i+1,j} - 2u_{i,j} + u_{i-1,j}}{\Delta\zeta_x^2} + \frac{u_{i,j+1} - 2u_{i,j} + u_{i,j-1}}{\Delta\zeta_y^2} \right) \text{ (bulk)}. \quad (5.8a)$$

Mapping the Laplacian onto the unit square would turn it into a relatively complicated expression with many terms containing mixed derivatives of both first and second order. The diffusion term was intended as a numerical tool, so it was best to keep it simple with respect to the grid. The downside to not transforming the Laplacian was that its physical meaning became muddled. If the Laplacian were to be transformed, it would be a genuine viscosity term (when added to the equations of motion for the velocities).

On the boundaries (apart from the ones separating the symmetric images), the second derivative was set to zero:

$$\left. \frac{\partial^2 u}{\partial t^2} \right|_{\zeta=i\Delta\zeta} \rightarrow 0 \quad \text{(edge)}. \quad (5.8b)$$

Trying to calculate the second derivative by extrapolation at the edge, as was done for the first-order derivative, would lead to decreased numerical stability, making the behavior of the damping term contradictory to its purpose.

The purpose of the viscosity term was, as mentioned earlier, to make the numerical scheme more stable by creating a greater coupling between the grid points. However, when using explicit time-stepping schemes like the mid-point method, the Laplacian could have the opposite effect if the time-step was made too large. Section A.2.4 shows that the upper limit for the time-step in order to guarantee

stability for all wavelengths is given by

$$\Delta t < \frac{1}{2\eta} \frac{1}{\frac{1}{\Delta\zeta_x^2} + \frac{1}{\Delta\zeta_y^2}}. \quad (5.9)$$

Since the added viscosity was only meant as a numerical tool, it was important to monitor any changes it made to the physical results. The influence of the viscosity was minimized by performing successive runs with smaller and smaller values of η . If the numerical viscosity was chosen too high, the results would look nice and smooth, but when compared to simulations with lower values of η it became clear that the added viscosity was smearing out sharp features such as shear bands. On the other hand, when too small values of η were used, large gradients caused by the “de-coupling” would make the simulations more unstable. This was particularly pronounced at the border (where values were calculated through extrapolation) and in larger grids.

The simulations were most sensitive to the value of η at low strain rates, basically because there was more time (per strain) to dampen out the velocities. When running as slow as $D^{\text{tot}} = 10^{-5}$ on the larger (more unstable) grids used in Chapter 7, there were no values of η that gave satisfactory results. Even for the smaller grids in the necking simulations of Chapter 6, the slowest strain rate $D^{\text{tot}} = 10^{-5}$ was hard to accommodate. In the end, it was found that $\eta = 0.02$ (which in fact turned out to be a good choice for all the simulations) enabled the slowest simulation to reach 5% strain while having only a small impact on the physical results. The influence due to the exact choice of η for higher strain rates was usually imperceptible.

Table 5.1: This table shows what symmetry conditions were imposed on the fields in the necking calculations across the boundaries between the symmetric images in Fig. 5.2. The fields were: the pressure p , the stress-tensor components s and τ and corresponding STZ variables Δ_s and Δ_τ , the relative density of STZs Λ , and the velocity components v_x and v_y .

	symmetric	anti-symmetric
boundary parallel to x-axis	$p, s, \Delta_s, \Lambda, v_x$	τ, Δ_τ, v_y
boundary parallel to y-axis	$p, s, \Delta_s, \Lambda, v_y$	τ, Δ_τ, v_x

5.6 Boundary Conditions

In the bulk, the dynamics of the material was calculated from Eqs. (4.52) (with the numerical viscosity (5.7) added) and mapped onto the coordinates ζ_x and ζ_y using Eqs. (5.1) or (5.2), and then discretized using Eqs. (5.4a) and (5.8a).

On the boundary of the grid on which the material was simulated, special care was needed. Some of the fields had their node values at the edge set explicitly, while others had these values determined by extrapolating the values calculated for the bulk or using symmetry conditions.

In the necking simulations, special symmetry conditions were applied to the boundaries between the grid and its symmetric images (the x -axis and y -axis in Fig. 5.2). At these boundaries, each field was either considered symmetric or anti-symmetric; Table 5.1 shows which fields fell into which category across each of the two applicable boundaries. A symmetric boundary condition $u_{-i} = u_i$ simply meant that the gradient across this boundary had to be zero, and that the values of the nodes were mirrored on the other side. An anti-symmetric condition $u_{-i} = -u_i$ meant that the value on the boundary was zero and that values on opposite sides

had opposite signs.

At all the outer boundaries, most of the values were calculated by extrapolating from the bulk using Eqs. (5.4b) and (5.8b), although some were set explicitly; the rest of this section will describe how this was implemented.

All the simulations were done at constant strain rate. This was enforced by controlling the y -component of the velocity, v_y , at the grips (the top and bottom boundaries in Fig. 5.1). For example, in the necking simulations the grip velocity was given by

$$v_y[x, y = \pm Y(t), t] = \pm Y(t) D^{\text{tot}}, \quad (5.10)$$

where D^{tot} was the constant strain rate. Since the velocity was applied to all the nodes along the top and bottom, these edges remained straight. The position of the edge as a function of time, using that $v_y[x, y = Y(t), t] = \partial_t Y(t)$, was therefore

$$Y(t) = Y(0) \exp(t D^{\text{tot}}). \quad (5.11)$$

In addition to controlling v_y , the variables τ and Δ_τ were kept at zero along the grips.

At the free boundaries, which comprised $X(y, t)$ in the necking simulations and $X^0(y, t)$ and $X^1(y, t)$ in the others, the normal stress σ_{nn} and shear stress σ_{nt} were set to zero, while the tangential stress σ_{tt} was left untouched. Since these boundaries could deform, the stresses had to be written in a locally rotated frame of reference at each node. θ was defined as the angle through which $X(y, t)$ was rotated in the counter-clockwise direction, where $\theta = 0$ meant that the boundary was parallel to the y -axis; see Fig. 5.4. Using $X_y \equiv \partial_y X(y, t)$, the free boundary

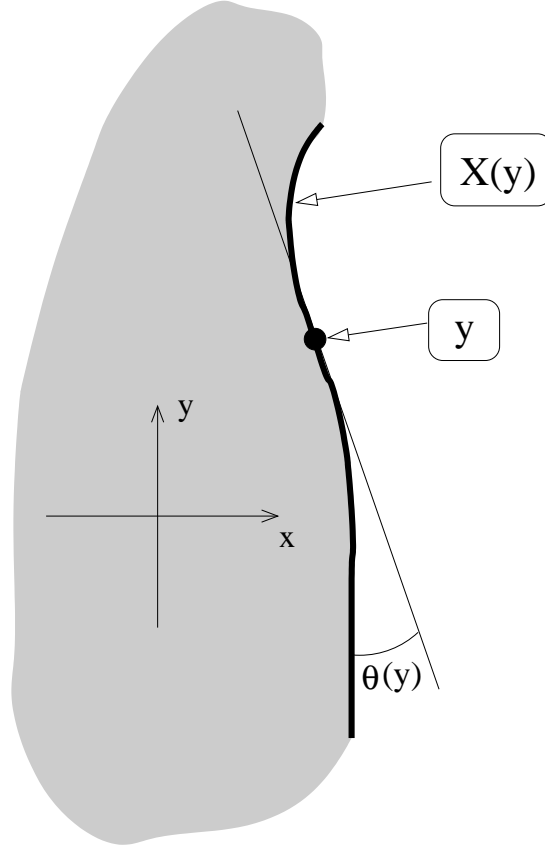


Figure 5.4: θ was defined as the angle through which $X(y, t)$ was rotated in the counter-clockwise direction.

and θ were related by

$$\begin{aligned}
 \tan \theta &= -X_y, & \tan 2\theta &= \frac{-2X_y}{1 - X_y^2}, \\
 \sin \theta &= \frac{-X_y}{\sqrt{1 + X_y^2}}, & \sin 2\theta &= \frac{-2X_y}{1 + X_y^2}, \\
 \cos \theta &= \frac{1}{\sqrt{1 + X_y^2}}, & \cos 2\theta &= \frac{1 - X_y^2}{1 + X_y^2}.
 \end{aligned} \tag{5.12}$$

Using Eq. (2.11b), the free-boundary conditions can be written as

$$\sigma_{nn} = \sigma'_{xx} = -p - s \cos 2\theta + \tau \sin 2\theta = 0 \quad (\text{no normal stress}), \tag{5.13a}$$

$$\sigma_{nt} = \sigma'_{xy} = \tau \cos 2\theta + s \sin 2\theta = 0 \quad (\text{no shear stress}), \tag{5.13b}$$

$$\sigma_{tt} = \sigma'_{yy} = -p + s \cos 2\theta - \tau \sin 2\theta = \tilde{\sigma}_{tt} \quad (\text{unaltered tang. stress}), \tag{5.13c}$$

where the indices n and t stand for the normal and tangential components of the stress and $\tilde{\sigma}_{tt}$ was the original value of the tangential stress.

Since the simulations had the stresses written in terms of p , s , and τ , the boundary conditions (5.13) had to be applied to those fields. Their new values were found by solving Eqs. (5.13), giving

$$p = -\frac{1}{2}\tilde{\sigma}_{tt}, \quad (5.14a)$$

$$s = \frac{1}{2}\tilde{\sigma}_{tt} \cos 2\theta, \quad (5.14b)$$

$$\tau = -\frac{1}{2}\tilde{\sigma}_{tt} \sin 2\theta. \quad (5.14c)$$

Surface tension could be added at the boundary by using $\sigma_{nn} = \gamma\kappa$. This was done for some earlier simulations that are not discussed in this dissertation. The positive constant γ determines the amount of surface tension, and

$$\kappa = \frac{\partial_y^2 X}{[1 + X_y^2]^{3/2}} \quad (5.15)$$

is the curvature of the boundary. The latter is positive if the boundary is concave (necking), and negative if it is convex (bulging). When surface tension is included, the new values for p , s , and τ would be

$$p = -\frac{1}{2}(\tilde{\sigma}_{tt} + \gamma\kappa), \quad (5.16a)$$

$$s = \frac{1}{2}(\tilde{\sigma}_{tt} - \gamma\kappa) \cos 2\theta, \quad (5.16b)$$

$$\tau = -\frac{1}{2}(\tilde{\sigma}_{tt} - \gamma\kappa) \sin 2\theta. \quad (5.16c)$$

The boundaries $X(y, t)$, $X^0(y, t)$, and $X^1(y, t)$ also had some of their values set explicitly. Since stresses were large in the corners of the samples, forcing the boundaries to be flat there improved stability dramatically. This was done by setting the values of the two nodes closest to the grips in each corner.

5.7 Change of Area in a Uniform Two-Dimensional Solid

One of the approximations in the two-dimensional tensorial STZ model was that the material density ρ remained constant, or equivalently, that the material was incompressible. While this was true by construction for the plastic deformation, the trace of the elastic strain tensor did not vanish. It was possible to find the parameter ranges for which the system was approximately incompressible by measuring the change in density while varying the parameter values. Note that this problem is not present in the zero-dimensional theory, since this description has no inertia nor elastic deformation.

For a given stress, the strain in an elastic material is given by Eqs. (4.55), where $\varepsilon_{xx} = \ln(L_x/L_{x0})$ and $\varepsilon_{yy} = \ln(L_y/L_{y0})$. For a two-dimensional, rectangular piece of elastic material, the area A is given by

$$\begin{aligned} A &= L_x L_y \\ &= L_{x0} L_{y0} \exp(\varepsilon_{xx} + \varepsilon_{yy}) \\ &= A_0 \exp\left(\frac{s}{\mu} \frac{1 - \nu_2}{1 + \nu_2}\right). \end{aligned} \quad (5.17)$$

Defining the change in area as $\Delta A \equiv |A - A_0|$, one can write

$$\frac{\Delta A}{A_0} = \left| \exp\left(\frac{s}{\mu} \frac{1 - \nu_2}{1 + \nu_2}\right) - 1 \right|. \quad (5.18)$$

Eq. (5.18) is plotted in Fig. 5.5 for certain values of s , the positive and negative stresses representing tensile and compressive loads, respectively. According to Eq. (5.18), choosing $\mu = 100$ with $\nu_2 = 0.5$ would give $\Delta A/A_0 \approx 0.3\%$ when $s = 1$ (the ‘‘yield stress’’), and $\Delta A/A_0 \approx 3\%$ when $s = 10$. For $\mu = 10$, the relative change in area is becoming uncomfortably high even at $s = 1$, where $\Delta A/A_0 \approx 3\%$. Conversely, insisting that $\Delta A/A_0 < 1\%$ requires that $\mu > 34$ at $s = 1$ and $\mu > 67$

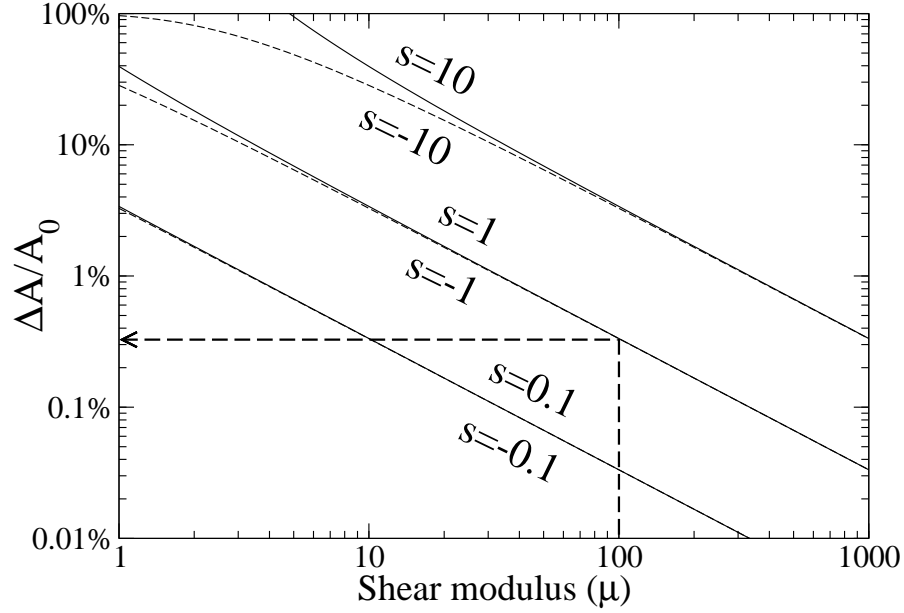


Figure 5.5: The shear modulus μ plotted against the relative change of area $\Delta A/A_0$ due to elastic deformation for a few selected values of the stress s . The Poisson ratio was $\nu_2 = 0.5$. With $\mu = 100$ and $s = 1$ (the “yield stress”), the elastic deformation would increase the area by about 0.3%. As the stress increases, the area changes further.

at $s = 2$. More generally,

$$\frac{\Delta A}{A_0} < r \quad \text{requires} \quad \mu > \begin{cases} \left(\frac{1-\nu_2}{1+\nu_2} \right) \frac{s}{\ln(1+r)} & \text{for } s > 0, r > 0 \\ \left(\frac{1-\nu_2}{1+\nu_2} \right) \frac{s}{\ln(1-r)} & \text{for } s < 0, r \in \langle 0, 1 \rangle. \end{cases} \quad (5.19)$$

As will be shown later, the stresses in the simulations discussed in this dissertation, which used $\mu = 100$, seldom exceeded $s = 3$, or even $s = 2$ (the exception was stresses at grid points where the material had grown extremely thin and was “breaking”; these results were questionable also for geometrical reasons, and were disregarded). This means that the relative change in area due to elastic deformations stayed below 1%.

To verify that these results held in the numerical model, a range of small

simulations were run. The concern was that other approximations such as the numerical viscosity or the discreteness of the grid might influence the change in area as well. These small simulations were run on a 5 by 5 grid, where the edges were straight and the strain rate constant. The physical size of the systems varied around the size of the simulations described later in this chapter ($A_0 \in [1, 16]$). The parameters were varied in the following ranges: $\mu \in [10, 1000]$, $\epsilon_0 \in [0.3, 0.003]$, $\Lambda_0 \in [0.01, 1]$, and $D^{\text{tot}} \in [10^{-2}, 10^{-5}]$.

In all the stable simulations, the elastic strain accounted for nearly all the change in density, as described above. More specifically, the actual change in area was always slightly lower than that estimated due to elastic deformations, the difference never exceeding 0.5% of the total change in area. For small values of ϵ_0 , the higher strain rates were the most inaccurate in this respect. For higher values of ϵ_0 , when the stresses would be less responsible for storing the energy, a change in strain rate would have little, if any, effect on the change in area. In general, lowering μ or Λ_0 would also cause a greater difference between the expected change in area due to the stress, and the actual.

For example, with $\mu = 100$, $\Lambda_0 = 1$, $\epsilon_0 = 0.1$, and $D^{\text{tot}} = 0.001$, the stress leveled off at $s_\infty = 1.005$, which should have given a relative change in area of 0.336%. The measured relative change in area was actually 0.333%. In other words, the change of density in the simulations closely followed the theoretical predictions above, and when there were any discrepancies, the area in the simulated model would remain somewhat closer to the initial value. Thus it should be safe to use Eq. (5.18) as an upper bound estimate of the change in density, $\Delta A/A_0$. Since only results with $s < 3$ were used, setting the shear modulus to $\mu = 100$ was a reasonable choice.

CHAPTER 6

NECKING

Irregular geometry in a two-dimensional sample of material can cause stress localization and shear banding. As compared to the zero-dimensional model, the introduction of two spatial dimensions also adds elastic deformation and inertia. As long as the elastic strains are small, the speed of sound high, and the rate of total deformation low, the difference between a zero-dimensional and a uniform two-dimensional system is minimal. In a spatially extended system, geometry can play a role in determining the behavior of the material through phenomena such as stress localization and shear banding.

Generally speaking, metallic glasses have two modes of deformation: homogeneous and inhomogeneous (see Section 4.2 and also [77]). The simulations described in this and the next chapter illustrate how a system transitions from the former to the latter. Some earlier work can be found in [71].

6.1 Simulations

One way of exploring the effect of a non-trivial geometry is to look at the dynamics of a material while it is necking. A series of simulations were run where a rectangular 2×8 piece of material was elongated in the y -direction at a constant strain rate. The material was slightly indented in the middle, where the width was reduced by 1%. Specifically, the right-hand boundary was given by $X(y, t = 0) = 1 - \delta(y)$, where $\delta(y) = 0.01 \exp[-\ln 2(y/0.1)^2]$. This perturbation to the geometry was added to break the symmetry and to help trigger any potential instabilities. The material (or rather, a quarter of it) was mapped onto an 11×41 regular grid, using the transformation of variables described in Section 5.2. The size of the grid

was verified to be large enough to support the desired accuracy, as a comparison with some test runs on a larger 21×81 grid gave almost identical results. The shear modulus was set to $\mu = 100$, while the numerical viscosity was chosen to be $\eta = 0.02$, based on the discussions in Sections 5.5 and 5.7, respectively.

Fig. 6.1 shows the outlines of material samples in two separate simulations. The solid outlines were the initial configurations; notice that the indentations are hardly visible. The dashed outlines represent the configurations after the systems had been strained. The simulation on the left was strained an order of magnitude faster than the one on the right. While the former had a smooth neck, the latter had a more irregular boundary due to shear bands.

In general, shear bands would appear more readily when the material was strained at a lower rate. The left part of Fig. 6.2 shows the plastic dissipation Q as given by Eq. (4.60) in a simulation with $D^{\text{tot}} = 10^{-4}$, $\epsilon_0 = 0.03$, and $\Lambda_0 = 1$ after it had strained roughly 6%. The right-hand side displays, for the same simulation, the velocity field with the uniform part $\mathbf{v}_{\text{uniform}} = (0, yD^{\text{tot}})$ subtracted away. These figures show that the material no longer was deforming uniformly. Stress concentrations radiating out from each notch at roughly 45° increased the plastic dissipation, and thus the plastic deformation, along these shear bands. As can be seen in the velocity plot, the whole central piece of the neck became narrower, and this is what caused the irregular boundaries seen on the right-hand side of Fig. 6.1.

Chapter 3 explained how the rate of deformation D^{pl} increases drastically when the deviatoric stress $|s|$ becomes larger than unity. In steady state, any area with $|s| > 1$ can be considered to be flowing plastically, while regions with $|s| < 1$ are jammed. This applies to the tensorial version of the theory, too, when measuring the deviatoric stress by the invariant $\bar{s} = \sqrt{s^2 + \tau^2}$, also known as the maximum

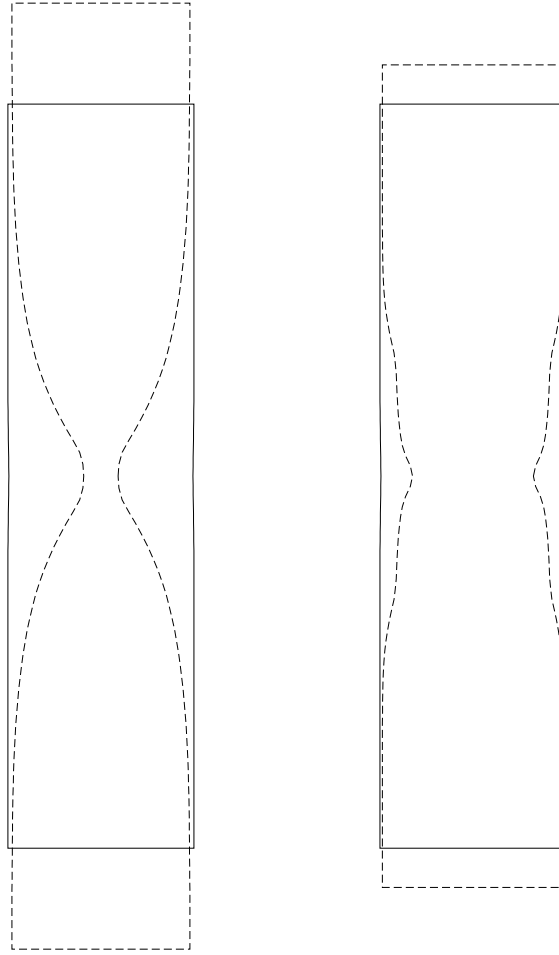


Figure 6.1: Examples of the geometry in two numerical experiments. The solid outlines are the initial configurations — the initial indentations are hardly visible. The dashed outlines represent the geometry after the left and right samples were strained 24% and 10%, respectively. The strain rate in the left simulation was $D^{\text{tot}} = 10^{-3}$, ten times higher than on the right. In both simulations $\mu = 100$, $\nu_2 = 0.5$, $\epsilon_0 = 0.03$, $\Lambda_0 = 1$, and the initial size of the samples were 2×8 .

shear stress. Fig. 6.3 shows a series of snapshots from a necking simulation where the interior has been shaded according to the values of \bar{s} ; the darker the shade, the higher the value. At low strains the stress was uniform, but as the material

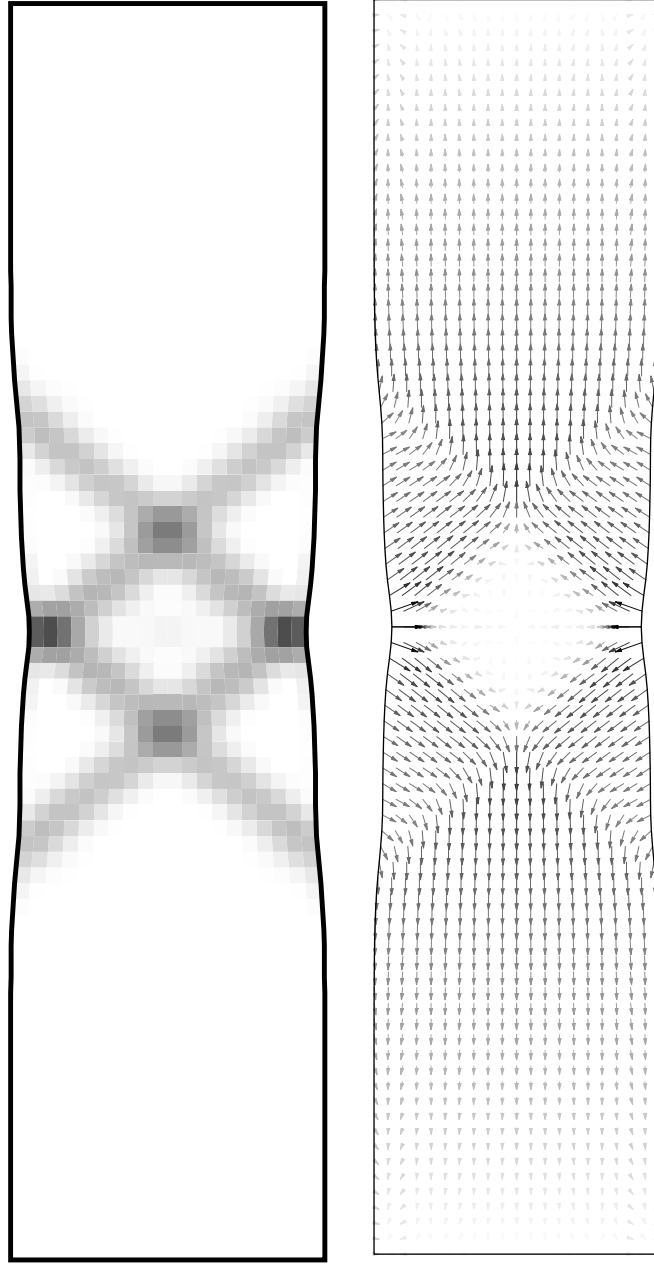


Figure 6.2: The plots in this figure are taken from the same simulation as the outline on the right-hand side of Fig. 6.1, but this time at roughly 6% strain. The density plot on the left shows the plastic dissipation Q as given by Eq. (4.60). The figure on the right displays the velocity field after the uniform part $\mathbf{v}_{\text{uniform}} = (0, yD^{\text{tot}})$ had been subtracted away. The parameters for this simulation were $D^{\text{tot}} = 10^{-4}$, $\epsilon_0 = 0.03$, and $\Lambda_0 = 1$.

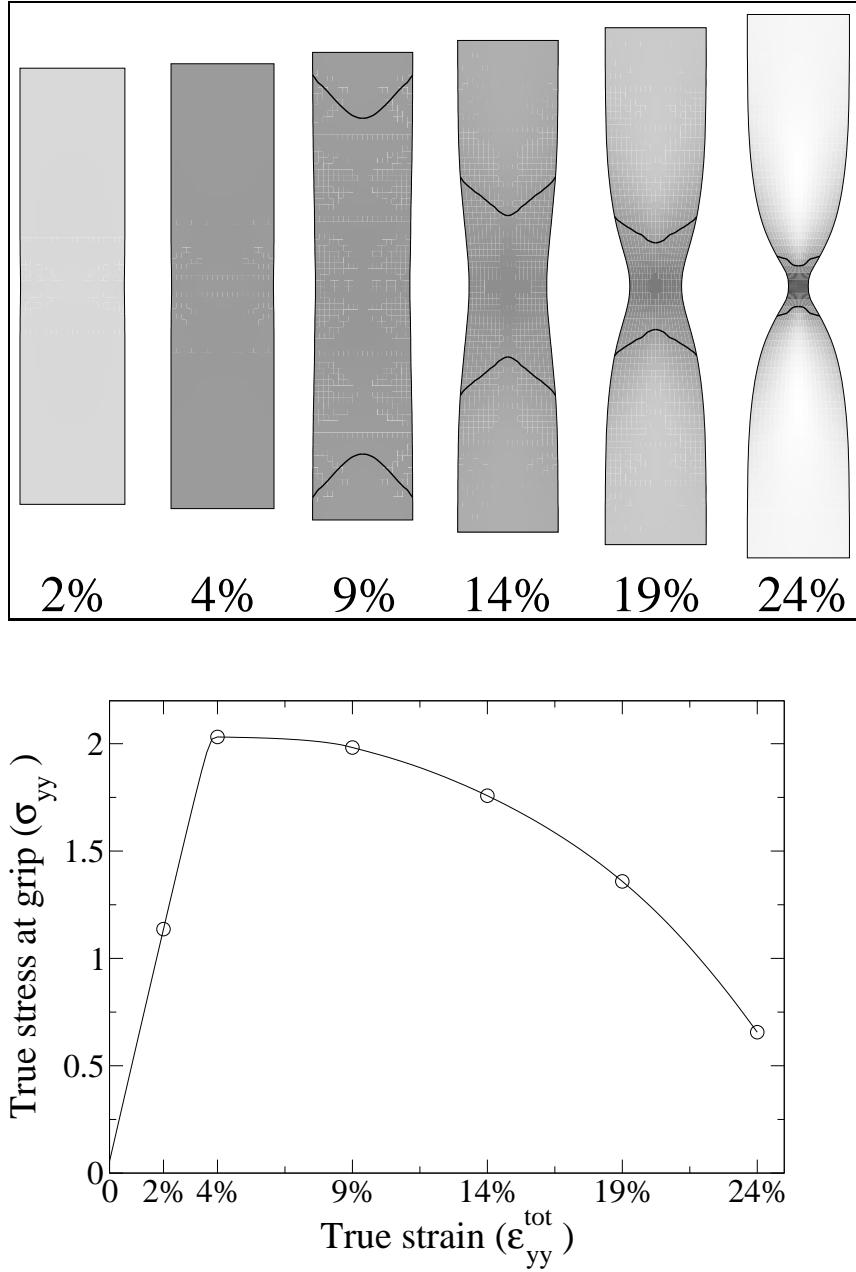


Figure 6.3: The graph shows the true stress σ_{yy} at the grips as a function of the total strain $\epsilon_{yy}^{\text{tot}}$. Snapshots of the system were taken at six different strains, and the interior was shaded according to the value of the maximum shear stress $\bar{s} = \sqrt{s^2 + \tau^2}$. The black lines in the four last snapshots show where $\bar{s} = 1$, suggesting that the area between the lines ($\bar{s} > 1$) is flowing plastically while the areas at the ends ($\bar{s} < 1$) are jammed. The parameter values were $D^{\text{tot}} = 10^{-3}$, $\epsilon_0 = 0.03$, and $\Lambda_0 = 1$.

necked the stress concentrated in the center. The black lines that appear in the last four snapshots mark the boundary between $\bar{s} < 1$ and $\bar{s} > 1$. The steady-state solutions suggest that the area between the lines were flowing plastically, while the regions on either end, outside the lines, were more or less jammed. As the neck grew more pronounced, the plastically flowing area would shrink, making a smaller and smaller area responsible for accommodating the ever increasing global strain. In addition, the jammed areas would relax (notice how the ends grew lighter in the final snapshots) and contract along the strained y -axis while releasing stored energy. This decrease in strain at the ends had to be compensated by increasing the strain even further in the middle.

The graph below the snapshots plots the true stress σ_{yy} at the grips as a function of the total true strain $\varepsilon_{yy}^{\text{tot}}$. The true stress (at the grip) is defined as the force divided by the current width of the material, both measured at the grip. The true, or logarithmic, total strain is defined as $\varepsilon_{yy}^{\text{tot}} = \ln[L_y(t)/L_y(0)]$, where $L_y(t)$ is the length of the material at time t . The snapshots were marked on the graph as circles. The first snapshot was taken while the material was in the “elastic phase”, while the second was taken just as the material was about to yield. This explains why the two first snapshots seem so uniform. Note that since the plotted stress was measured at the grips, it corresponds to the shading at the ends of the material.

To illustrate how the parameters affect the material behavior, Figs. 6.4, 6.5, and 6.6 show further plots where the true stress σ_{yy} at the grip was plotted against the true total strain $\varepsilon_{yy}^{\text{tot}}$, comparing curves for various values of ϵ_0 and D^{tot} . In Fig. 6.4 all the simulations were strained at a rate of $D^{\text{tot}} = 10^{-3}$ while ϵ_0 , the amount of strain caused by flipping STZs, was varied. In simulations with a higher ϵ_0 , the material needed to be strained further before reaching the yield stress. This

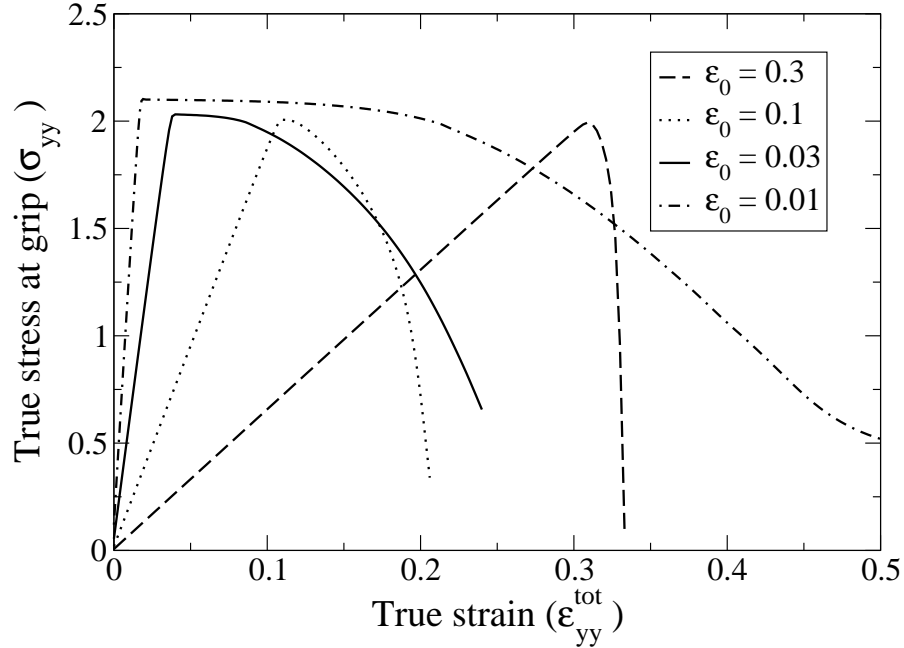


Figure 6.4: The true stress σ_{yy} at the grip plotted against the true total strain $\varepsilon_{yy}^{\text{tot}}$ for selected values of ε_0 . Values of other parameters were $D^{\text{tot}} = 10^{-3}$, $\mu = 100$, $\nu_2 = 0.5$, and $\Lambda \equiv 1$. As ε_0 was increased, it took longer (in terms of the strain) for the material to reach the yield stress, since less of the deformation was stored as elastic energy (and more as plastic). Once the yield stress was reached, a higher value of ε_0 allowed for more plastic deformation and thus a quicker relaxation of the stress.

is because more of the work done on the system was stored as plastic energy; it was only the elastic deformations that contributed to the rising stress. After reaching the yield stress, the systems with a higher ε_0 would see a faster relaxation of the stress. This is probably because a high ε_0 allowed for a higher plastic rate of deformation at the neck, where the elastic stored energy was released through plastic dissipation. Interestingly enough, a high ε_0 meant that most of the stored energy was plastic; that is, the energy was stored in flipped STZs rather than elastic strain (the amount of stored plastic energy cannot easily be deduced from the stress-strain curves).

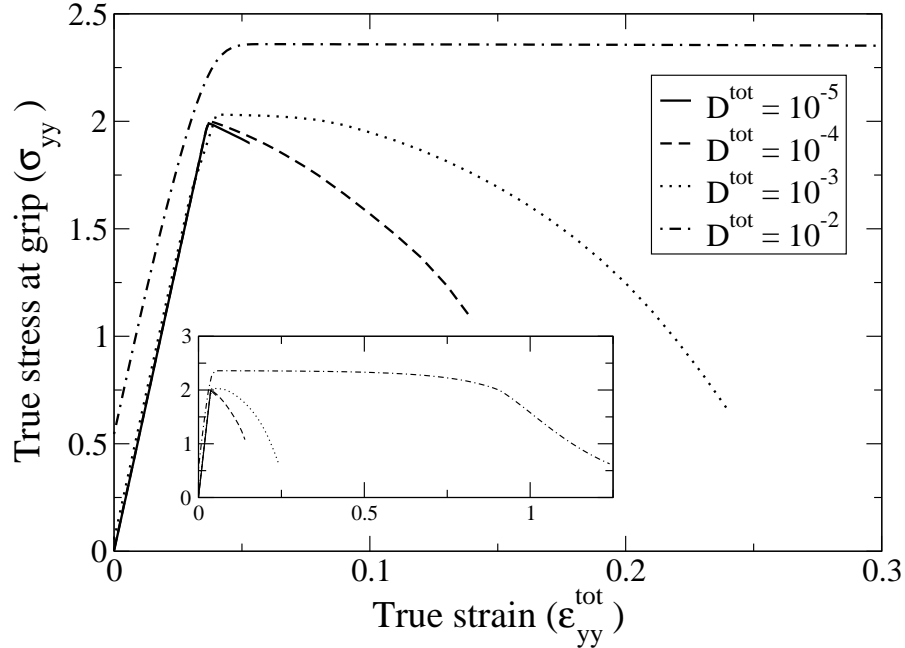


Figure 6.5: The true stress σ_{yy} at the grip plotted against the true total strain $\epsilon_{yy}^{\text{tot}}$ for selected values of D^{tot} . Values of other parameters were $\epsilon_0 = 0.03$, $\mu = 100$, $\nu_2 = 0.5$, and $\Lambda \equiv 1$. The value of D^{tot} had little effect on the “rate”, in terms of strain, at which the stress reached yield; that is to say, all the simulations in this graph yielded approximately at the same strain (the reason the $D^{\text{tot}} = 10^{-2}$ curve starts at a higher stress is explained in Section 4.7). After yield, though, the high strain rate simulations were strained much further before they relaxed. In the slowest simulation, the shear bands were so sharp that the numerics had trouble continuing on past 5% strain. The framed plot shows how long it took before the stress relaxed in the simulation with the highest strain rate.

The effect of varying the total strain rate is shown in Fig. 6.5. The strain rate had little effect on the strain at which the yield stress was reached (although, as explained in Section 4.7, it did influence the initial stress in these simulations). After the system reached yield stress, the simulations with high strain rates took a lot longer (in terms of strain) before they would neck. The higher strain rate meant a higher steady-state stress \bar{s}_∞ , which in turn meant that small geometric

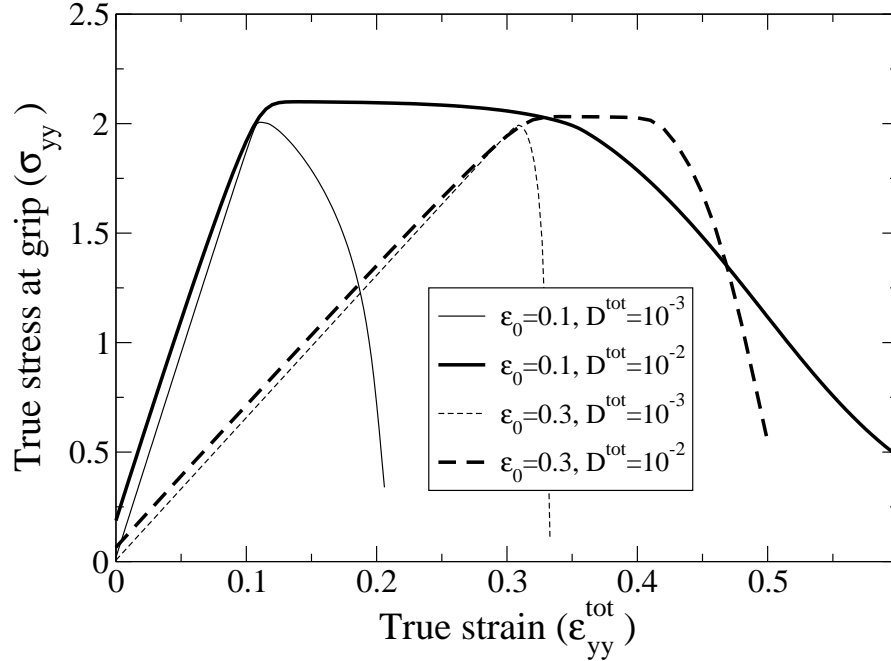


Figure 6.6: The true stress σ_{yy} at the grip plotted against the true total strain $\varepsilon_{yy}^{\text{tot}}$. Again, a higher ε_0 caused a slower rise to yield but a faster relaxation after. The strain rate did not affect the rise to yield, but a faster rate resulted in longer plateaus of “uniform steady-state plastic deformation” before the indented geometry caused a necking instability. Parameter values were $\mu = 100$, $\nu_2 = 0.5$, and $\Lambda \equiv 1$.

inhomogeneities would not be able to separate the stress into regions of $\bar{s} > 1$ and $\bar{s} < 1$. For the low strain rate simulations, the stress localization was more pronounced, and for the lowest rate, the shear bands were so sharp that the numerics was not able to strain the material beyond 5%.

Fig. 6.6 compares stress-strain curves of simulations where both ε_0 and D^{tot} were varied. These curves show clearly that the strain rate primarily changed the time between yield and necking, while ε_0 controlled the dynamics of both the stress increase before yield and the relaxation after.

To gain a better intuition of the necking process, Figs. 6.7 and 6.8 compare

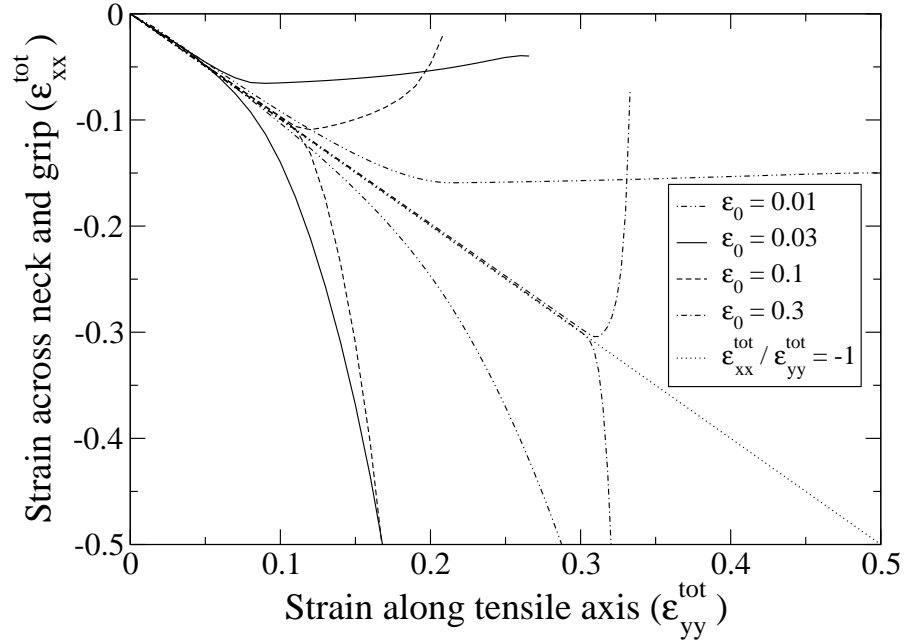


Figure 6.7: The true strain $\varepsilon_{xx}^{\text{tot}}$ across the sample both at the end (grip) and at the middle (neck) as a function of the total strain $\varepsilon_{yy}^{\text{tot}}$ along the sample for various values of ε_0 . When the materials started necking, the strain at the grips would relax back up to zero, while the strain at the center would descend to large negative values as the neck became thinner. Values of other parameters were $D^{\text{tot}} = 10^{-3}$, $\mu = 100$, $\nu_2 = 0.5$, and $\Lambda \equiv 1$.

the strain $\varepsilon_{xx}^{\text{tot}}$ both at the neck and at the end (where the grip was) as a function of the strain $\varepsilon_{yy}^{\text{tot}}$. The curves were taken from the same simulations shown in Figs. 6.4 and 6.5. The upper and lower curves were the strain at the grip and the neck, respectively. The straight line $\varepsilon_{xx}^{\text{tot}} = -\varepsilon_{yy}^{\text{tot}}$ represents the trajectory followed by a uniform material (with no necking) if there were no elastic deformations. In the simulations, the material did neck, and plastic and elastic stored energy was released from the areas near the grips. Consequently, the strain would decrease there, making the ends wider while jamming the plastic flow. These effects were particularly sharp when the value of ε_0 was increased.

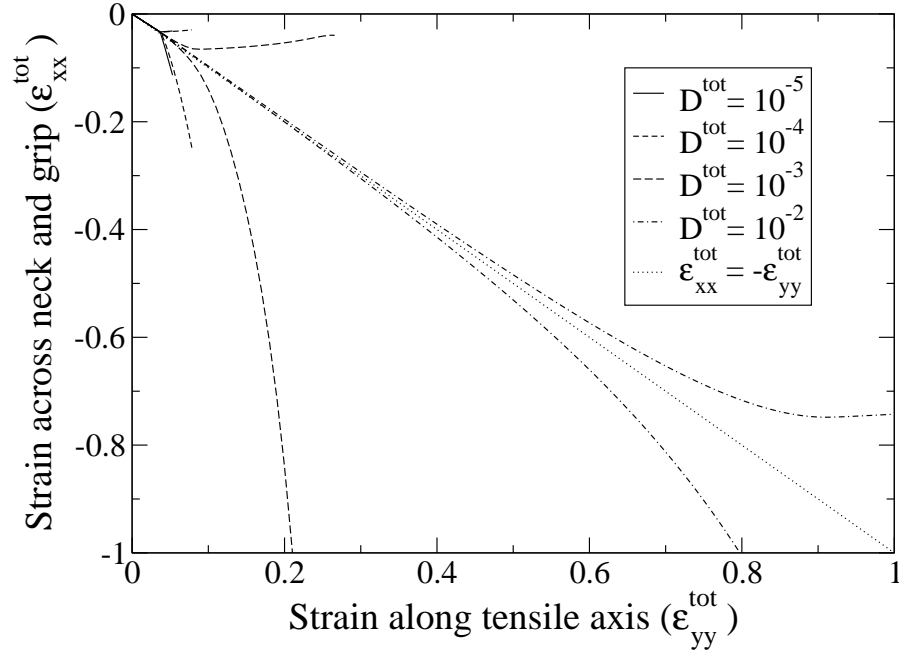


Figure 6.8: The true strain $\varepsilon_{xx}^{\text{tot}}$ both at the end (grip) and at the middle (neck) as a function of the total strain $\varepsilon_{yy}^{\text{tot}}$ for various strain rates, otherwise similar to Fig. 6.7. Note that the curves from the two simulations with the slowest strain rates, $D^{\text{tot}} = 10^{-4}$ and $D^{\text{tot}} = 10^{-5}$, are hard to distinguish (they are in the upper left-hand corner). The values of the parameters were $\varepsilon_0 = 0.03$, $\mu = 100$, $\nu_2 = 0.5$, and $\Lambda \equiv 1$.

If ε_0 had been chosen so that $\varepsilon_0 \ll 1/\mu(1 + \nu_2)$, the first part of the curves in Figs. 6.7 and 6.8 (the upper left-hand corner) would follow $\varepsilon_{xx} = -\nu_2\varepsilon_{yy}$ (this is not shown in the graphs). The material would revert back to $\varepsilon_{xx} = -\varepsilon_{yy}$ after reaching yield and steady-state plastic flow, since at that point there would only be plastic deformation.

6.2 Discussion

In the previous section, a series of necking simulations with different values of the parameters ε_0 and D^{tot} was described. Trends seen in these simulations are

discussed in more depth in the text below.

Fig. 6.9 is a “phase diagram” of the dynamics of the necking simulations, mapping out the behavior as a function of D^{tot} , the total strain rate, and ϵ_0 , the strain due to flipped STZs (Spaepen uses a similar diagram, which he calls a “deformation map”, when he outlines the behavior of amorphous metals in a graph of the temperature versus the stress [20, 21]). It tries to capture the essence of the behavior described in the simulations above, and also includes some information that was derived in earlier chapters. The shaded area shows where the initial stress starts above the yield stress, as described in Section 4.7. It might still be possible to do simulations at these parameter values, but the strain rate would have to be ramped up gradually from a lower value. Unfortunately, the details of the ramping-up procedure would affect the outcome. On one hand, if the strain rate was ramped up too slowly, the material would yield before the strain rate had reached its final value. On the other hand, if it was ramped up too fast, the speed of sound would no longer be negligible and inhomogeneities would form at the grips due to large stress buildups. This is not a numerical effect; it would be true for real experiments as well.

In the area above the solid line, the stress at steady state would be such that the elastic deformations would cause a change in density greater than 1%. Parameter values for the simulations were not chosen from this area since the model assumed that the density would remain constant (see Section 5.7). This was a numerical approximation in the model, and future models might refrain from this assumption in order to investigate behavior in this parameter space.

The three curves running down the center of the graph represent various values (at steady state) of the fraction of stored plastic to elastic energy $\psi^{\text{pl}}/\psi^{\text{el}}$.

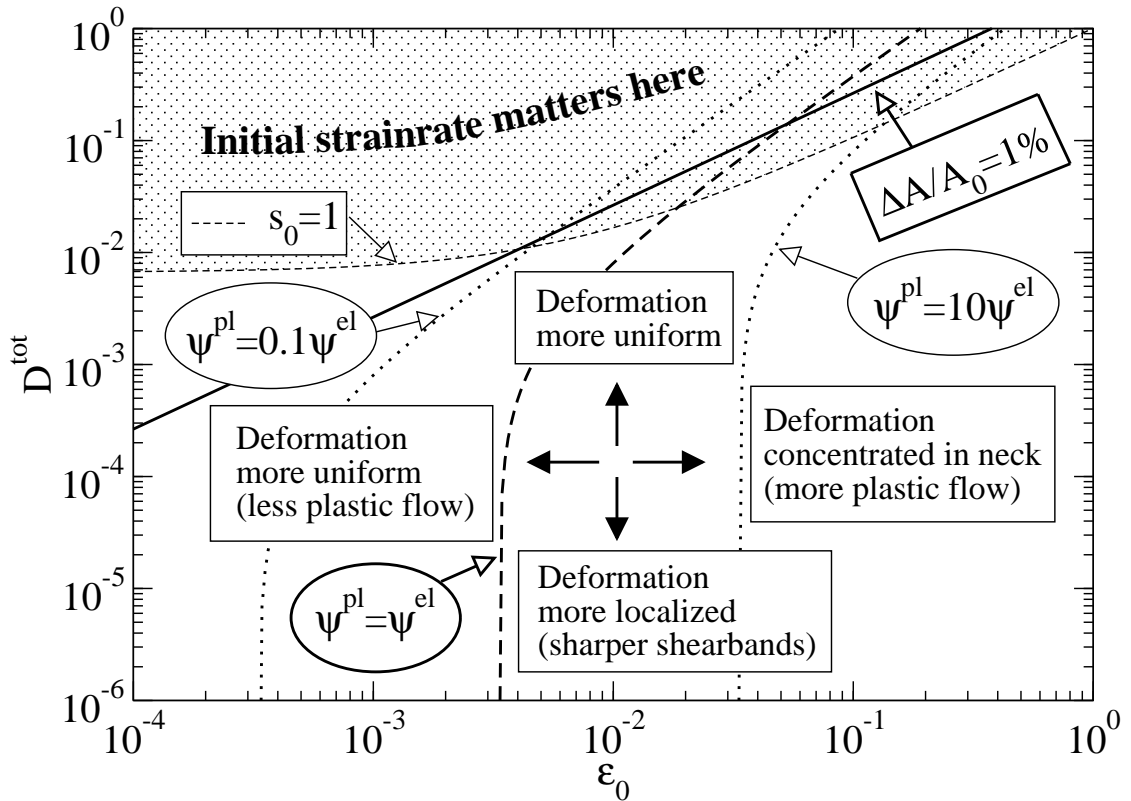


Figure 6.9: A “phase diagram” for the dynamics of constant strain rate necking simulations in the $(D^{\text{tot}}, \epsilon_0)$ parameter space when $\Lambda \equiv 1$, $\mu = 100$, and $\nu_2 = 0.5$. Simulations with a lower total strain rate had more pronounced shear bands. An increased ϵ_0 resulted in more plastic flow, which allowed for sharper necks (in both time and space). The three curves running down through the center indicate various values (at steady state) of the ratio of stored plastic to stored elastic energy. If parameters were chosen from the shaded area at the top, the initial stress (as explained in Section 4.7) would be higher than the yield stress; thus, the strain rate would have to be ramped up from a lower value (perhaps from rest), and the details of how the strain rate was ramped up would affect the outcome of the simulation. The simulations in this dissertation deliberately avoided parameters from this region. Finally, the solid line shows where, at steady state, the change in density due to elastic deformation would reach 1%. To keep the change in density to a minimum, parameter values for the simulations were chosen from below this line.

Specifically, assuming a uniform system (as described in Section 4.4) at steady state (which means that $\tau = \Delta_\tau = 0$, $p = -s$, $\Lambda = 1$, and $\Delta_s = 1/s$), combining Eqs. (4.58) and (4.59) gives

$$\frac{\psi^{\text{pl}}}{\psi^{\text{el}}} = \epsilon_0 \mu (1 + \nu_2) \frac{1 + s^2}{s^4}. \quad (6.1)$$

The curves can be represented parametrically as

$$\{\epsilon_0, D^{\text{tot}}\} = \frac{1}{\mu(1 + \nu_2)} \left(\frac{1+t}{1-t} \right)^{3/2} \left\{ \frac{\sqrt{1-t^2}}{2}, t \right\} \quad \text{with } t \in \langle 0, 1 \rangle. \quad (6.2)$$

Fig. 6.10 shows how the simulations discussed in the previous section fit into the “phase diagram” of Fig. 6.9. Since there was more room in this graph, an additional curve and shading was added to show what parameter values would cause the initial stress to lie between $s_0 = 0.1$ and $s_0 = 1$, the latter being the yield stress. More details about the initial stress can be found in Section 4.7.

Returning to Fig. 6.9, how can the trends summarized there be explained? First, the simulations with higher strain rates had less pronounced shear bands. Since energy was supplied at a faster rate, the material also had to dissipate this energy if it were to stay in steady state. In the slow strain rate simulations, the rate was slow enough that all the dissipated energy could exit through the shear bands; in other words, only the shear bands had stresses above the yield stress. In the simulations with higher strain rates, the system needed to rid itself of more energy per unit time, and thus had to dissipate energy throughout the material. This forced the stress to exceed the yield stress everywhere. Remember that if $\bar{s} > 1$ then $\bar{\Delta} \rightarrow 1/\bar{s}$, while if $\bar{s} < 1$ then $\bar{\Delta} \rightarrow \bar{s}$. Since the plastic flow was proportional to $\epsilon_0(s - \Delta)$ ($\Lambda_0 = 1$ in these simulations), the slowly strained materials saw a large difference between the amount of plastic flow in the shear bands and the rest of the material. The stresses would be above the yield stress in the shear bands and

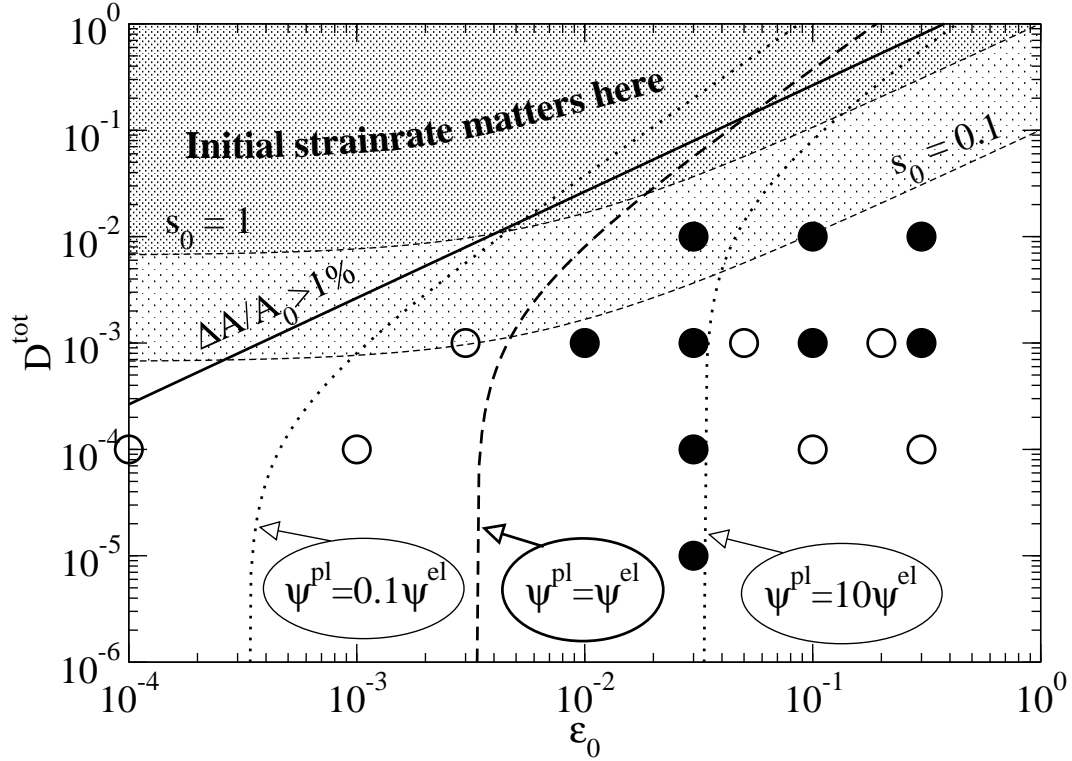


Figure 6.10: This is the same “phase diagram” as in Fig. 6.9, with simulations marked as open and filled circles. The latter are the simulations that were presented in Section 6.1. Parameter values were $\mu = 100$, $\nu_2 = 0.5$, and $\Lambda \equiv 1$. The shaded area added since Fig. 6.9 represents the parameter space where the initial stress would lie between $s_0 = 0.1$ and $s_0 = 1$.

below it elsewhere. Notice how the inhomogeneous geometry played a vital role by breaking the symmetry, concentrating the stresses in certain areas, and thus allowing the shear bands to form. In contrast, the value of the strain rate had little effect on the simulations before the stress reached the yield stress. As long as $\bar{\Delta}$ was low, Γ was negligible, and few STZs were created or annihilated. This implies that the deformation before yield was almost reversible, and that the plastic strain was proportional to $\bar{\Delta}$, the fraction of flipped STZs. Thus the material would always reach the yield stress at the same total (that is, elastic and plastic) strain.

Second, when the parameter ϵ_0 was given high values, the material would have to be strained further before reaching yield stress. This parameter controlled the amount of strain due to flipping STZs, or alternatively, how much of the energy was absorbed in plastic (reversible and irreversible) deformations. When $\epsilon_0 \mu(1 + \nu_2)$, which is approximately proportional to $\psi^{\text{pl}}/\psi^{\text{el}}$, was less than unity, most of the strain energy was stored as elastic strain. This would correspond to $\epsilon_0 < 0.007$ in the above simulations, since $\mu = 100$ and $\nu_2 = 0.5$. As ϵ_0 was increased, the STZs were responsible for more of the deformation, and since the stress is only proportional to the elastic strain, the stress would grow more slowly for large ϵ_0 . That explains why the materials with the smaller ϵ_0 yielded earlier.

Observing the post-yield dynamics, a large value of ϵ_0 ultimately resulted in sharper necks. Once the stress had reached yield, the energy supplied by the work at the grips was no longer being stored in the elastic or plastic deformations (which corresponds to stress and flipped STZs, respectively). Rather, the energy was dissipated through flipping newly created STZs while annihilating the same amount of already-flipped ones. In a homogeneous system the material would just remain in this steady state. In the necking simulations, though, the localized stresses emanating from the indentations perturbed the system enough to change the flow from homogeneous to inhomogeneous. Especially for higher values of ϵ_0 , the neck would narrow rapidly, increasing the stress and plastic flow there until the material would snap in two (in practice, the restricted geometry of the grid would not actually allow the material to split, but the neck would become extremely narrow and the time-step would decrease to a value which was, for all practical purposes, zero). This uncontrolled necking was mainly driven by stored energy being released through plastic dissipation at the neck. Interestingly enough, it was

the stored plastic energy that supplied almost all of the energy; the stored elastic energy was almost negligible when $\epsilon_0 \gg 1/\mu(1 + \nu_2)$. An interesting question is: Would the dynamics change if one refrained from making the approximation (4.27), one of the quasi-linear assumptions? In some versions of the theory, $1/\tau_0^\theta$ would grow small for low stresses, thus preventing the STZs from flipping back [30]. Potentially, this could prevent some of the release of the stored plastic energy from the areas further from the neck.

A large value of ϵ_0 meant that the material needed to be strained further before the stress reached the yield stress since the plastic flow relaxed some of the stresses. Although it took longer for the material to reach the yield stress, once it did the neck developed more rapidly. This was because the increased plastic flow in the neck allowed the ends to relax and release its stored plastic and elastic energy faster. The relaxation of the stress at the ends added even more strain to the center, contributing to the plastic flow at the neck. Finally, as the neck became thinner, the stress would rise there and increase the already high plastic flow even further. Thus the material would neck faster when ϵ_0 was high, since that would reinforce this feedback loop.

When $\epsilon_0 \ll 1/\mu(1 + \nu_2)$, most of the initial work done on the system was stored as elastic energy. After reaching yield stress, the steady-state stress became large (and $\bar{\Delta} = 1/\bar{s}$ small) in order to create enough plastic dissipation \bar{D}^{pl} to counter the steady input of energy supplied by the work done at the ends of the material. There were some faint shear bands where the stresses showed slightly elevated values, but the plastic dissipation was almost uniform throughout the material when ϵ_0 was small.

CHAPTER 7

PRE-ANNEALED MATERIALS

The behavior of a pre-annealed metallic glass is more brittle than both a virgin as-quenched sample and a material that has experienced plastic work. The experiments discussed in Section 3.2 also reported that the pre-annealed solids had a higher density; structural relaxation had packed the molecules more closely together. The STZ theory describes the change in behavior due to annealing through Λ , the relative density of STZs. With less room for the atoms to move, a pre-annealed material would start with an initial value of Λ less than one, $\Lambda_0 < 1$. In a virgin material that has just been quenched from a molten state, the atoms find themselves in more “fluffy” structure, which would correspond to a higher value of Λ . Likewise, if an annealed material is subjected to plastic work, the value of Λ would rise as the tightly packed atoms are “re-fluffed”. Consequently, a material with $\Lambda_0 < 1$ and $\Lambda_0 = 1$ will from now on be referred to as “pre-annealed” and “worked”, respectively, although the latter could also represent a material in its virgin as-quenched state.

Chapter 3 described the effects of using a lower initial value of Λ in the non-tensorial version of the theory. Initially during a constant strain-rate experiment, a small Λ would suppress plastic deformation since there would be very few STZs to flip. As the stress $|s| \rightarrow 1$, most of the existing STZs would be flipped, and new ones would have to be created causing Λ to grow. The lower ϵ_0 was set, the higher the peak stress and steady-state stress would be, and the faster Λ would grow toward one.

The previous chapter assumed that $\Lambda \equiv 1$ throughout. The current chapter describes simulations where pre-annealed materials were used during loading, im-

plemented by setting $\Lambda_0 = 0.01$. A spatially extended two-dimensional simulation allowed Λ to grow locally, thus making it possible for the material to boost the plastic flow even further in areas where the stresses were high. As will be seen, this contribution to the inhomogeneous deformation was particularly pronounced for high values of ϵ_0 .

As in Chapter 6, the simulations had a shear modulus of $\mu = 100$, a Poisson ratio of $\nu_2 = 0.5$, and a numerical viscosity of $\eta = 0.02$. The size of the material was 4×4 , although this time the whole material was simulated (that is, there were no symmetric boundaries). The material was mapped onto a grid measuring 33×33 nodes. The left and right boundaries $X^0(y, t)$ and $X^1(y, t)$ (initially parallel to the y -axis) were both allowed to deform. The lower boundary was held fixed at $y = 0$, while the upper boundary $Y(t)$ was moved at a constant strain rate. See Chapter 5 for more details. The initial density of STZs was set below unity, to $\Lambda_0 = 0.01$. In order to encourage inhomogeneous flow, the free boundaries were made jagged by randomly perturbing the width with values up to 1% of the total width (in other words, after the perturbation $X^1(y, 0) - X^0(y, 0) \in [3.96, 4.04]$). By setting the seed for the random number generator to the same value for all the simulations, the initial geometry would always be the same.

On a side note, some attempts were made to look at the behavior of the pre-annealed materials during compression. The advantage of applying a negative strain rate was that the material was not able to neck or break in two. Most of the simulations were well behaved, but unfortunately the increased local stresses would in some cases (especially for high values of ϵ_0) be extreme enough to cause, among other effects, spurious energy creation (when comparing the rate of work done at the grips to the actual total rate of energy absorbed and dissipated by the system,

the latter would sometimes be 5% or 10% higher than the former). The results from these simulations were therefore not included. After looking into the problem, it is believed that it was mainly numerical in nature, although triggered by harsher physical conditions; for example, there are reports of seeing serrated flow during compression experiments with amorphous metals [22, 78, 79, 80, 81, 82, 83, 84] (keep in mind, though, that the mechanisms that cause serrated flow might not be present in the current version of the STZ model).

The simulations in this chapter illustrate the dynamics of pre-annealed materials in three different ways. First, the distribution and average density of STZs are compared to the dissipated energy and the work done on the systems for different values of ϵ_0 . Second, the dynamics of pre-annealed and worked materials are compared. And third, the following question is addressed: Would the simulations with higher strain rates experience more pronounced shear bands if they were stopped and held at a fixed strain for the same amount of time it would take a slower simulation to reach that same strain?

7.1 Variation in ϵ_0

Fig. 7.1 compares the average density of STZs

$$\Lambda_{\text{avg}} \equiv \frac{1}{A} \int_A \Lambda dA \quad (7.1)$$

(where A is the area of the sample) to the plastic dissipation of energy

$$Q_{\text{sum}} \equiv \int_A Q dA \quad (7.2)$$

for three different values of ϵ_0 . All three simulations were strained at a rate of $D^{\text{tot}} = 10^{-4}$. Each of the three graphs on the left displays three curves, of which

the solid represents the rate of work done on the system at the grip,

$$P_{\text{external}} = F v_y = (X^1 - X^0) \sigma_{yy} v_y. \quad (7.3)$$

F is the force applied to the end of the material, and σ_{yy} , v_y , X^0 , and X^1 were all evaluated at $y = Y(t)$. Since the upper boundary was kept flat and moved perpendicular to its surface, only the y -component of the stress was needed. P_{external} is thus the rate at which energy flowed into the system.

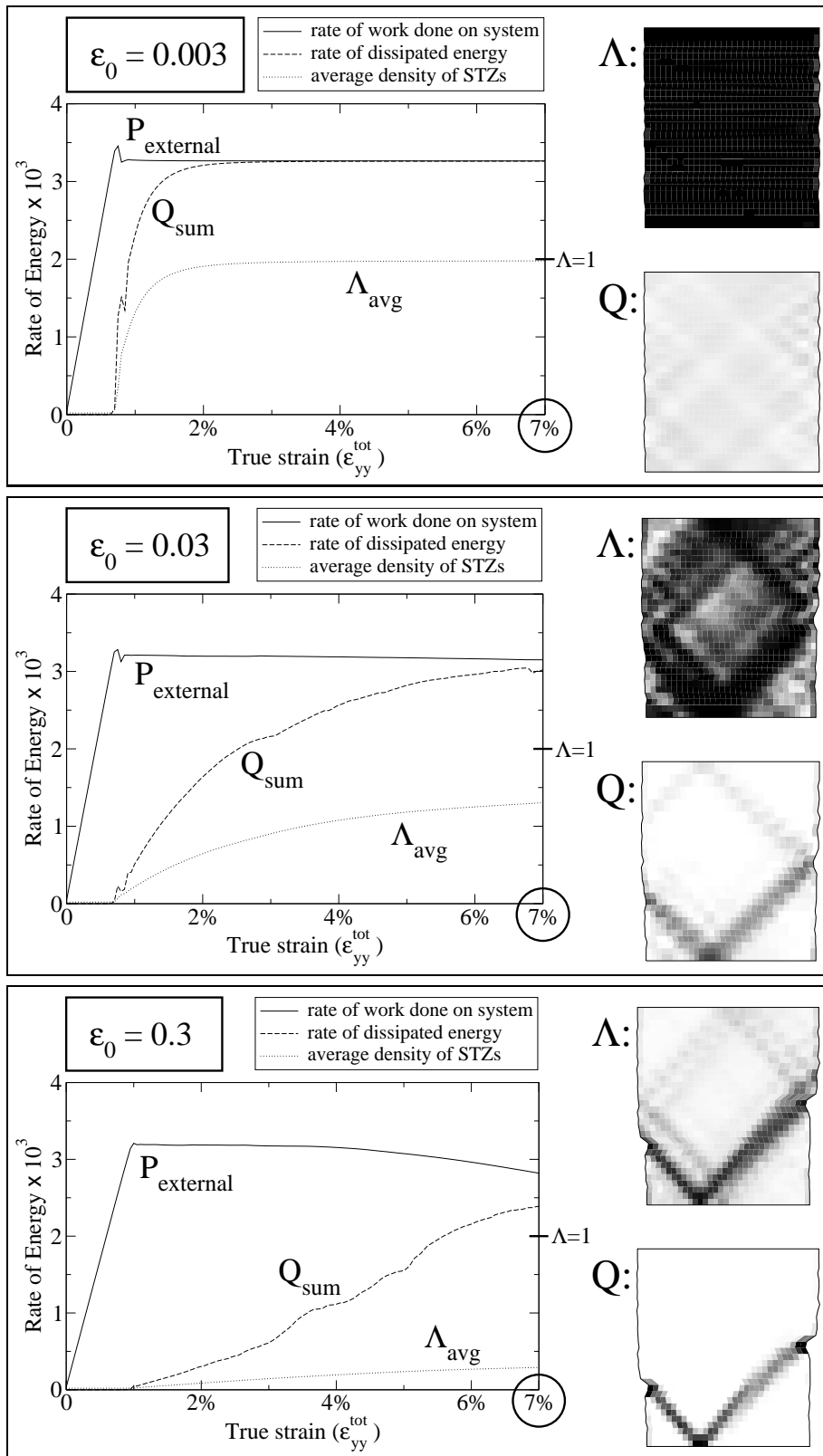
The middle curve in all three graphs shows Q , the rate of energy dissipated due to plastic deformation summed over the whole material. The axis on the left side displays the values for both this curve and that of P_{external} , although they were multiplied by 10^3 to reduce clutter (the interval is really $[0, 0.004]$). The axis on the right sets the scale for the third curve, Λ , which represents the density of STZs averaged over the whole sample.

The two density plots to the right of each of the graphs show the final distributions of Λ and Q when the systems had reached 7% strain. In the density plots for Λ , the shading was scaled so that the interval $[0, 1]$ went from white to black. With Q , the gray scale was mapped onto the interval $[0, 0.003]$, with white again representing zero. In the latter density plots there were occasional points that exceeded 0.003 (these were just painted black as well), but choosing a larger interval would have erased most of the structure seen in the pictures.

In the simulation where $\epsilon_0 = 0.003$, Λ_{avg} quickly rose to one while Q_{sum} grew equal to P_{external} once the stress reached yield. The latter meant that all the energy provided at the grips was dissipated through plastic deformation, and none was stored, after the material reached about 2% strain. In the $\epsilon_0 = 0.3$ simulations, Λ_{avg} never even reached a value of 0.15, and the plastic rate of dissipation grew a lot slower. In fact, looking at the density plot shows that the density of STZs

Figure 7.1: Three pre-annealed simulations with $\Lambda_0 = 0.01$ were run for $\epsilon_0 = 0.003$, $\epsilon_0 = 0.03$, and $\epsilon_0 = 0.3$, all with a strain rate of $D^{\text{tot}} = 10^{-4}$. The graphs on the left show P_{external} , the rate of work done at the grips, Q_{sum} , the rate of dissipated plastic energy summed over the whole material, and Λ_{avg} , the average density of STZs. The left vertical axis shows the range for P_{external} and Q_{sum} (the interval is $[0, 0.004]$), while the right vertical axis displays the scale for Λ_{avg} . The density plots on the right show Λ and Q at 7% strain.

Figure 7.1 (Continued)



only saturated along one band, and the plot for Q shows that this was where most of the plastic dissipation took place as well. The fact that Λ so quickly reached its equilibrium value everywhere in the material for small ϵ_0 meant that the initial value of $\Lambda_0 = 0.01$ had little effect in this case.

Although the density plots of Q and Λ both were snapshots, the latter in some ways gave a cumulative look at what had happened since the start, since Λ could not decay (this is not true in other versions of the STZ theory that, being developed at the time of this writing, incorporate thermal relaxation [66]). In contrast, the density plot of Q is more appropriate when examining the instantaneous dynamics, since it highlights the current rate of plastic deformation in the different areas of the material.

In the simulation with $\epsilon_0 = 0.3$, the rate at which energy flowed into the system, P_{external} , started decaying towards the end. This is because the stress at the grip began to drop due to the increased plastic flow along the shear band. The high value of ϵ_0 allowed the material to deform enough in the small area of this band to account for all the strain imposed by the grip, thus inducing inhomogeneous flow and perhaps cause the material to break at a later time.

7.2 Comparing Pre-Annealed and Worked Materials

Fig. 7.2 compares a pre-annealed and a worked material, having initial conditions of $\Lambda_0 = 0.01$ and $\Lambda_0 = 1$, respectively. The two curves in the center show the true stress-strain curves of these two materials as they were strained beyond yield and toward failure (the materials would eventually grow extremely thin somewhere in the center). The density plots of Q on either side were arbitrarily chosen some time after the materials had yielded, with the stress at the grips being the same

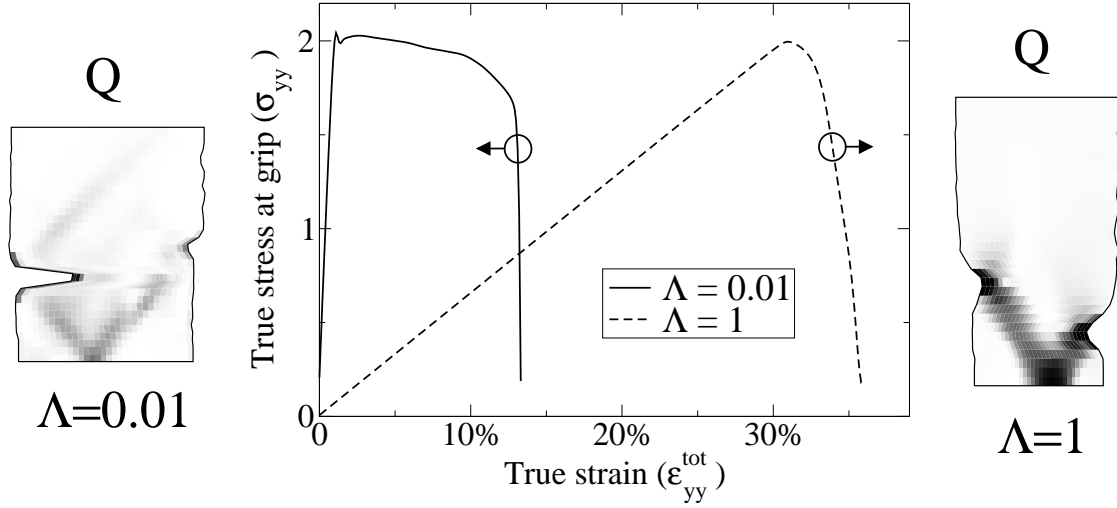


Figure 7.2: The true stress-strain curves for two materials, one with $\Lambda_0 = 0.01$ and one with $\Lambda_0 = 1$. The other parameters were $D^{\text{tot}} = 10^{-3}$ and $\epsilon_0 = 0.3$. The density plots show the plastic rate of dissipation at some arbitrary time after yield, with the stress at the grips being the same in the left and right snapshots.

in the two snapshots. Although the two density plots look different, their initial geometries were identical to each other and to all the other simulations in this chapter.

The only comparison shown here is that of the simulations with $\epsilon_0 = 0.3$. Although no less important, the pre-annealed materials with a lower ϵ_0 would have Λ rise to one everywhere so quickly that the results were essentially the same as for the worked materials; this effect was seen in Fig. 7.1.

A high value of ϵ_0 allowed the stresses to grow more slowly, permitting some areas to reach $\bar{s} > 1$ while others remained at $\bar{s} < 1$ as the material approached yield. Λ would only grow in the resulting shear bands, thus making its average value grow slowly. A slow growing stress (with respect to time) would also occur for small strain rates, resulting in a similar shear-banding effect.

Comparing the stress-strain curves in Fig. 7.2, the pre-annealed material plateaued before breaking. It almost seemed like it was riding along an unstable equilibrium before it increased the density of STZs in one location and then deformed and broke there. In comparison, the worked material would deform substantially more before reaching yield stress, and then “ooze” apart (rather than “break”).

It is tempting, although perhaps somewhat speculative, to compare the necking on the left side of Fig. 7.2 to fracture. Some of the simulations, including this one, had extremely concentrated stresses and narrow necks, and the deformations behaved in many ways similar to brittle cracks. The simulations have shown that there is an interplay between the STZs, the geometry, and stress concentrations. Naturally, the geometry in these simulations was quite restricted, the single-valued boundaries forcing the “crack” to run horizontally rather than following the 45° shear bands as seen in experiments [23, 24]. Also, the resolution was too low to make any good quantitative arguments. Nevertheless, this behavior suggests that the STZ description might be capturing some of the dynamics that is present in fracture¹.

7.3 Strain-Rate Dependent Localization

When comparing the results of the simulations from both the current and previous chapters, the shear bands at a given strain were more pronounced for smaller strain rates. Comparing two identical materials that were strained to 7% at rates of $D^{\text{tot}} = 10^{-4}$ and $D^{\text{tot}} = 10^{-3}$, the former would not only be stretched ten times slower, it would also have ten times as long to relax and deform. Could it be that

¹For more information on fracture in brittle amorphous materials, see the review by Fineberg and Marder [85].

it was not the difference in speed, but the difference in relaxation time that allowed the shear bands to form in the slow case?

Fig. 7.3 shows density plots of Λ at 7% strain where the materials had been strained at the rates mentioned above, with both $\epsilon_0 = 0.03$ and $\epsilon_0 = 0.3$. The system that had been strained at the slower rate, $D^{\text{tot}} = 10^{-4}$, reached 7% at time $t = 700$, while the faster system with a rate of $D^{\text{tot}} = 10^{-3}$ was stopped around $t = 70$ (the snapshot was taken at $t = 75$ to make sure the material had come to a complete stop, reaching its full 7%; in order to stop the material at this exact strain, it was necessary to start slowing it down already at $t = 65$). After stopping the fast system, it was held fixed until $t = 700$, the same amount of time it took the slow system to reach 7% strain.

It turned out that there was practically no change in the quickly-strained material after the grips had come to a halt (this was the case both for $\epsilon_0 = 0.03$ and $\epsilon_0 = 0.3$, although the former ended up with a higher Λ_{avg}). This means that all the deformation took place instantly, not allowing any of the stored energy to escape later.

This does not preclude a situation where a more irregular geometry might induce a stress concentration, allowing both stored plastic and elastic energy to be released, perhaps even driving a necking instability; this kind of behavior was seen in the previous chapter. It does mean, though, that the shear bands were created without the need of instability mechanisms. In fact, the bands of STZs were more pronounced when energy flowed into the system at a slower rate.

The previous section speculated that the STZ theory could perhaps contribute to explain fracture dynamics. The current section seems to contradict this somewhat, at least at first glance. From experience, a material strained at a higher rate

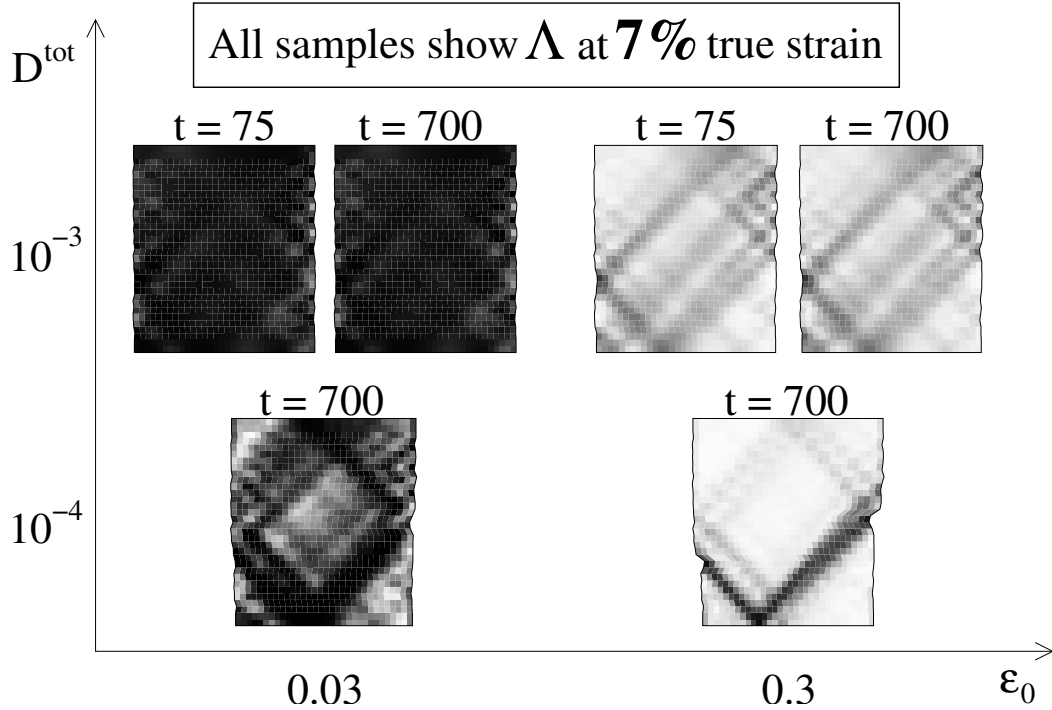


Figure 7.3: Density plots of Λ at 7% strain, both for $\epsilon_0 = 0.03$ and $\epsilon_0 = 0.3$. The systems were strained at rates of $D^{\text{tot}} = 10^{-4}$ and $D^{\text{tot}} = 10^{-3}$, and in the latter case the grip was held fixed at 7% for the same amount of time that it took the slower strain rate to reach this strain. Despite the extra time, no pronounced shear bands developed; in fact, once the grip was stopped, the material hardly changed at all.

seems more brittle, implying that it should have sharper stress concentrations, and more localized shear bands. How could such behavior be compatible with the results shown above?

It was briefly mentioned earlier that, as of this writing, the thermal relaxation is being incorporated into the STZ theory [66]. With that mechanism included, Λ can decrease as STZs are annihilated over time, and this might suppress the creation of localized bands of STZs as the strain rate drops. The model used in this dissertation did not allow Λ to decrease, which might be interpreted as running the simulations close to zero temperature.

CHAPTER 8

CONCLUSION

In addition to showing that a two-dimensional implementation of the STZ theory is capable of describing shear localization, the goal of this dissertation has been to give the whole theory a broad yet detailed presentation. Examples taken from both the zero- and two-dimensional theory, and from a wide range of parameter values, were used to expose the different types of behavior inherent in the model. The geometry, energy flow, and internal state of the material all contributed to the rheology through effects such as jamming and plastic flow, annealing, strain softening, necking, and shear banding.

The STZ model is an example of a physically motivated rate-and-state theory that incorporates both static and time-dependent plastic theory in one compact description. It assumes that plastic flow in an amorphous solid is caused by the non-affine transformation of particles in localized areas, or shear-transformation-zones (STZs). This description, which includes the internal state variables Λ (the relative density of STZs) and Δ (the orientation of the transformed STZs), is then combined with linear elastic theory.

Chapter 3 explored the behavior of a uniform glassy material by using the zero-dimensional, non-tensorial version of the theory developed by Falk and Langer[29, 30]. In steady state, the STZ variables Λ and Δ would allow the material to either jam or flow plastically depending on the value of the deviatoric stress. An initially low value of Λ would mimic the effects of a pre-annealed material, including strain softening when subjected to a constant strain rate. Later these insights were used to explain the behavior, such as shear localization, seen in the two-dimensional inhomogeneous simulations of Chapters 6 and 7.

A tensorial, two-dimensional version of the theory was developed in Chapter 4. The rate of transformation for the STZs was based on the magnitude and direction of the local deviatoric stress, while their rate of creation and annihilation was set proportional to that of the plastic dissipation. A simplified, quasi-linear version of the model was derived, where basically the plastic rate-of-deformation tensor was approximated to be proportional to the difference between the deviatoric stress and the average alignment of the transformed STZs. It was the behavior of this simplified model that was explored throughout most of this dissertation.

Chapters 6 and 7 presented and discussed results obtained from a numerical implementation of the two-dimensional, tensorial version of the STZ theory. The first chapter looked at how the strain rate, the straining-capability of STZs (ϵ_0), and the geometry affected flow and deformation during necking. It was especially striking how sharp shear bands and narrow necks were formed at low strain rates and high ϵ_0 , respectively. The former of these two trends appeared to contradict experimental evidence: An amorphous metal displays increased brittle behavior as it is strained at a higher rate [77], while the opposite seemed true for the simulated materials. The discrepancy stems from the lack of temperature in the current STZ model. There was no mechanism once the simulation had started, apart from plastic deformation, to annihilate existing STZs. In the experiments, the non-zero temperature allowed the molecules in the most strained areas to relax if given enough time. This resulted in more homogeneous flow as the material was strained at lower rates. Efforts are currently underway to incorporate thermal relaxation into the model [66].

The second of the two chapters considered pre-annealed amorphous solids, starting with a lower initial relative density of STZs Λ_0 . Experiments have shown

that amorphous metals become more brittle when annealed, even though no crystallization is detected [60, 61, 62, 63, 64, 65]. Rather, the embrittlement correlates with structural relaxation, leaving the more closely packed molecules less room to move. In the simulations, the lower Λ_0 enhanced the localization of the strain, especially for higher values of ϵ_0 when most of the stored energy was in the form of flipped STZs (rather than elastic strain). Compared to either virgin as-quenched or worked samples, the pre-annealed materials behaved in a more brittle manner with narrower shear bands and something resembling a cleavage fracture. The latter observation should be approached with great caution since the numerical implementation was not designed to handle such extreme deformations. Nevertheless, the similarities between the dynamics of the STZ theory at low Λ_0 and empirically annealed solids were strong enough to warrant further investigation.

As mentioned, an increased value of ϵ_0 would result in more of the applied work being stored as anelastic rather than elastic strain. This was particularly apparent for the virgin materials ($\Lambda_0 = 1$), where an increased ϵ_0 meant that the material would reach yield stress at a much larger total strain. On the one hand, it is possible that the large values of ϵ_0 , which were needed to produce interesting dynamics in the simulations, exaggerated the anelastic strain. On the other hand, $\Lambda_0 \ll 1$ would restrict the plastic strain (and thus the stored plastic energy) to narrow shear bands, causing a mostly elastic behavior before yield and more brittle dynamics at failure. It is possible that the sharp bands of inhomogeneous flow in experimentally deforming amorphous solids are due to an internal structure corresponding to low initial values of Λ ; unless the materials were quenched extremely rapidly and to very low temperatures, chances are that some structural relaxation would occur. Incorporating the earlier mentioned thermal relaxation into the STZ model could

help lower the value of Λ throughout the simulation and yield better agreement with the experimental results.

The STZ theory was created by averaging out the microscopic details of simple amorphous solids. Notwithstanding the geometric restrictions and the quasi-linear approximation, the results presented in this dissertation still show that the theory captures many important rheological features seen experimentally including plastic flow, jamming, necking, annealing, strain softening, shear banding, and soon also thermal relaxation. Since the assumptions on which the STZ theory is based are few and relatively general in nature — the STZs are two-state systems that transform according to the local deviatoric stress — it might also have relevance to other more complex systems such as glassy polymers. It is with great excitement and anticipation that I see the agreement between theory and experiment improve as the STZ description keeps growing more mature.

APPENDIX A

LINEAR STABILITY ANALYSIS OF NUMERICAL ALGORITHMS

Section 5.5 discussed the numerical stability of the implementation of the STZ model, and stated that the integration algorithm would only be stable if the time-step was set low enough. Section 19.1 of Numerical Recipes [76] shows how the von Neumann stability analysis can be used to determine under what conditions an algorithm is stable. This chapter explains how to easily and systematically apply this idea to large systems of numerical equations.

A.1 The Stability Criteria

Assume that there are N fields $(u_\alpha)_j^n$, with $\alpha \in [1, N]$, where n and j are the discrete temporal and spatial coordinates, respectively (thus $t = n\Delta t$ and $x = j\Delta x$). This means that N difference equations are needed to describe how the fields propagate in discrete time:

$$F_\alpha = 0. \tag{A.1}$$

In general, F_α can be a function of all the fields u_α at all time-steps n and all locations j . More often, though, F_α is just a function of the u_α at times n and $n + 1$, and at locations $j - 1$, j and $j + 1$ (sometimes also at $j - 2$ and $j + 2$). If this is confusing, take a look at the examples.

Assuming that a constant stationary solution u_α^* is known (that is, constant with respect to n and j), the stability condition is

$$|\xi| \leq 1, \tag{A.2a}$$

where ξ is the solution of

$$\det(A) = 0 \tag{A.2b}$$

and the matrix A is given by

$$A_{\alpha\beta} = \sum_{p,m} \frac{\partial F_\alpha}{\partial (u_\beta)_{j+m}^{n+p}} \xi^p e^{ik\Delta xm} \quad (\text{A.2c})$$

(See Section A.3 for the derivation). The partial derivatives $\partial F_\alpha / \partial u_\beta$ are evaluated at $u_\beta = u_\beta^*$. For example, if F_α only depends on u_α at n and $n+1$, and $j-1$, j , and $j+1$, Eq. (A.2c) reduces to

$$A_{\alpha\beta} = \sum_{m=0,\pm 1} \left(\frac{\partial F_\alpha}{\partial (u_\beta)_{j+m}^n} + \frac{\partial F_\alpha}{\partial (u_\beta)_{j+m}^{n+1}} \xi \right) e^{ik\Delta xm}. \quad (\text{A.3})$$

A.2 Examples

A.2.1 Advection Equation with Explicit Euler

The analytical advection equation is given by

$$\frac{\partial u}{\partial t} = -v \frac{\partial u}{\partial x}, \quad (\text{A.4})$$

where the velocity v is constant. In this case the solution is known: a wave $f(x-vt)$ (of any shape) moving in the positive x -direction.

Using a numerical scheme that is fully explicit (forward in time), and a symmetric derivative on the right-hand side, the difference equation becomes

$$\frac{u_j^{n+1} - u_j^n}{\Delta t} = -v \frac{u_{j+1}^n - u_{j-1}^n}{2\Delta x}. \quad (\text{A.5})$$

This scheme is first order in time and second order in space. Moving everything to the left-hand side (and multiplying with Δt for aesthetic reasons),

$$F = u_j^{n+1} - u_j^n + \frac{v\Delta t}{2\Delta x} (u_{j+1}^n - u_{j-1}^n) = 0. \quad (\text{A.6})$$

Since there is only one difference equation ($N = 1$), the α subscript is dropped.

The only partial differentials left are

$$\begin{aligned} \frac{\partial F}{\partial u_j^{n+1}} &= 1, & \frac{\partial F}{\partial u_j^n} &= -1, \\ \frac{\partial F}{\partial u_{j+1}^n} &= \frac{v\Delta t}{2\Delta x}, & \frac{\partial F}{\partial u_{j-1}^n} &= -\frac{v\Delta t}{2\Delta x}. \end{aligned} \quad (\text{A.7})$$

The matrix A now only has one component, which is

$$\begin{aligned} A &= \xi - 1 + \frac{v\Delta t}{2\Delta x} (e^{ik\Delta x} - e^{-ik\Delta x}) \\ &= \xi - 1 + \frac{iv\Delta t}{\Delta x} \sin(k\Delta x). \end{aligned} \quad (\text{A.8})$$

Setting $\det(A) = A = 0$, one can solve for ξ . Taking the absolute value gives

$$|\xi| = 1 + \left[\frac{v\Delta t}{\Delta x} \sin(k\Delta x) \right]^2, \quad (\text{A.9})$$

which is always greater than or equal to one. The advection equation with the explicit time scheme is thus unconditionally unstable.

A.2.2 Diffusion Equation with Explicit Euler

The diffusion equation is

$$\frac{\partial u}{\partial t} = \eta \frac{\partial^2 u}{\partial x^2}, \quad (\text{A.10})$$

where η is the diffusion constant. Using an explicit time scheme and a symmetric Laplacian,

$$F = u_j^{n+1} - u_j^n - \frac{\eta\Delta t}{\Delta x^2} (u_{j+1}^n - 2u_j^n + u_{j-1}^n) = 0. \quad (\text{A.11})$$

This time the partial derivatives read

$$\begin{aligned} \frac{\partial F}{\partial u_j^{n+1}} &= 1, & \frac{\partial F}{\partial u_j^n} &= \frac{2\eta\Delta t}{\Delta x^2} - 1, \\ \frac{\partial F}{\partial u_{j+1}^n} &= -\frac{\eta\Delta t}{\Delta x^2}, & \frac{\partial F}{\partial u_{j-1}^n} &= -\frac{\eta\Delta t}{\Delta x^2}. \end{aligned} \quad (\text{A.12})$$

which gives

$$\begin{aligned}
A &= \xi - 1 - \frac{\eta\Delta t}{\Delta x^2} (e^{ik\Delta x} + e^{-ik\Delta x} - 2) \\
&= \xi - 1 - \frac{2\eta\Delta t}{\Delta x^2} (\cos(k\Delta x) - 1) \\
&= \xi - 1 + \frac{4\eta\Delta t}{\Delta x^2} \sin^2\left(\frac{k\Delta x}{2}\right). \tag{A.13}
\end{aligned}$$

Again, set $\det(A) = A = 0$ and solve for ξ . Requiring $|\xi| < 1$, stability can now be ensured by requiring $4\eta\Delta t/\Delta x^2 < 2$, or

$$\Delta t < \frac{\Delta x^2}{2\eta}. \tag{A.14}$$

A.2.3 Diffusion Equation with Second-Order Runge-Kutta in One Dimension

The algorithm for the Runge-Kutta scheme is described in Eq. (5.6). If the equation of motion is given by Eq. (5.5), then the discrete diffusion equation has

$$f[u^n] = \eta \frac{u_{j+1}^n - 2u_j^n + u_{j-1}^n}{\Delta x^2}, \tag{A.15}$$

and thus

$$\begin{aligned}
F &= u_j^{n+1} - u_j^n (1 - 2B + 3B^2) \\
&\quad - (u_{j-1}^n + u_{j+1}^n)B(1 - 2B) - (u_{j-2}^n + u_{j+2}^n)\frac{B^2}{2} = 0 \tag{A.16}
\end{aligned}$$

where $B = \eta\Delta t/\Delta x^2$. This gives

$$A = \xi - 2 \left[2 \sin^2\left(\frac{k\Delta x}{2}\right) \frac{\eta\Delta t}{\Delta x^2} - \frac{1}{2} \right]^2 - \frac{1}{2}. \tag{A.17}$$

Setting $\det(A) = A = 0$, it is immediately clear that $\xi \geq \frac{1}{2}$ always. Thus the system will be stable if $\xi < 1$. This means that

$$-\frac{1}{2} < 2 \sin^2\left(\frac{k\Delta x}{2}\right) \frac{\eta\Delta t}{\Delta x^2} - \frac{1}{2} < \frac{1}{2} \tag{A.18}$$

or

$$0 < \Delta t < \frac{1}{2\eta} \frac{\Delta x^2}{\sin^2\left(\frac{k\Delta x}{2}\right)}. \quad (\text{A.19})$$

It is important that the system is stable for all values of k . This is achieved by assigning k the value that restricts Δt the most. In this case, that is $k = 2\pi/(2\Delta x)$, which corresponds to a wavelength of two grid points; this is the shortest possible wavelength on a grid. Since Δt is always positive, the restriction on the time-step for the system to be stable is

$$\Delta t < \frac{\Delta x^2}{2\eta}. \quad (\text{A.20})$$

A.2.4 Diffusion Equation with Second-Order Runge-Kutta in Two Dimensions

This section will repeat the analysis of the previous section, but the field $u_{i,j}$ will be two-dimensional where i and j are the x and y indices, respectively (thus $x = i\Delta x$ and $y = j\Delta y$). The formula for the second-order Runge-Kutta, Eq. (5.6), still holds, but Eq. (A.15) now becomes

$$f[u^n] = \eta \left(\frac{u_{i+1,j}^n - 2u_{i,j}^n + u_{i-1,j}^n}{\Delta x^2} + \frac{u_{i,j+1}^n - 2u_{i,j}^n + u_{i,j-1}^n}{\Delta y^2} \right). \quad (\text{A.21})$$

Following the usual procedure,

$$\xi = 2 \left[2 \sin^2\left(\frac{k_x \Delta x}{2}\right) \frac{\eta \Delta t}{\Delta x^2} + 2 \sin^2\left(\frac{k_y \Delta y}{2}\right) \frac{\eta \Delta t}{\Delta y^2} - \frac{1}{2} \right]^2 + \frac{1}{2}. \quad (\text{A.22})$$

Again $\xi \geq \frac{1}{2}$, and requiring $\xi < 1$ gives

$$\Delta t < \frac{1}{2\eta} \frac{1}{\frac{\sin^2\left(\frac{k_x \Delta x}{2}\right)}{\Delta x^2} + \frac{\sin^2\left(\frac{k_y \Delta y}{2}\right)}{\Delta y^2}}. \quad (\text{A.23})$$

This time the toughest restriction on Δt is achieved by choosing $k_x = 2\pi/(2\Delta x)$ and $k_y = 2\pi/(2\Delta y)$; again, the smallest wavelengths possible on a grid. The

stability condition thus becomes

$$\Delta t < \frac{1}{2\eta} \frac{1}{\frac{1}{\Delta x^2} + \frac{1}{\Delta y^2}}. \quad (\text{A.24})$$

This is the condition used in Section 5.5.

A.2.5 Wave Equation with Lax

This final example is included to show how the stability analysis can be done when there are more than one field. The wave equation reads

$$\frac{\partial^2 u}{\partial t^2} = v^2 \frac{\partial^2 u}{\partial x^2}. \quad (\text{A.25})$$

To simplify, this is rewritten as

$$\frac{\partial u_1}{\partial t} = v \frac{\partial u_2}{\partial x} \quad \text{and} \quad \frac{\partial u_2}{\partial t} = v \frac{\partial u_1}{\partial x}, \quad (\text{A.26})$$

where

$$u_1 \equiv v \frac{\partial u}{\partial x} \quad \text{and} \quad u_2 \equiv \frac{\partial u}{\partial t}. \quad (\text{A.27})$$

There are now two difference equations,

$$F_1 = (u_1)_j^{n+1} - (u_1)_j^n - \frac{v\Delta t}{2\Delta x} [(u_2)_{j+1}^n - (u_2)_{j-1}^n], \quad (\text{A.28a})$$

$$F_2 = (u_2)_j^{n+1} - (u_2)_j^n - \frac{v\Delta t}{2\Delta x} [(u_1)_{j+1}^n - (u_1)_{j-1}^n]. \quad (\text{A.28b})$$

Since $N = 2$, A is a 2×2 matrix:

$$A = \begin{bmatrix} \xi - 1 & -\frac{iv\Delta t}{\Delta x} \sin(k\Delta x) \\ -\frac{iv\Delta t}{\Delta x} \sin(k\Delta x) & \xi - 1 \end{bmatrix}. \quad (\text{A.29})$$

Setting $\det(A) = 0$, the two eigenvalues are found to be

$$\xi = 1 \pm i \frac{v\Delta t}{\Delta x} \sin(k\Delta x). \quad (\text{A.30})$$

Since $|\xi|$ is always greater than or equal to one (for both roots), this algorithm is unconditionally unstable.

A.3 Derivation of the Stability Criteria Formulas

This section derives the general form of the stability condition, Eqs. (A.2). Start by expanding F_α around the stationary solutions u_α^* ,

$$\begin{aligned}
0 &= F_\alpha(\{(u_\alpha)_j^n\}) \\
&= F_\alpha(\{u_\alpha^* + (\delta u_\alpha)_j^n\}) \\
&= \sum_{\beta,p,m} \frac{\partial F_\alpha}{\partial (u_\beta)_{j+m}^{n+p}} (\delta u_\beta)_{j+m}^{n+p} + \mathcal{O}(\delta u^2), \tag{A.31}
\end{aligned}$$

where the partial derivatives $\partial F_\alpha / \partial u_\alpha$ are evaluated at $u_\alpha = u_\alpha^*$.

It was said earlier that u_α^* needs to be constant with respect to both time and space. This restriction is perhaps harsher than necessary, but usually there is no need for a more delicate approach. If u_α^* changes in time (that is, not a stationary solution), then it usually become exceedingly hard to find a criterion on Δt such that $|\xi| \leq 1$. If u_α^* has spatial variations, the stability criteria will vary over the grid, and one would have to calculate this at each grid point. There is one case where a varying initial field would be relatively simple to do: when $(u_\alpha^*)_j^n = \exp(ik^* \Delta x j) \exp(-i\omega^* \Delta t n)$. Having u_α^* constant is just the special case $k^* = 0$, $\omega^* = 0$. Note that the spatial frequency of the initial configuration k^* is different from the frequency of the perturbation k .

Returning to Eq. (A.31), look only at perturbations at wavelength k by using

$$(\delta u_\alpha)_j^n = \xi^n e^{ik \Delta x j} h_\alpha. \tag{A.32}$$

The h_α are the initial amplitudes of the perturbations. In order for the system to be stable, it is required that $|\xi| < 1$, where ξ can be a complex number. It will turn out that, essentially, the solutions for ξ are the eigenvalues of the system, and the h_α are the corresponding eigenvectors.

Inserting Eq. (A.32) into (A.31) and dividing by $\xi^n \exp(ik\Delta x j)$,

$$\sum_{\beta,p,m} \frac{\partial F_\alpha}{\partial (u_\beta)_{j+m}^{n+p}} \xi^p e^{ik\Delta x m} h_\beta = \sum_{\beta} A_{\alpha\beta} h_\beta = A\mathbf{h} = 0. \quad (\text{A.33})$$

(Here the definition (A.2c) was used for A). To find a nontrivial solution ($\mathbf{h} \neq 0$), it is necessary that $\det(A) = 0$. If $\alpha \in [1, N]$, this should give a polynomial of order N , and thus N eigenvalues ξ . In order for the scheme to be stable, all the eigenvalues must satisfy $|\xi| \leq 1$.

APPENDIX B

MAPPING THE VARIABLES ONTO A UNIT SQUARE

As explained in Section 5.2, the numerical implementation of the STZ model mapped the physical coordinates onto a unit square. This chapter presents the derivation of the temporal and spatial derivatives in the new coordinates, as well as the transformed equations of motion. The derivation includes the mapping for both the necking simulations in Chapter 6, which has symmetry conditions along the x and y axes and only one deforming boundary, and for the simulations of the pre-annealed materials in Chapter 7, which has no symmetric boundaries and two deforming edges.

B.1 Prelude

To gain some insight before tackling the real problem, a simpler transformation will be considered first:

$$\zeta_x = \frac{x}{X(t)}, \quad \zeta_y = \frac{y}{Y(t)}, \quad \tilde{t} = t. \quad (\text{B.1})$$

Using the chain rule, one can write

$$\frac{\partial}{\partial x} = \frac{\partial \zeta_x}{\partial x} \frac{\partial}{\partial \zeta_x} + \frac{\partial \zeta_y}{\partial x} \frac{\partial}{\partial \zeta_y} + \frac{\partial \tilde{t}}{\partial x} \frac{\partial}{\partial \tilde{t}}, \quad (\text{B.2a})$$

$$\frac{\partial}{\partial y} = \frac{\partial \zeta_x}{\partial y} \frac{\partial}{\partial \zeta_x} + \frac{\partial \zeta_y}{\partial y} \frac{\partial}{\partial \zeta_y} + \frac{\partial \tilde{t}}{\partial y} \frac{\partial}{\partial \tilde{t}}, \quad (\text{B.2b})$$

$$\frac{\partial}{\partial t} = \frac{\partial \zeta_x}{\partial t} \frac{\partial}{\partial \zeta_x} + \frac{\partial \zeta_y}{\partial t} \frac{\partial}{\partial \zeta_y} + \frac{\partial \tilde{t}}{\partial t} \frac{\partial}{\partial \tilde{t}}, \quad (\text{B.2c})$$

and the first derivatives thus take the form

$$\frac{\partial}{\partial x} = \frac{1}{X(t)} \frac{\partial}{\partial \zeta_x} \quad (\text{B.3a})$$

$$\frac{\partial}{\partial y} = \frac{1}{Y(t)} \frac{\partial}{\partial \zeta_y} \quad (\text{B.3b})$$

$$\frac{\partial}{\partial t} = -\zeta_x \frac{\dot{X}(t)}{X(t)} \frac{\partial}{\partial \zeta_x} - \zeta_y \frac{\dot{Y}(t)}{Y(t)} \frac{\partial}{\partial \zeta_y} + \frac{\partial}{\partial \tilde{t}}. \quad (\text{B.3c})$$

Consequently, the total time derivative becomes

$$\begin{aligned} \frac{d}{dt} &= \frac{\partial}{\partial t} + \frac{\partial x}{\partial t} \frac{\partial}{\partial x} + \frac{\partial y}{\partial t} \frac{\partial}{\partial y} \\ &= \frac{\partial}{\partial t} + v_x \frac{\partial}{\partial x} + v_y \frac{\partial}{\partial y} \\ &= \frac{\partial}{\partial \tilde{t}} - \frac{\zeta_x \dot{X}(t) - v_x}{X(t)} \frac{\partial}{\partial \zeta_x} - \frac{\zeta_y \dot{Y}(t) - v_y}{Y(t)} \frac{\partial}{\partial \zeta_y}. \end{aligned} \quad (\text{B.4})$$

B.2 One Deforming Edge

The exercise in the previous section will now be repeated, except this time a slightly more complicated transformation is used:

$$\zeta_x = \frac{x}{X(y, t)}, \quad \zeta_y = \frac{y}{Y(t)}, \quad \tilde{t} = t. \quad (\text{B.5})$$

The only problem is that X needs to be a function of ζ_y , not y . Thus a small detour is required. Write the transform as

$$x = \zeta_x \mathcal{X}(\zeta_y, \tilde{t}), \quad y = \zeta_y \mathcal{Y}(\tilde{t}), \quad t = \tilde{t}. \quad (\text{B.6})$$

The differentials in the two different coordinate systems are connected by

$$\begin{pmatrix} dx \\ dy \\ dt \end{pmatrix} = A \begin{pmatrix} d\zeta_x \\ d\zeta_y \\ d\tilde{t} \end{pmatrix} \quad (\text{B.7})$$

where

$$A = \begin{pmatrix} \mathcal{X} & \zeta_x \frac{\partial \mathcal{X}}{\partial \zeta_y} & \zeta_x \frac{\partial \mathcal{X}}{\partial t} \\ 0 & \mathcal{Y} & \zeta_y \frac{\partial \mathcal{Y}}{\partial t} \\ 0 & 0 & 1 \end{pmatrix}. \quad (\text{B.8})$$

The inverse is

$$A^{-1} = \begin{pmatrix} \frac{1}{\mathcal{X}} & -\frac{\zeta_x}{\mathcal{X}\mathcal{Y}} \frac{\partial \mathcal{X}}{\partial \zeta_y} & \frac{\zeta_x}{\mathcal{X}} \left(\frac{\zeta_y}{\mathcal{Y}} \frac{\partial \mathcal{X}}{\partial \zeta_y} \frac{\partial \mathcal{Y}}{\partial t} - \frac{\partial \mathcal{X}}{\partial t} \right) \\ 0 & \frac{1}{\mathcal{Y}} & -\frac{\zeta_y}{\mathcal{Y}} \frac{\partial \mathcal{Y}}{\partial t} \\ 0 & 0 & 1 \end{pmatrix}. \quad (\text{B.9})$$

Further, the partial derivatives are linked by

$$\begin{pmatrix} \frac{\partial}{\partial x} \\ \frac{\partial}{\partial y} \\ \frac{\partial}{\partial t} \end{pmatrix} = (A^{-1})^T \begin{pmatrix} \frac{\partial}{\partial \zeta_x} \\ \frac{\partial}{\partial \zeta_y} \\ \frac{\partial}{\partial t} \end{pmatrix}. \quad (\text{B.10})$$

Now, the total time derivative is given by

$$\begin{aligned} \frac{d}{dt} &= \begin{pmatrix} v_x & v_y & 1 \end{pmatrix} \begin{pmatrix} \frac{\partial}{\partial x} \\ \frac{\partial}{\partial y} \\ \frac{\partial}{\partial t} \end{pmatrix} \\ &= \begin{pmatrix} v_x & v_y & 1 \end{pmatrix} (A^{-1})^T \begin{pmatrix} \frac{\partial}{\partial \zeta_x} \\ \frac{\partial}{\partial \zeta_y} \\ \frac{\partial}{\partial t} \end{pmatrix} \\ &= \left[A^{-1} \begin{pmatrix} v_x \\ v_y \\ 1 \end{pmatrix} \right]^T \begin{pmatrix} \frac{\partial}{\partial \zeta_x} \\ \frac{\partial}{\partial \zeta_y} \\ \frac{\partial}{\partial t} \end{pmatrix}. \end{aligned} \quad (\text{B.11})$$

Writing these equations out in full using $\mathcal{X}_y \equiv \partial\mathcal{X}/\partial\zeta_y$ gives

$$\frac{\partial}{\partial x} = \frac{1}{\mathcal{X}} \frac{\partial}{\partial \zeta_x}, \quad (\text{B.12a})$$

$$\frac{\partial}{\partial y} = \frac{1}{\mathcal{Y}} \left(\frac{\partial}{\partial \zeta_y} - \mathcal{X}_y \frac{\zeta_x}{\mathcal{X}} \frac{\partial}{\partial \zeta_x} \right), \quad (\text{B.12b})$$

$$\frac{\partial}{\partial t} = \frac{\partial}{\partial \tilde{t}} + \left(\omega_{xt} - \mathcal{X}_y \frac{\zeta_x}{\mathcal{X}} \omega_{yt} \right) \frac{\partial}{\partial \zeta_x} + \omega_{yt} \frac{\partial}{\partial \zeta_y}, \quad (\text{B.12c})$$

and

$$\frac{d}{dt} = \frac{\partial}{\partial \tilde{t}} + \left(\Omega_x - \mathcal{X}_y \frac{\zeta_x}{\mathcal{X}} \Omega_y \right) \frac{\partial}{\partial \zeta_x} + \Omega_y \frac{\partial}{\partial \zeta_y}, \quad (\text{B.13})$$

where

$$\omega_{xt} = -\frac{\zeta_x}{\mathcal{X}} \frac{\partial \mathcal{X}}{\partial \tilde{t}}, \quad \omega_{yt} = -\frac{\zeta_y}{\mathcal{Y}} \frac{d\mathcal{Y}}{d\tilde{t}}, \quad (\text{B.14a})$$

$$\Omega_x = \frac{1}{\mathcal{X}} \left(v_x - \zeta_x \frac{\partial \mathcal{X}}{\partial \tilde{t}} \right), \quad \Omega_y = \frac{1}{\mathcal{Y}} \left(v_y - \zeta_y \frac{d\mathcal{Y}}{d\tilde{t}} \right). \quad (\text{B.14b})$$

The second derivatives, using $\mathcal{X}_{yy} \equiv \partial^2 \mathcal{X} / \partial \zeta_y^2$, are given by

$$\frac{\partial^2}{\partial x^2} = \frac{1}{\mathcal{X}^2} \frac{\partial^2}{\partial \zeta_x^2}, \quad (\text{B.15a})$$

$$\begin{aligned} \frac{\partial^2}{\partial y^2} &= \frac{[2\mathcal{X}_y^2 - \mathcal{X}\mathcal{X}_{yy}]\zeta_x}{(\mathcal{X}\mathcal{Y})^2} \frac{\partial}{\partial \zeta_x} - \frac{2\mathcal{X}_y\zeta_x}{\mathcal{X}\mathcal{Y}^2} \frac{\partial^2}{\partial \zeta_x \partial \zeta_y} \\ &\quad + \left(\frac{\mathcal{X}_y\zeta_x}{\mathcal{X}\mathcal{Y}} \right)^2 \frac{\partial^2}{\partial \zeta_x^2} + \frac{1}{\mathcal{Y}^2} \frac{\partial^2}{\partial \zeta_y^2}, \end{aligned} \quad (\text{B.15b})$$

$$\frac{\partial^2}{\partial x \partial y} = \frac{1}{\mathcal{X}\mathcal{Y}} \frac{\partial^2}{\partial \zeta_x \partial \zeta_y} - \frac{\mathcal{X}_y}{\mathcal{X}^2\mathcal{Y}} \left(\frac{\partial}{\partial \zeta_x} + \zeta_x \frac{\partial^2}{\partial \zeta_x^2} \right). \quad (\text{B.15c})$$

The Laplacian can be written as

$$\nabla^2 = \left(\frac{1}{\mathcal{X}^2} + \frac{\omega_{xy}^2}{\mathcal{Y}^2} \right) \frac{\partial^2}{\partial \zeta_x^2} + \frac{1}{\mathcal{Y}^2} \left(\frac{\partial^2}{\partial \zeta_y^2} - \frac{\partial \omega_{xy}}{\partial \zeta_y} \frac{\partial}{\partial \zeta_x} - 2\omega_{xy} \frac{\partial^2}{\partial \zeta_x \partial \zeta_y} \right) \quad (\text{B.16})$$

where

$$\omega_{xy} \equiv \frac{\mathcal{X}_y}{\mathcal{X}} \zeta_x. \quad (\text{B.17})$$

Having introduced \mathcal{X} and \mathcal{Y} means that two more equations of motion are needed. In the original coordinate system (x, y, t) ,

$$\frac{dX}{dt} = v_x(x = X, y, t), \quad (\text{B.18a})$$

$$\frac{dY}{dt} = v_y(x, y = Y, t) = V. \quad (\text{B.18b})$$

This needs to be written in the other coordinate system, $(\zeta_x, \zeta_y, \tilde{t})$. Using Eq. (B.13),

$$\frac{d\mathcal{Y}}{d\tilde{t}} = \frac{dY}{dt} = \tilde{v}_y(\zeta_x, 1, \tilde{t}) = \tilde{v}_y(1, 1, \tilde{t}) = V, \quad (\text{B.19a})$$

$$\begin{aligned} \frac{\partial \mathcal{X}}{\partial \tilde{t}} &= \frac{dX}{dt} - (\Omega_x - \omega_{xy}\Omega_y) \frac{\partial \mathcal{X}}{\partial \zeta_x} - \Omega_y \frac{\partial \mathcal{X}}{\partial \zeta_y} \\ &= \tilde{v}_x(1, \zeta_y, \tilde{t}) - \frac{1}{\mathcal{Y}} [\tilde{v}_y(1, \zeta_y, \tilde{t}) - \zeta_y V] \frac{\partial \mathcal{X}}{\partial \zeta_y}. \end{aligned} \quad (\text{B.19b})$$

Remember that physically $X = \mathcal{X}$ and $Y = \mathcal{Y}$. The notational difference is just used as a reminder of what coordinate system they are expressed in.

Eqs. (B.12) and (B.13) can now be rewritten as

$$\frac{\partial}{\partial x} = \frac{1}{\mathcal{X}} \frac{\partial}{\partial \zeta_x}, \quad (\text{B.20a})$$

$$\frac{\partial}{\partial y} = \frac{1}{\mathcal{Y}} \left(\frac{\partial}{\partial \zeta_y} - \mathcal{X}_y \frac{\zeta_x}{\mathcal{X}} \frac{\partial}{\partial \zeta_x} \right), \quad (\text{B.20b})$$

$$\frac{\partial}{\partial t} = \frac{\partial}{\partial \tilde{t}} - \left[\tilde{v}_x(1, \zeta_y, \tilde{t}) - \frac{\mathcal{X}_y}{\mathcal{Y}} \tilde{v}_y(1, \zeta_y, \tilde{t}) \right] \frac{\zeta_x}{\mathcal{X}} \frac{\partial}{\partial \zeta_x} - V \frac{\zeta_y}{\mathcal{Y}} \frac{\partial}{\partial \zeta_y}, \quad (\text{B.20c})$$

and

$$\begin{aligned} \frac{d}{dt} &= \frac{\partial}{\partial \tilde{t}} + \left\{ [\tilde{v}_x - \zeta_x \tilde{v}_x(1, \zeta_y, \tilde{t})] - \frac{\mathcal{X}_y}{\mathcal{Y}} \zeta_x [\tilde{v}_y - \tilde{v}_y(1, \zeta_y, \tilde{t})] \right\} \frac{1}{\mathcal{X}} \frac{\partial}{\partial \zeta_x} \\ &\quad + (\tilde{v}_y - \zeta_y V) \frac{1}{\mathcal{Y}} \frac{\partial}{\partial \zeta_y}. \end{aligned} \quad (\text{B.21})$$

For the boundary conditions, one needs the partial derivatives of X with respect to the new coordinate system. Since \mathcal{X} is only a function of ζ_y , the derivatives are

greatly simplified:

$$\frac{\partial X}{\partial x} = 0, \quad \frac{\partial X}{\partial y} = \frac{1}{\mathcal{Y}} \frac{\partial \mathcal{X}}{\partial \zeta_y} \quad (\text{B.22a})$$

$$\frac{\partial^2 X}{\partial x^2} = 0, \quad \frac{\partial^2 X}{\partial y^2} = \frac{1}{\mathcal{Y}^2} \frac{\partial^2 \mathcal{X}}{\partial \zeta_y^2}, \quad \frac{\partial^2 X}{\partial x \partial y} = 0. \quad (\text{B.22b})$$

B.3 Two Deforming Edges

The derivation below is similar to the previous section, except this time both the left and the right boundaries are allowed to deform. The mapping transforms the coordinates and all the relevant equations of a system confined within $x \in [X^0(y, t), X^1(y, t)]$ and $y \in [Y^0(t), Y^1(t)]$ to a square box $\zeta_x \in [0, 1]$ and $\zeta_y \in [0, 1]$.

The transform is defined as

$$\zeta_x \equiv \frac{x - X^0(y, t)}{\Delta X(y, t)}, \quad \zeta_y \equiv \frac{y - Y^0(t)}{\Delta Y(t)}, \quad \tilde{t} \equiv t, \quad (\text{B.23})$$

where

$$\Delta Z \equiv Z^1 - Z^0. \quad (\text{B.24})$$

Again, X needs to be a function of ζ_y , not y . Write the transform as

$$x = \zeta_x \mathcal{X}^1(\zeta_y, \tilde{t}) + (1 - \zeta_x) \mathcal{X}^0(\zeta_y, \tilde{t}), \quad (\text{B.25a})$$

$$y = \zeta_y \mathcal{Y}^1(\tilde{t}) + (1 - \zeta_y) \mathcal{Y}^0(\tilde{t}), \quad (\text{B.25b})$$

$$t = \tilde{t}. \quad (\text{B.25c})$$

Using the shorthand

$$W[\zeta, Z] \equiv \zeta Z^{(\zeta=1)} + (1 - \zeta) Z^{(\zeta=0)}, \quad (\text{B.26})$$

this can be written as

$$x = W[\zeta_x, \mathcal{X}(\zeta_y, \tilde{t})], \quad y = W[\zeta_y, \mathcal{Y}(\tilde{t})], \quad t = \tilde{t}. \quad (\text{B.27})$$

Notice that the only difference between the upright ΔX , X^0 , and X^1 , and the slanted $\Delta\mathcal{X}$, \mathcal{X}^0 , and \mathcal{X}^1 , is that the former are always functions of y and t , while the latter are functions of ζ_y and \tilde{t} . Similarly, ΔY , Y^0 , and Y^1 are functions of t , while $\Delta\mathcal{Y}$, \mathcal{Y}^0 , and \mathcal{Y}^1 are functions of \tilde{t} .

The following shorthand notations and definitions will be useful later:

$$X_y \equiv \frac{\partial X}{\partial y}, \quad X_t \equiv \frac{\partial X}{\partial t}, \quad Y_t \equiv \frac{\partial Y}{\partial t}, \quad (\text{B.28a})$$

$$\mathcal{X}_y \equiv \frac{\partial \mathcal{X}}{\partial \zeta_y}, \quad \mathcal{X}_t \equiv \frac{\partial \mathcal{X}}{\partial \tilde{t}}, \quad \mathcal{Y}_t \equiv \frac{\partial \mathcal{Y}}{\partial \tilde{t}}, \quad (\text{B.28b})$$

$$\omega_{xy} \equiv \frac{W[\zeta_x, \mathcal{X}_y]}{\Delta\mathcal{X}}, \quad \omega_{xt} \equiv \frac{W[\zeta_x, \mathcal{X}_t]}{\Delta\mathcal{X}}, \quad \omega_{yt} \equiv \frac{W[\zeta_y, \mathcal{Y}_t]}{\Delta\mathcal{Y}}. \quad (\text{B.29})$$

The differentials in the two different coordinate systems are connected by

$$\begin{pmatrix} dx \\ dy \\ dt \end{pmatrix} = A \begin{pmatrix} d\zeta_x \\ d\zeta_y \\ d\tilde{t} \end{pmatrix}, \quad (\text{B.30})$$

where

$$A = \begin{pmatrix} \Delta\mathcal{X} & \Delta\mathcal{X}\omega_{xy} & \Delta\mathcal{X}\omega_{xt} \\ 0 & \Delta\mathcal{Y} & \Delta\mathcal{Y}\omega_{yt} \\ 0 & 0 & 1 \end{pmatrix}. \quad (\text{B.31})$$

The inverse is

$$A^{-1} = \begin{pmatrix} \frac{1}{\Delta\mathcal{X}} & -\frac{\omega_{xy}}{\Delta\mathcal{Y}} & -\omega_{xt} + \omega_{xy}\omega_{yt} \\ 0 & \frac{1}{\Delta\mathcal{Y}} & -\omega_{yt} \\ 0 & 0 & 1 \end{pmatrix}. \quad (\text{B.32})$$

Further, the partial derivatives are linked by

$$\begin{pmatrix} \frac{\partial}{\partial x} \\ \frac{\partial}{\partial y} \\ \frac{\partial}{\partial t} \end{pmatrix} = (A^{-1})^T \begin{pmatrix} \frac{\partial}{\partial \zeta_x} \\ \frac{\partial}{\partial \zeta_y} \\ \frac{\partial}{\partial \tilde{t}} \end{pmatrix}. \quad (\text{B.33})$$

The total time derivative is given by

$$\begin{aligned}
\frac{d}{dt} &= \begin{pmatrix} v_x & v_y & 1 \end{pmatrix} \begin{pmatrix} \frac{\partial}{\partial x} \\ \frac{\partial}{\partial y} \\ \frac{\partial}{\partial t} \end{pmatrix} \\
&= \begin{pmatrix} v_x & v_y & 1 \end{pmatrix} (A^{-1})^T \begin{pmatrix} \frac{\partial}{\partial \zeta_x} \\ \frac{\partial}{\partial \zeta_y} \\ \frac{\partial}{\partial \tilde{t}} \end{pmatrix} \\
&= \left[A^{-1} \begin{pmatrix} v_x \\ v_y \\ 1 \end{pmatrix} \right]^T \begin{pmatrix} \frac{\partial}{\partial \zeta_x} \\ \frac{\partial}{\partial \zeta_y} \\ \frac{\partial}{\partial \tilde{t}} \end{pmatrix}. \tag{B.34}
\end{aligned}$$

Written out in full, these equations become

$$\frac{\partial}{\partial x} = \frac{1}{\Delta \mathcal{X}} \frac{\partial}{\partial \zeta_x}, \tag{B.35a}$$

$$\frac{\partial}{\partial y} = \frac{1}{\Delta \mathcal{Y}} \left(\frac{\partial}{\partial \zeta_y} - \omega_{xy} \frac{\partial}{\partial \zeta_x} \right), \tag{B.35b}$$

$$\frac{\partial}{\partial t} = \frac{\partial}{\partial \tilde{t}} - (\omega_{xt} - \omega_{xy}\omega_{yt}) \frac{\partial}{\partial \zeta_x} - \omega_{yt} \frac{\partial}{\partial \zeta_y}, \tag{B.35c}$$

and

$$\frac{d}{dt} = \frac{\partial}{\partial \tilde{t}} - (\Omega_x - \omega_{xy}\Omega_y) \frac{\partial}{\partial \zeta_x} - \Omega_y \frac{\partial}{\partial \zeta_y}, \tag{B.36}$$

where

$$\Omega_x = \omega_{xt} - \frac{v_x}{\Delta \mathcal{X}}, \quad \Omega_y = \omega_{yt} - \frac{v_y}{\Delta \mathcal{Y}}. \tag{B.37}$$

Having introduced \mathcal{X}^0 , \mathcal{X}^1 , \mathcal{Y}^0 , and \mathcal{Y}^1 means that four more equations of motion are needed. In the original coordinate system (x, y, t) , the total derivatives

of the boundaries are

$$\frac{dX^0}{dt} = v_x(x = X^0, y, t), \quad (\text{B.38a})$$

$$\frac{dX^1}{dt} = v_x(x = X^1, y, t), \quad (\text{B.38b})$$

$$\frac{dY^0}{dt} = v_y(x, y = Y^0, t) \equiv V^0(t), \quad (\text{B.38c})$$

$$\frac{dY^1}{dt} = v_y(x, y = Y^1, t) \equiv V^1(t). \quad (\text{B.38d})$$

It is worth noting that v_y is only a function of t when $y = Y^i$, since the boundaries there are straight. Eqs. (B.38) need to be written in the other coordinate system, $(\zeta_x, \zeta_y, \tilde{t})$. Using Eq. (B.36), (the tilde over the velocities just means that they are functions of ζ_x, ζ_y , and \tilde{t} , rather than x, y , and t)

$$\mathcal{Y}_t^0 = \frac{dY^0}{dt} = \tilde{v}_y(\zeta_x, 0, \tilde{t}) = \tilde{V}^0(\tilde{t}), \quad (\text{B.39a})$$

$$\mathcal{Y}_t^1 = \frac{dY^1}{dt} = \tilde{v}_y(\zeta_x, 1, \tilde{t}) = \tilde{V}^1(\tilde{t}), \quad (\text{B.39b})$$

$$\mathcal{X}_t^0 = \frac{dX^0}{dt} + \Omega_y(0, \zeta_y, \tilde{t})\mathcal{X}_y^0 = \tilde{v}_x(0, \zeta_y, \tilde{t}) + \left[\omega_{yt} - \frac{\tilde{v}_y(0, \zeta_y, \tilde{t})}{\Delta\mathcal{Y}} \right] \mathcal{X}_y^0, \quad (\text{B.39c})$$

$$\mathcal{X}_t^1 = \frac{dX^1}{dt} + \Omega_y(1, \zeta_y, \tilde{t})\mathcal{X}_y^1 = \tilde{v}_x(1, \zeta_y, \tilde{t}) + \left[\omega_{yt} - \frac{\tilde{v}_y(1, \zeta_y, \tilde{t})}{\Delta\mathcal{Y}} \right] \mathcal{X}_y^1. \quad (\text{B.39d})$$

This means that

$$\omega_{xt} = \frac{1}{\Delta\mathcal{X}} \left\{ W[\zeta_x, \tilde{v}_x] - \frac{W[\zeta_x, \tilde{v}_y\mathcal{X}_y]}{\Delta\mathcal{Y}} \right\} + \omega_{xy}\omega_{yt}, \quad (\text{B.40})$$

and Eqs. (B.35c) and (B.36) become

$$\frac{\partial}{\partial t} = \frac{\partial}{\partial \tilde{t}} - \frac{1}{\Delta\mathcal{X}} \left\{ W[\zeta_x, \tilde{v}_x] - \frac{W[\zeta_x, \tilde{v}_y\mathcal{X}_y]}{\Delta\mathcal{Y}} \right\} \frac{\partial}{\partial \zeta_x} - \frac{W[\zeta_y, \tilde{V}]}{\Delta\mathcal{Y}} \frac{\partial}{\partial \zeta_y} \quad (\text{B.41})$$

$$\begin{aligned} \frac{d}{dt} = & \frac{\partial}{\partial \tilde{t}} - \frac{1}{\Delta\mathcal{X}} \left\{ W[\zeta_x, \tilde{v}_x] - \tilde{v}_x - \frac{W[\zeta_x, \tilde{v}_y\mathcal{X}_y] - \tilde{v}_y W[\zeta_x, \mathcal{X}_y]}{\Delta\mathcal{Y}} \right\} \frac{\partial}{\partial \zeta_x} \\ & - \frac{1}{\Delta\mathcal{Y}} \left\{ W[\zeta_y, \tilde{V}] - \tilde{v}_y \right\} \frac{\partial}{\partial \zeta_y}, \end{aligned} \quad (\text{B.42})$$

respectively. As a final comment, note that by setting $X^0 \equiv 0$ to all the expressions in this section, one regains the results found in Section B.2.

BIBLIOGRAPHY

- [1] O. A. Hasan and M. C. Boyce, "A Constitutive Model for the Nonlinear Viscoelastic Viscoplastic Behavior of Glassy-Polymers," *Polym. Eng. Sci.*, vol. 35, p. 331, Feb 1995.
- [2] J. Rottler and M. O. Robbins, "Yield Conditions for Deformation of Amorphous Polymer Glasses," *Phys. Rev. E*, vol. 64, p. 051801, Nov 2001.
- [3] C. Marano and M. Rink, "Shear Yielding Threshold and Viscoelasticity in an Amorphous Glassy Polymer: A Study on a Styrene-Acrylonitrile Copolymer," *Polymer*, vol. 42, p. 2113, Mar 2001.
- [4] P. Chaudhari, B. C. Giessen, and D. Turnbull, "Metallic Glasses," *Sci. Am.*, vol. 242, no. 4, p. 98, 1980.
- [5] F. Spaepen and D. Turnbull, "Metallic Glasses," *Annu. Rev. Phys. Chem.*, vol. 35, p. 241, 1984.
- [6] A. Inoue, "Stabilization of Metallic Supercooled Liquid and Bulk Amorphous Alloys," *Acta Mater.*, vol. 48, p. 279, Jan 2000.
- [7] J. F. Loffler, "Bulk Metallic Glasses," *Intermetallics*, vol. 11, p. 529, Jun 2003.
- [8] A. S. Argon and H. Y. Kuo, "Plastic-Flow in a Disordered Bubble Raft (an Analog of a Metallic Glass)," *Mater Sci Eng*, vol. 39, no. 1, p. 101, 1979.
- [9] J. Lauridsen, M. Twardos, and M. Dennin, "Shear-Induced Stress Relaxation in a Two-Dimensional Wet Foam," *Phys. Rev. Lett.*, vol. 89, p. 098303, Aug 2002.
- [10] C. S. O'Hern, S. A. Langer, A. J. Liu, and S. R. Nagel, "Force Distributions Near Jamming and Glass Transitions," *Phys. Rev. Lett.*, vol. 86, p. 111, Jan 2001.
- [11] I. K. Ono, C. S. O'Hern, D. J. Durian, S. A. Langer, A. J. Liu, and S. R. Nagel, "Effective Temperatures of a Driven System Near Jamming," *Phys. Rev. Lett.*, vol. 89, p. 095703, Aug 2002.
- [12] R. P. Behringer, "Taking the Temperature," *Nature*, vol. 415, no. 6872, p. 594, 2002.
- [13] H. M. Jaeger, S. R. Nagel, and R. P. Behringer, "Granular Solids, Liquids, and Gases," *Rev. Mod. Phys.*, vol. 68, p. 1259, Oct 1996.
- [14] R. R. Hartley and R. P. Behringer, "Logarithmic Rate Dependence of Force Networks in Sheared Granular Materials," *Nature*, vol. 421, p. 928, Feb 2003.

- [15] A. Lemaitre, "Origin of a Repose Angle: Kinetics of Rearrangement for Granular Materials," *Phys. Rev. Lett.*, vol. 89, p. 064303, Aug 2002.
- [16] S. S. Hsiau and M. L. Hunt, "Shear-Induced Particle Diffusion and Longitudinal Velocity Fluctuations in a Granular-Flow Mixing Layer," *J. Fluid Mech.*, vol. 251, p. 299, Jun 1993.
- [17] W. Klement, R. H. Willens, and P. Duwez, "Non-Crystalline Structure in Solidified Gold-Silicon Alloys," *Nature*, vol. 187, no. 4740, p. 869, 1960.
- [18] W. L. Johnson, "Bulk Glass-Forming Metallic Alloys: Science and Technology," *MRS Bull.*, vol. 24, p. 42, Oct 1999.
- [19] A. Peker and W. L. Johnson, "A Highly Processable Metallic-Glass - Zr_{41.2}Ti_{13.8}Cu_{12.5}Ni_{10.0}Be_{22.5}," *Appl. Phys. Lett.*, vol. 63, p. 2342, Oct 1993.
- [20] F. Spaepen, "Microscopic Mechanism for Steady-State Inhomogeneous Flow in Metallic Glasses," *Acta Met*, vol. 25, no. 4, p. 407, 1977.
- [21] F. E. Luborsky, ed., *Amorphous Metallic Alloys*, ch. 13. London; Boston: Butterworths, 1983.
- [22] T. G. Nieh, C. Schuh, J. Wadsworth, and Y. Li, "Strain Rate-Dependent Deformation in Bulk Metallic Glasses," *Intermetallics*, vol. 10, p. 1177, Nov 2002.
- [23] C. A. Pampillo and A. C. Reimschuessel, "Fracture Topography of Metallic Glasses," *J. Mater. Sci.*, vol. 9, no. 5, p. 718, 1974.
- [24] C. A. Pampillo, "Flow and Fracture in Amorphous Alloys," *J. Mater. Sci.*, vol. 10, no. 7, p. 1194, 1975.
- [25] J. J. Lewandowski and P. Lowhaphandu, "Effects of Hydrostatic Pressure on the Flow and Fracture of a Bulk Amorphous Metal," *Philos. Mag. A-Phys. Condens. Matter Struct. Defect Mech. Prop.*, vol. 82, p. 3427, Nov 2002.
- [26] P. Lowhaphandu, S. L. Montgomery, and J. J. Lewandowski, "Effects of Superimposed Hydrostatic Pressure on Flow and Fracture of a Zr-Ti-Ni-Cu-Be Bulk Amorphous Alloy," *Scr. Mater.*, vol. 41, p. 19, Jun 1999.
- [27] C. P. Chou and F. Spaepen, "Some Mechanical-Properties of Phase Separated Pd_{0.74}Au_{0.08}Si_{0.38} Metallic Glasses," *Acta Met*, vol. 23, no. 5, p. 609, 1975.
- [28] A. S. Argon, "Mechanisms of Inelastic Deformation in Metallic Glasses," *J. Phys. Chem. Solids*, vol. 43, no. 10, p. 945, 1982.
- [29] M. Falk, *Deformation and Fracture in Amorphous Solids*. PhD thesis, UCSB, 1998.

- [30] M. L. Falk and J. S. Langer, "Dynamics of Viscoplastic Deformation in Amorphous Solids," *Phys. Rev. E*, vol. 57, p. 7192, Jun 1998.
- [31] L. D. Landau and E. M. Lifshitz, *Theory of Elasticity*, p. 2. Oxford: Pergamon, 1970. transl. J. B. Sykes and W. H. Reid.
- [32] W. S. Slaughter, *The Linearized Theory of Elasticity*. Boston: Birkhäuser, 2002.
- [33] L. D. Landau and E. M. Lifshitz, *Fluid Mechanics*, vol. 6. Oxford, England; New York: Pergamon Press, 2nd ed., 1987. transl. J. B. Sykes and W. H. Reid.
- [34] L. E. Malvern, *Introduction to the Mechanics of a Continuous Medium*. New Jersey: Prentice-Hall, Inc., 1969.
- [35] J. Lubliner, *Plasticity Theory*. New York: Macmillan Publishing Company, 1990.
- [36] V. Tvergaard and A. Needleman, "Shear-Band Development in Polycrystals," *Proc. R. Soc. London Ser. A-Math. Phys. Eng. Sci.*, vol. 443, p. 547, Dec 1993.
- [37] J. R. Rice and J. W. Rudnicki, "A Note on Some Features of the Theory of Localization of Deformation," *Int. J. Solids Struct.*, vol. 16, no. 7, p. 597, 1980.
- [38] E. W. Hart, "A Micromechanical Basis for Constitutive-Equations With Internal State Variables," *J. Eng. Mater. Technol.-Trans. ASME*, vol. 106, no. 4, p. 322, 1984.
- [39] J. C. Swearingen, T. C. Lowe, and J. Lipkin, "Constitutive-Equations for Rate-Dependent Plasticity," *Annu. Rev. Mater. Sci.*, vol. 15, p. 249, 1985.
- [40] K. S. Chan, S. R. Bodner, A. F. Fossum, and D. E. Munson, "A Constitutive Model for Inelastic Flow and Damage Evolution in Solids Under Triaxial Compression," *Mech. Mater.*, vol. 14, p. 1, Nov 1992.
- [41] G. A. Henshall and A. K. Miller, "Simplifications and Improvements in Unified Constitutive- Equations for Creep and Plasticity .1. Equations Development," *Acta Metall. Mater.*, vol. 38, p. 2101, Nov 1990.
- [42] E. Krempl, "Models of Viscoplasticity Some Comments on Equilibrium (Back) Stress and Drag Stress," *Acta Mech.*, vol. 69, p. 25, Dec 1987.
- [43] A. S. Krausz and K. Krausz, eds., *Unified Constitutive Laws of Plastic Deformation*, ch. 6, p. 281. San Diego: Academic Press, 1996.

- [44] I. Nishiguchi, T. L. Sham, and E. Krempl, "A Finite Deformation-Theory of Viscoplasticity Based on Overstress .1. Constitutive-Equations," *J. Appl. Mech.-Trans. ASME*, vol. 57, p. 548, Sep 1990.
- [45] A. Lemaitre, "Rearrangements and Dilatancy for Sheared Dense Materials," *Phys. Rev. Lett.*, vol. 89, p. 195503, Nov 2002.
- [46] R. Huang, Z. Suo, J. H. Prevost, and W. D. Nix, "Inhomogeneous Deformation in Metallic Glasses," *J. Mech. Phys. Solids*, vol. 50, no. 5, p. 1011, 2002.
- [47] M. L. Falk, "Molecular-Dynamics Study of Ductile and Brittle Fracture in Model Noncrystalline Solids," *Phys. Rev. B*, vol. 60, p. 7062, Sep 1999.
- [48] M. L. Falk and J. S. Langer, "From Simulation to Theory in the Physics of Deformation and Fracture," *MRS Bull.*, vol. 25, no. 5, p. 40, 2000.
- [49] J. S. Langer and A. E. Lobkovsky, "Rate-and-State Theory of Plastic Deformation Near a Circular Hole," *Phys. Rev. E*, vol. 60, p. 6978, Dec 1999.
- [50] J. S. Langer, "Viscoplasticity and the Dynamics of Brittle Fracture," *Phys. Rev. E*, vol. 62, p. 1351, Jul 2000.
- [51] A. E. Lobkovsky and J. S. Langer, "Dynamic Ductile to Brittle Transition in a One-Dimensional Model of Viscoplasticity," *Phys. Rev. E*, vol. 58, p. 1568, Aug 1998.
- [52] J. S. Langer, "Microstructural Shear Localization in Plastic Deformation of Amorphous Solids," *Phys. Rev. E*, vol. 6401, p. 011504, Jul 2001.
- [53] R. Balian, M. Kléman, and J.-P. Poirier, eds., *Les Houches Lectures, session XXXV: Physics of Defects*, p. 133. Amsterdam: North Holland, 1981.
- [54] A. S. Argon, "Plastic-Deformation in Metallic Glasses," *Acta Met*, vol. 27, no. 1, p. 47, 1979.
- [55] A. S. Argon and L. T. Shi, "Development of Visco-Plastic Deformation in Metallic Glasses," *Acta Met*, vol. 31, no. 4, p. 499, 1983.
- [56] V. A. Khonik and A. T. Kosilov, "Kinetics of Strain Relaxation in Metallic Glasses," *J. Non-Cryst. Solids*, vol. 170, p. 270, Jul 1994.
- [57] M. H. Cohen and D. Turnbull, "Molecular Transport in Liquids and Glasses," *J. Chem. Phys.*, vol. 31, no. 5, p. 1164, 1959.
- [58] D. Turnbull and M. H. Cohen, "Free-Volume Model of Amorphous Phase - Glass Transition," *J. Chem. Phys.*, vol. 34, no. 1, p. 120, 1961.
- [59] D. Turnbull and M. H. Cohen, "On Free-Volume Model of Liquid-Glass Transition," *J. Chem. Phys.*, vol. 52, no. 6, p. 3038, 1970.

- [60] D. Suh and R. H. Dauskardt, "Effects of Open-Volume Regions on Relaxation Time-Scales and Fracture Behavior of a Zr-Ti-Ni-Cu-Be Bulk Metallic Glass," *J. Non-Cryst. Solids*, vol. 317, p. 181, Mar 2003.
- [61] U. Harms, O. Jin, and R. B. Schwarz, "Effects of Plastic Deformation on the Elastic Modulus and Density of Bulk Amorphous Pd₄₀Ni₁₀Cu₃₀P₂₀," *J. Non-Cryst. Solids*, vol. 317, p. 200, Mar 2003.
- [62] V. A. Fedorov and I. V. Ushakov, "Effect of Annealing on the Deformation and Fracture of Metallic Glass Under Local Loading," *Tech. Phys.*, vol. 46, p. 673, Jun 2001.
- [63] P. de Hey, J. Sietsma, and A. van Den Beukel, "Structural Disordering in Amorphous Pd₄₀Ni₄₀P₂₀ Induced By High Temperature Deformation," *Acta Mater.*, vol. 46, p. 5873, Oct 1998.
- [64] A. Inoue, T. Zhang, and T. Masumoto, "Reductilization of Embrittled La-Al-Ni Amorphous-Alloys By Viscous-Flow Deformation in a Supercooled Liquid Region," *J. Non-Cryst. Solids*, vol. 156, p. 598, 1993.
- [65] C. A. Pampillo and D. E. Polk, "Annealing Embrittlement in an Iron-Nickel-Based Metallic Glass," *Mater Sci Eng*, vol. 33, no. 2, p. 275, 1978.
- [66] J. S. Langer, L. Pechenik, and M. L. Falk, "Thermal effects in the shear-transformation-zone theory of amorphous plasticity: Comparisons to metallic glass data." <http://www.arXiv.org/abs/cond-mat/0311057>, Nov 2003.
- [67] D. Kivelson, G. Tarjus, X.-L. Xiao, and S. A. Kivelson, "Reply to 'Comment on 'Fitting of viscosity: Distinguishing the temperature dependences predicted by various models of supercooled liquids''," *Phys. Rev. E*, vol. 54, p. 5873, Nov 1996.
- [68] M. Doi and S. F. Edwards, *The Theory of Polymer Dynamics*, vol. 73 of *Int. Ser. Monogr. Phys.*, p. 350. New York: Oxford University Press Inc., 1988.
- [69] J. S. Langer and L. Pechenik, "Dynamics of shear-transformation zones in amorphous plasticity: Energetic constraints in a minimal theory." <http://www.arXiv.org/abs/cond-mat/0301009>, Jul 2003.
- [70] L. Pechenik, "Energetic processes in the shear-transformation-zone theory of plastic deformation." <http://www.arXiv.org/abs/cond-mat/0305516>, May 2003.
- [71] L. O. Eastgate, J. S. Langer, and L. Pechenik, "Dynamics of Large-Scale Plastic Deformation and the Necking Instability in Amorphous Solids," *Phys. Rev. Lett.*, vol. 90, p. 045506, Jan 2003.

- [72] A. I. Taub and F. Spaepen, "Ideal Elastic, Anelastic and Viscoelastic Deformation of a Metallic-Glass," *J. Mater. Sci.*, vol. 16, no. 11, p. 3087, 1981.
- [73] L. O. Eastgate, J. P. Sethna, M. Rauscher, T. Cretegnny, C. S. Chen, and C. R. Myers, "Fracture in Mode I using a Conserved Phase-Field Model," *Phys. Rev. E*, vol. 65, p. 036117, Mar 2002.
- [74] J. A. Sethian, *Level Set Methods and Fast Marching Methods: Evolving Interfaces in Computational Geometry, Fluid Mechanics, Computer Vision, and Materials Science*. Cambridge, U.K.; New York: Cambridge University Press, 2nd ed., 1999.
- [75] S. J. Osher and R. P. Fedkiw, *Level Set Methods and Dynamic Implicit Surfaces*. New York: Springer Verlag, 2003.
- [76] W. H. Press, S. A. Teukolsky, W. T. Vetterling, and B. P. Flannery, *Numerical Recipes in C++*. Cambridge University Press, 2002.
- [77] J. Lu, G. Ravichandran, and W. L. Johnson, "Deformation Behavior of the Zr_{41.2}Ti_{13.8}Cu_{12.5}Ni₁₀Be_{22.5} Bulk Metallic Glass over a Wide Range of Strain-Rates and Temperatures," *Acta Mater.*, vol. 51, p. 3429, Jul 2003.
- [78] A. C. Lund and C. A. Schuh, "Yield Surface of a Simulated Metallic Glass," *Acta Mater.*, vol. 51, p. 5399, Oct 2003.
- [79] C. A. Schuh, A. S. Argon, T. G. Nieh, and J. Wadsworth, "The Transition from Localized to Homogeneous Plasticity During Nanoindentation of an Amorphous Metal," *Philos. Mag.*, vol. 83, p. 2585, Aug 2003.
- [80] W. J. Wright, T. C. Hufnagel, and W. D. Nix, "Free Volume Coalescence and Void Formation in Shear Bands in Metallic Glass," *J. Appl. Phys.*, vol. 93, p. 1432, Feb 2003.
- [81] C. A. Schuh, T. G. Nieh, and Y. Kawamura, "Rate Dependence of Serrated Flow During Nanoindentation of a Bulk Metallic Glass," *J. Mater. Res.*, vol. 17, p. 1651, Jul 2002.
- [82] P. E. Donovan, "A Yield Criterion for Pd₄₀Ni₄₀P₂₀ Metallic-Glass," *Acta Met*, vol. 37, p. 445, Feb 1989.
- [83] C. A. Pampillo and H. S. Chen, "Comprehensive Plastic-Deformation of a Bulk Metallic Glass," *Mater Sci Eng*, vol. 13, no. 2, p. 181, 1974.
- [84] S. Takayama, "Serrated Plastic-Flow in Metallic Glasses," *Scr Metall*, vol. 13, no. 6, p. 463, 1979.
- [85] J. Fineberg and M. Marder, "Instability in Dynamic Fracture," *Phys. Rep.-Rev. Sec. Phys. Lett.*, vol. 313, no. 1-2, p. 2, 1999.